Title
Mechanical Properties and Failure Mechanisms of Advanced Structural Materials

Author
Ell, Jon Floyd

Publication Date
2022

Peer reviewed|Thesis/dissertation

Mechanical Properties and Failure Mechanisms of Advanced Structural Materials

by

Jon Floyd Ell

A dissertation submitted in partial satisfaction

of the requirements for the degree of

Doctor of Philosophy

in

Engineering – Materials Science and Engineering

in the

Graduate Divisions

of the

University of California, Berkeley

Committee in charge:

Professor Robert O. Ritchie, Chair
Professor Andrew M. Minor
Professor Peter Hosemann

Spring 2022

Abstract

Mechanical Properties and Failure Mechanisms of Advanced Structural Materials

by

Jon Floyd Ell

Doctor of Philosophy in Engineering – Materials Science and Engineering

University of California, Berkeley

Professor Robert O. Ritchie, Chair

The advancement of structural materials with different engineering applications is dependent on understanding their mechanics and mechanisms of deformation and fracture. The performance of materials under extreme environmental conditions is the limiting factor in many engineering systems: from the jet engine, to nuclear power plants, to something as mundane as a bridge or building. In this study, three structural materials are examined from the perspective of understanding how their unique microstructures lend them their ability to mechanically withstand the extreme environments they are designed for. First, Deformed and Partitioned (D&P) steel is discussed. D&P steel possesses good mechanical properties: a yield strength around 2GPa and a fracture toughness as high as 100 MPa$\sqrt{m}$. The way D&P steel is processed produces a highly tailored martensite/austenite duplex microstructure. This microstructure allows for both transformation induced plasticity (TRIP) and delamination toughening to forego the strength-toughness trade-off, without the addition of expensive alloying elements. Next, Tristructural isotropic (TRISO) nuclear fuel particles tested with the ALS tomography beamline are described. Due to the complex layered microstructures, *in situ* tomography is required to examine the internal features and failure mechanisms of the particles while being deformed at room temperature and 1000 ℃. This technique is used to examine the change in failure loads and fracture mechanisms due to the presence or absence of a SiC layer within the particles. For the TRISO particles, the results show that the SiC layer is responsible for a decrease in strength at higher temperatures due to the relaxation and redistribution of residual stresses. Finally, the mechanical properties, microstructural characterization, and failure mechanisms of body-centered cubic refractory high entropy superalloys ($Ti_{20}Zr_{20}Nb_{25}Ta_{25}Al_{10}$) are provided for two differing heat treatments. The first heat treatment has a microstructure with a brittle matrix and a ductile precipitate, whereas the second is inverted, having a ductile matrix and brittle precipitate. These two heat treatments were then examined in compression, tension, and fracture toughness at room and elevated temperatures. These materials have high yield strengths and ductility in compression, yet they are brittle in tension and have low fracture toughness values at all temperatures. Both heat treatments were brittle in tension and failed intergranularly because a ductile phase with a smaller fraction of the secondary strengthening precipitate phase formed at the grain boundaries which weakened the material.

To those who strive to advance mankind

Table of Contents

List of Figures

List of Tables

Acknowledgements

First and foremost, I would like to thank my advisor, Professor Robert O. Ritchie. Professor Ritchie has been an incredible role model and advisor. He has encouraged me to pursue my interests and supported my projects. It has been an honor to have Professor Ritchie as a mentor for my time at UC Berkeley.

Thank you to Dr. Qin Yu, who is the hardest working, most kind, and humble person I know. We have worked very closely through the years and have become an inseparable team. I have no doubt that we have forged a lifelong friendship.

To the undergraduate and graduate students who have worked with me, thank you. David and Andrew: thank you for your hard work, your support, and for making even the monotonous tasks enjoyable. To my fellow graduate students that departed before me, thank you for inspiring me to do my best work.

Thank you to my co-authors, who along with being some of the finest minds I have worked with, have permitted me to leverage their work in this dissertation.

This work was supported by the National Science Foundation Graduate Research Fellowship Program, the Mechanical Behavior of Materials Program (KC13), and The Citrine Informatics project. The support from these programs enabled me to attend Berkeley, work for Professor Ritchie, and be a part of incredible research.

Chapter 1
Introduction

The role of structural materials has and continues to provide the infrastructural framework of our society. These materials ensure our buildings continue to stand, our cars, trains, and airplanes continue to transport people around the world, and most importantly: to allow us to produce the energy that makes all of it possible in the first place. Without steel, we could not make skyscrapers, bridges or roads. Without nuclear materials, we could not ensure the safe and efficient operation of nuclear power plants. And last but not least, without nickel superalloys, we could not fly our airplanes, run our land-based generators, or even build oil and gas refineries. For this reason, researchers and engineers are on a constant search to discover new, higher-performing structural materials since their discovery could not only reduce our society's material usage, but also increase our energy efficiency by allowing for increased operating temperatures in jet engines and land-based turbines. This search is challenging: the strength-toughness trade off makes it difficult to make materials stronger without decreasing their toughness and preventing catastrophic failure [1], [2], and higher temperature, extremely corrosive conditions for which many of our existing materials have been made for, add a multitude of variables in materials design [3]. Because of this, the search for higher performing materials often involves finding new combinations of elements, tailoring microstructures, and combining materials to form composites. As these materials become more complex, so too do the materials' mechanisms of fracture and failure. Understanding these mechanisms on the microstructural level and how they impact the materials mechanical properties (be it negatively or positively), allows for this knowledge to be translated to multiple materials systems. For instance, understanding the mechanism of creep has led to increased high temperature performance by using single crystal parts. This study will focus on the mechanical testing and analysis of the failure mechanisms of several types of materials, such as D&P steel, complex composite nuclear fuel particles, and high entropy superalloys. These materials have complex microstructures and fracture mechanisms that can help or hinder their desired performance. Chapter 2 covers work on D&P steel that was recently published in *Science* [4], Chapter 3 covers work on Nuclear fuel particles that was published in *Materials and Design* [5], and Chapter 4 covers work on high entropy superalloys that is being prepared for publication.

First, deformed and partitioned (D&P) steels will be discussed. D&P steel has been shown to be very strong and ductile when compared to other high-strength steels. Most high-strength steels achieve their strength by alloying with more expensive elements; however, D&P steel achieves its strength without alloying elements, which makes it comparably inexpensive [4], [6]. In addition to having excellent mechanical properties and being low-cost, D&P steel is processed through conventional processing techniques, making it possible to be widely adopted into industrial manufacturing. D&P steel's excellent mechanical properties are due to its complex martensite/austenite duplex microstructure that allows for multiple added toughening and strengthening mechanisms. In this study, D&P steel's mechanical properties, microstructure, and failure mechanisms are thoroughly examined to understand the mechanisms at play.

Next, composite tristructural isotropic (TRISO) nuclear fuel particles, and *in situ* tomography testing will be discussed. TRISO particles are widely used in nuclear reactors and are being considered for next generation high-temperature gas cooled reactors [7] and very high temperature reactors [8]. They are composed of multiple layers of different materials coming together to form a complex inner structure that makes their fracture properties difficult to predict. By utilizing the x-ray tomography beamline, the internal structure and fracture mechanism are examined with and without the presence of an SiC layer at room temperature and at 1000 ℃. This allows for the effect of the SiC layer to be determined in terms of failure load and failure mechanisms.

Another class of materials that will be discussed are refractory high entropy superalloys (RHSAs). These materials have emerged as a promising replacement for Ni-based superalloys because of their ability to retain high strength at high temperatures. High entropy alloys (HEAs) are a new class of materials that were first developed by Cantor *et al.* [9] and theorized by Yeh *et al.* [10] in the early 2000's. The discovery of HEAs has both opened up a new field in metallurgy and propelled the search for new HEAs with particular properties. Since there are approximately 60 usable metals, when quinary combinations are considered there are millions of possible alloys, and when any number of constituents are considered there are effectively infinite combinations. Therefore, finding a good alloy can best be described as looking for a needle in a haystack. Certain combinations of refractory metals subjected to specific heat treatments can form complex dual phase microstructures, classified as RHSAs, of which many have been developed and tested. However, the majority of these alloys have been tested in compression, resulting in literature that shows reasonable ductility at high temperatures, even in the range of ~20%. That said, these published properties do not accurately represent these materials' useful tensile properties. In this study, $Ti_{20}Zr_{20}Nb_{25}Ta_{25}Al_{10}$ is examined with two different heat treatments giving two different superalloy microstructures. The first, a likely more brittle material, consists of a hard brittle matrix material and a ductile precipitate referred to as the 600HT condition. The second is a ductile matrix with a hard brittle precipitate referred to at the 800HT condition. These materials' mechanical properties and failure mechanisms were analyzed for compression, tensile, and fracture toughness tests at room temperature, 800 ℃, 1000 ℃, and 1200 ℃.

Chapter 2
Deformed and Partitioned Steel

2.1 INTRODUCTION

The *holy grail* of structural materials is one with superior mechanical properties that is also lightweight and inexpensive. Since steel is the most widely used alloy in our modern society, the ability to increase both its strength and toughness would have a very large impact on infrastructure design, material consumption, and would thus expand its use. Both strength and toughness are invariably required properties for structural materials. However, in metallic materials these properties are typically mutually exclusive: as the strength of a metallic material increases, fracture toughness tends to decrease. This decrease in toughness creates a major concern in safety critical applications, and limits the use of a material [1], [11].

The microstructural principle behind strengthening a metal is by inhibiting dislocation motion [12], [13]. To inhibit dislocation motion, obstacles to dislocations are added at variable length scales. While these obstacles prevent dislocation motion, and thus plasticity, they invariably cause dislocations to become entangled at lower strains, causing localized stress concentrations which can lead to crack initiation and catastrophic failure [1], [14]. Most efforts to overcome this strength-toughness trade-off are focused on (1) solid solution alloying or (2) tailoring a materials microstructure. The first method is currently being employed to create deformation-induced nano-twinning mechanisms in high and medium-entropy alloys that give them excellent fracture toughness at cryogenic temperatures [15], [16]. It is also used in maraging steels, endowing them with both strength and toughness, allowing them to be used in aerospace applications. However, solid solution strengthening requires the inclusion of usually several expensive alloying elements. For maraging steel, the alloying elements include nickel (17-19 wt.%), cobalt (8-12 wt.%) and molybdenum (3-5 wt.%) [17]. While this strategy does make maraging steel an excellent and useful material with high strength and toughness, the costs and environmental concerns make its mass production and recycling not economical [12], [18]. The alternative method, tailoring a material's microstructure, is also being explored to increase both strength and toughness. However, this method is limited by the complex, expensive, and time consuming processing techniques that can generally only produce small samples [19]–[22]. Another way to increase both strength and toughness is to decrease the average grain size, however this usually decreases ductility [23]–[25]. Here it is shown that high toughness and strength can both be achieved in steel with an inexpensive composition and processing methods. It is demonstrated that increasing the yield strength allows for the delamination toughening mechanism to be activated which significantly increases the toughness [26], [27]. Delamination toughening is activated at ultrahigh yield strengths at which a secondary fracture mode can occur causing delamination cracking. Multiples of these delaminating cracks form normal to the primary fracture surface which provide an increased energy release rate for the fracture, and improve crack tip blunting increasing the fracture toughness. This delamination toughening with the addition transformation induced plasticity (TRIP) toughening allows for the incredible strength, ductility, and toughness of D&P steel. In this chapter, I will evaluate the tensile strength, fracture toughness, and the toughening mechanisms of D&P steel. I performed all of the sample preparation for these materials including the surface polishing and precracking of the

compact tension specimens. I set up the optical long distance microscope to track the crack propagation length that was used alongside the crack tip opening displacement gauge. I performed all the tensile and fracture toughness tests. I examined the fracture surfaces of the tensile and fracture toughness specimens, and helped theorize the failure mechanisms.

2.2 PROCESSING AND MICROSTRUCTURE

D&P steel, a medium manganese steel, consists of relatively low amounts of alloying materials as shown in **Table 2.1**. The manganese and carbon act as austenite stabilizers, the aluminum prevents cementite precipitation, and the vanadium forms nanometer-sized carbides.

Table 2.1 The weight percent composition of D&P Steel

Fe	Mn	C	Al	V
Balance	9.95 wt.%	0.44 wt.%	1.87 wt.%	0.67 wt.%

2.2.1 Processing

D&P steel was fabricated by a complex deforming and partitioning treatment, as shown in **Figure 2.1** [6]. The components of the steel were cast by induction melting and then forged into a rectangular ingot with a thickness of 60 mm and a width of 80 mm. The ingot was then homogenized at 1150 °C for 2.5 hours. At this point the steel is almost fully austenitic. After homogenization, it was hot rolled to a thickness of 3.8 mm. This hot rolling allowed for some manganese to diffuse to the grain boundaries, elongate the austenite grains in the rolling direction (RD) and reduce the sample to a more manageable thickness. Following hot rolling, the sample was reheated to 750 °C for 10 min, followed by warm rolling to a thickness of 1.9 mm, which introduced dislocations, further elongation in the microstructure in the RD, and allowed for more manganese segregation. Intercritical annealing was performed at 620 °C for 5 hours to promote dislocation recovery and manganese segregation. Cold rolling reduced the sample to the final thickness of 1.4 mm and severely increased the number of dislocations. The process of cold rolling also transformed the mostly austenitic material into a lamellar martensite/austenite duplex microstructure [6], [28]. In the duplex microstructure austenite makes up 47.5% of the volume measured by neutron diffraction. Finally, the cold rolled strip was partitioned at 300 °C for 6 minutes followed by water quenching to room temperature. Partitioning allows for carbon to diffuse out of the martensite into the austenite to stabilize both phases and allow for more ductility even in the presence of a high dislocation density [6]. The prior austenite grain boundaries (PAGB's) were retained during cold rolling when about half of the austenite grains transform to martensite.

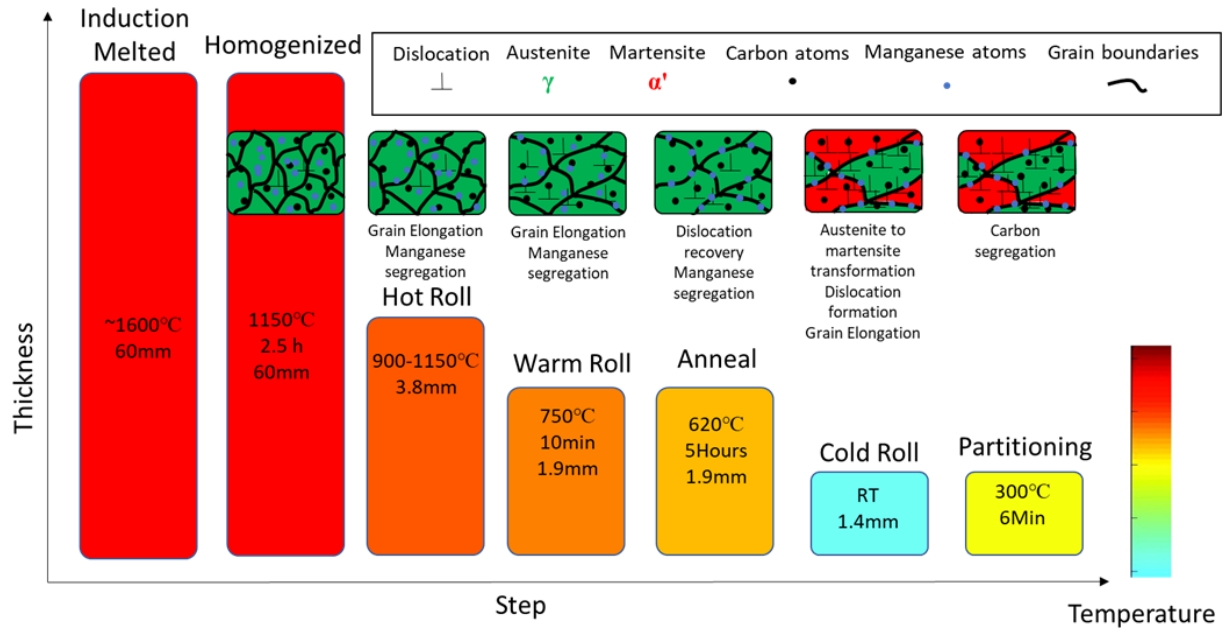

Figure 2.1: A schematic of the processing steps to form D&P steel and the microstructural changes that occur at each step. The components of the steel were cast by induction melting. The ingot was then homogenized and hot rolled. The hot rolling allowed for some manganese to diffuse to the grain boundaries, and elongated the grains. Warm rolling introduced dislocations, further elongation in the microstructure, and allowed for more manganese segregation. Intercritical annealing was performed to promote dislocation recovery and manganese segregation. Cold rolling reduced the sample to the final thickness and severely increased the number of dislocations. The process of cold rolling also transformed the mostly austenitic material into a lamellar martensite/austenite duplex microstructure. Finally, the cold rolled strip was partitioned allowing for carbon to diffuse out of the martensite into the austenite The PAGB's were retained during cold rolling.

This processing creates a complex martensite/austenite duplex microstructure shown in **Figure 2.2A**. The martensite newly formed during cold working is composed of nanosized grains with an extremely high dislocation density **Figure 2.2C**. The dislocation density of the martensite was 2.43×10^{16} m^2 measured by neutron diffraction and is at least an order of magnitude higher than other martensitic steels(citation or figure needed). The austenite phase remains formed into long flat grains elongated in the RD and flattened in the normal direction (ND) **Figure 2.2A**. The grain boundaries that were present before cold working when the sample was single phase austenite the PAGB's are retained after cold working and partitioning highlighted in **Figure 2.2B**. Atom probe tomography showed segregation of Mn and C to these PAGBs **Figure 2.2D**. **Figure 2.2D** is an illustration of the important features seen in D&P steel.

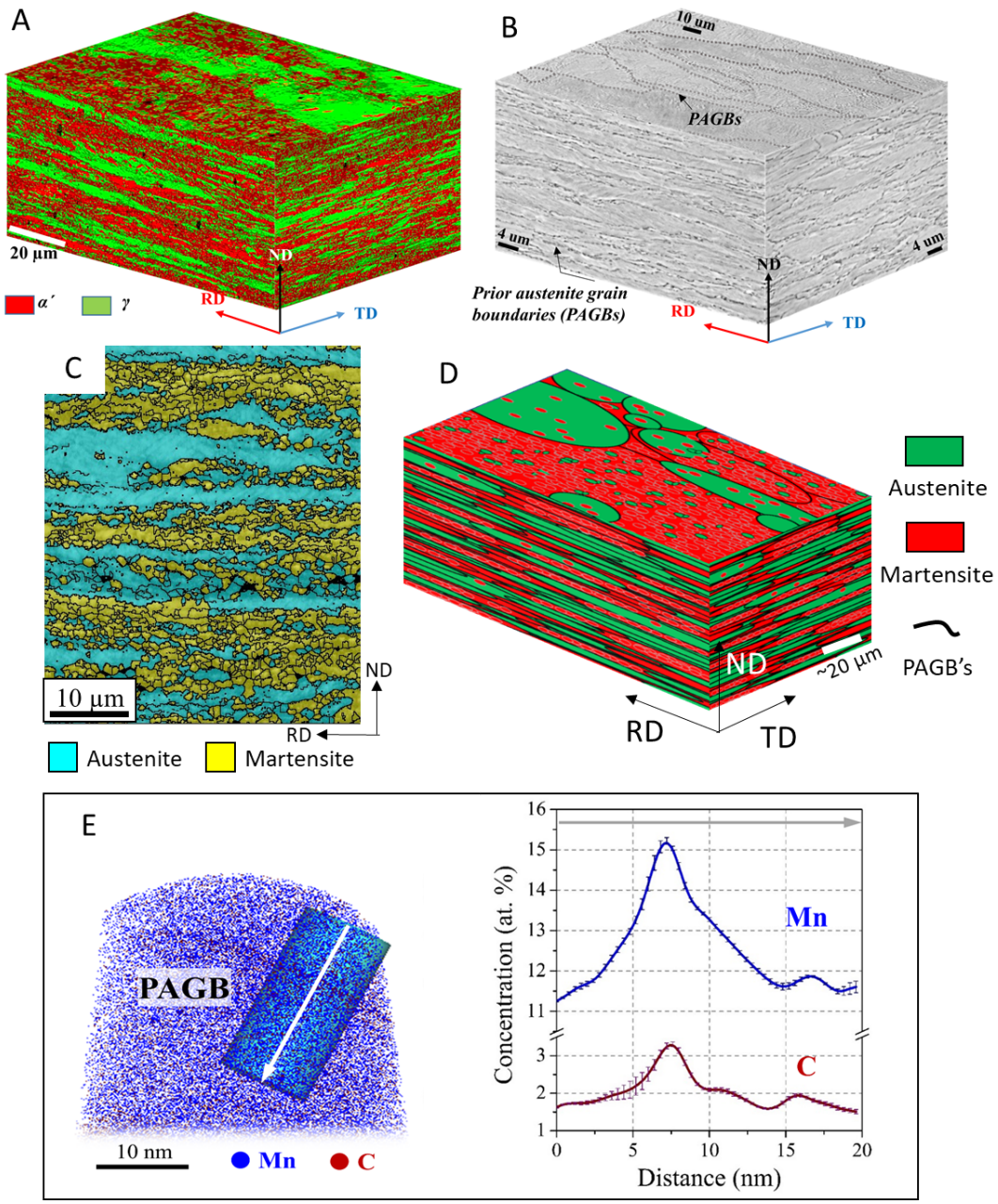

Figure 2.2: (**A**) is a 3D A schematic stereographic microstructure reconstructed by electron back-scatter diffraction (EBSD) phase maps. They were scanned on the rolling direction (RD), transverse direction (TD), and normal direction (ND). This EBSD scan shows the D&P steel's heterogeneous laminated duplex microstructure composed of a martensitic matrix (α') (red) and elongated austenite (γ) (green) lamellae. (**B**) 3-D stereographic microstructure imaged by SEM of the prior-austenite grain boundaries indicated by the dotted lines. (**C**) EBSD phase map of the microstructure showing the nanometer sized martensite grains (yellow) and the elongated austenite (blue). (**D**) Illustration of the important aspects D&P steel, showing its microstructure, with two phases - austenite in green and martensite in red - and the PAGB represented by thick black lines. These austenite and prior austenite grains are elongated along the rolling direction (RD), and flattened in the normal direction (ND). (**E**) 3-D ion concentration map of a PAGB and on the right a 1-D concentration profile that shows the segregation of Mn and C to these boundaries.

2.3 MECHANICAL PROPERTIES

The tensile properties and fracture toughness properties of D&P steel were examined via dog-bone tensile tests and *J*-integral based crack-resistance (*J*-Δ*a*) R-curves respectively. The tensile and fracture toughness tests were performed in both the RD and TD orientations. **Figure 2.3** shows the tensile (dog-bone) and fracture toughness (compact-tension (C(T))) specimens RD (orange) and the TD (blue) orientations. The RD tensile specimens are strained along the elongated austenite grains, and for the RD fracture toughness specimens the crack has to travel perpendicularly through the elongated grains.

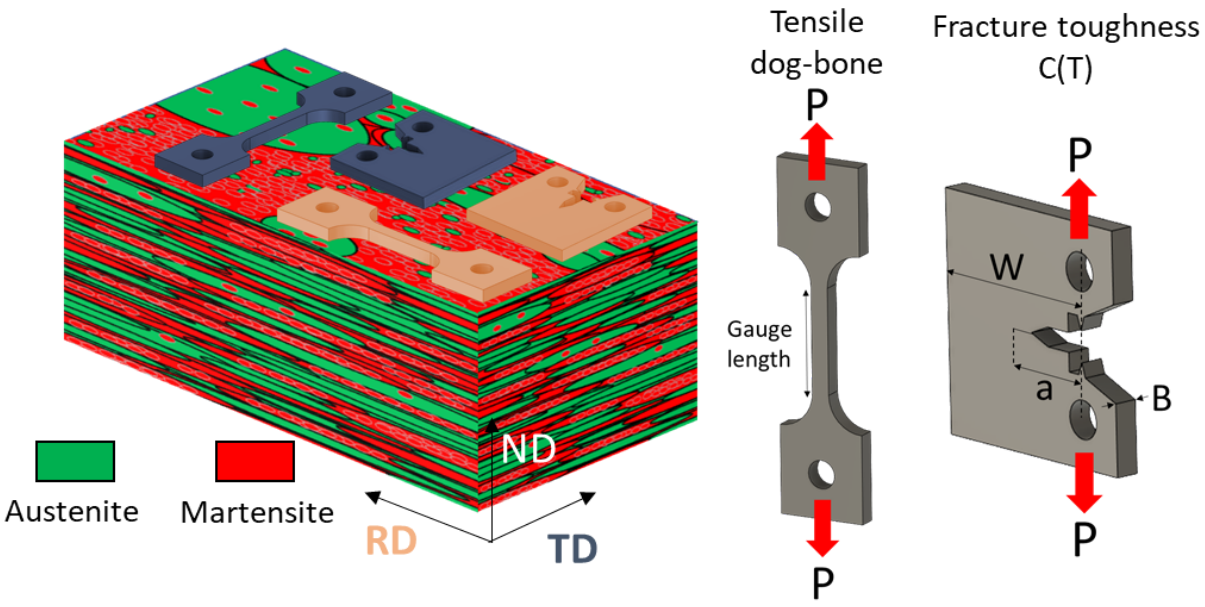

Figure 2.3: A schematic demonstrating the orientations of the tensile and fracture toughness samples for RD and TD.

2.3.1 Tensile Properties

When loading in the RD, tensile properties are enhanced by the extremely high dislocation density creating an extremely high strength and ductility **(Figure 2.4, Table 2.2)** [6]. The upper yield strength (σ_{yu}), the ultimate tensile strength (σ_{uts}) and the uniform elongation (ε_u) are 1,978 MPa, 2,144 MPa and 19.0%, respectively in RD. The RD specimen's initial plastic deformation was dominated by Lüders band propagation; the lower yield point is seen in **Table 2.2**. The TD aligned tensile properties also have a high ultimate strength of 2,048 MPa, but it has a lower yield strength of 1,714 MPa at the 0.2% offset and a lower strain at failure as seen in **Figure 2.4**.

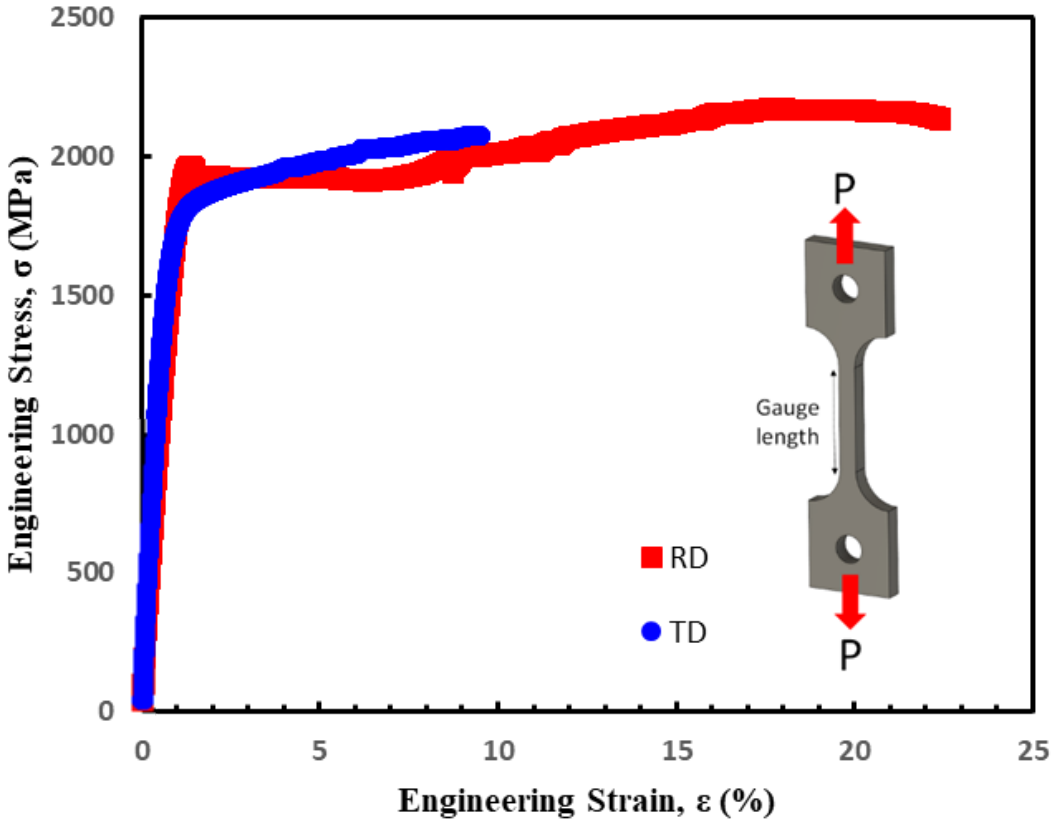

Figure 2.4: Engineering stress-strain curve of D&P steel deformed in tension in RD and TD orientations.

D&P steel gets its high strength from the high dislocation density in the martensitic phase which makes up 52.5% of the material. This high strength phase should also cause the material to become very brittle, but the partitioning allows carbon to diffuse out of the martensite into the austenite, thus stabilizing both phases. This stabilization allows the martensite to be far more ductile than conventional martensite [29]. In addition, the more ductile martensite is sandwiched between layers of ductile austenite, which further contributes to the ductility [30]. The austenite can also undergo transformation-induced plasticity (TRIP), which continually strain hardens the material, increasing the elongation at failure [31].

2.3.2 Fracture Toughness

Due to D&P steel's ultrahigh strength and ductility, the fracture toughness was measured by *J*-integral based R-curves in terms of *J* as a function of stable crack extension Δa. This is done in accordance with ASTM Standard E1820 [32]. **Figure 2.5** shows the R-curves constructed from the testing procedure and **Table 2.2** shows important values taken from the R-curve and stress-strain curve. The fracture toughness along the TD is measured at an average J_{Ic} of 19.6 kJ·m^{-2} at crack initiation. As can be seen from **Figure 2.5** the R-curve rises as the crack extends at 1 mm the crack growth toughness (J_{ss}) is 28.7 kJ·m^{-2}. These properties are comparable to 18Ni 300-grade maraging steels, 300M, and 4340 steels, some of the best strong and tough materials there are [33]–[36]. With a strength-toughness trade off it is unexpected that while the RD has a higher yield strength than TD it also has a better fracture toughness. The R-curve shows that RD

has a crack initiation toughness of J_{Ic} of 46.9 kJ·m^{-2} and a crack growth resistance J_{ss} of 84.6 kJ·m^{-2} at 1 mm. This is significantly higher than TD fracture toughness values. Utilizing the mode-I *J-K* equivalence ($K_{JIc} = (E'J_{Ic})^{½}$ where E' = elastic modulus (E) in plane stress, and = E/(1-ν^2) in plane strain where ν is Poisson's ratio), crack-initiation toughness in the RD and TD orientations are K_{JIc} is 101.5 and 65.4 MPa·m^{½}, respectively, with crack growth toughness of K_{ss}, = 136.4 (RD) and 79.4 MPa·m^{½} (TD) at Δa 1 mm. These extremely high toughness values seen in the D&P steel are exceptional for materials with a yield strength of ~2 GPa.

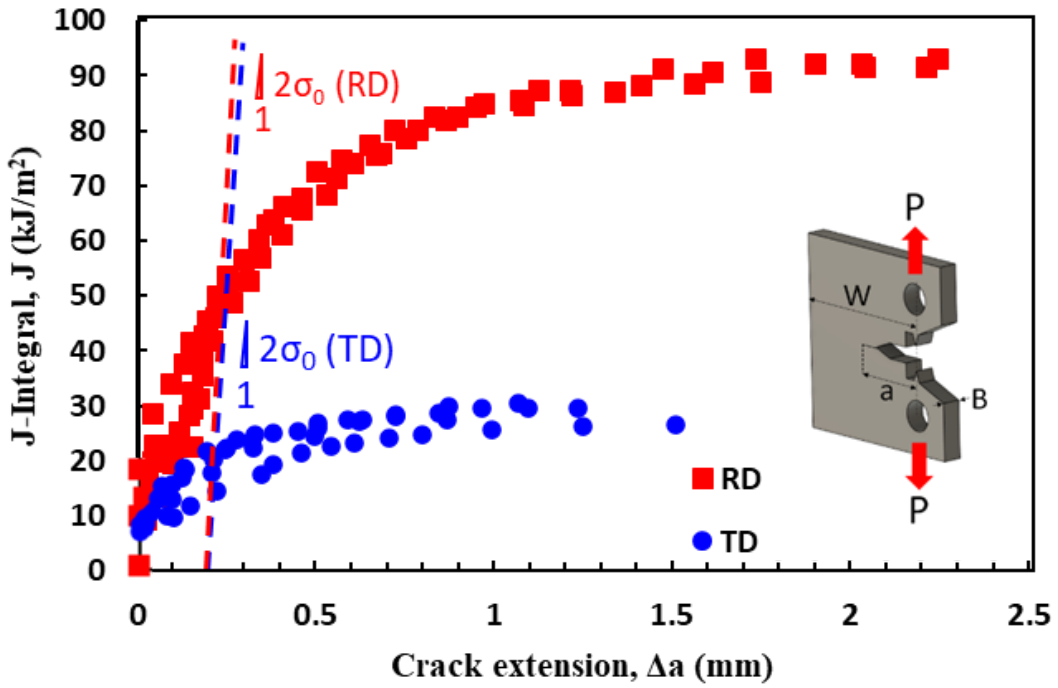

Figure 2.5: *J*-based R-curves for the D&P steel in both the RD and TD orientations tested at room temperature.

Table 2.2: Uniaxial tensile and fracture toughness properties of D&P steel

Property	RD	TD
Yield Strength* (MPa)	1978 ± 16 - 1916 ± 4 *	1714 ± 5
Ultimate Strength (MPa)	2144 ± 27	2048 ± 35
Elongation to Failure (%)	21.6 ± 0.8	8.3 ± 1.6
J-Integral at crack initiation J_{Ic} (MPa√m)	46.9 ± 4.0	19.6 ± 2.9
Fracture toughness K_{JIc} (MPa√m)	101.5 ± 4.3	65.4 ± 5

**For RD orientation, the first number is upper yield strength and the second is lower yield strength due to the yield point phenomenon. For the TD orientation, the yield strength is given as the 0.2% offset.*

2.4 CHARACTERIZATION OF FRACTURE

Examining the microstructure reveals the mechanisms that induce the high toughness in this alloy. Multiple sections of the RD and TD C(T) specimens were examined by scanning electron microscopy (SEM). These revealed multiple thin delaminations **Figure 2.6**. The cracks formed parallel through the ~1.4mm thickness of the sample dividing the sample into multiple thin layers. Different length scale delamination cracks formed creating multiple delamination bands **Figure 2.6**. The delaminations ligaments in D&P steel are significantly thinner than other materials that have delamination cracks[26], [27]. The TD delamination cracks are shorter in length and there are less of them than the RD samples. These through thickness sections and delamination cracks are further examined to gain a better understanding of the mechanisms of the delamination cracks **Figure 2.7**. The RD has short cracks (less than ~50um) and long cracks (more than ~50 um). In addition to these cracks there are thin cracks that are not connected to the fracture surface that are generally observed near the long cracks **Figure 2.7C**. It can clearly be seen that these delamination cracks occur almost exclusively along the PAGB's **Figure 2.7C.** The TD specimens only have short delamination cracks shorter than 50 um **Figure 2.7B**. The RD specimens have a much greater propensity for delamination cracking.

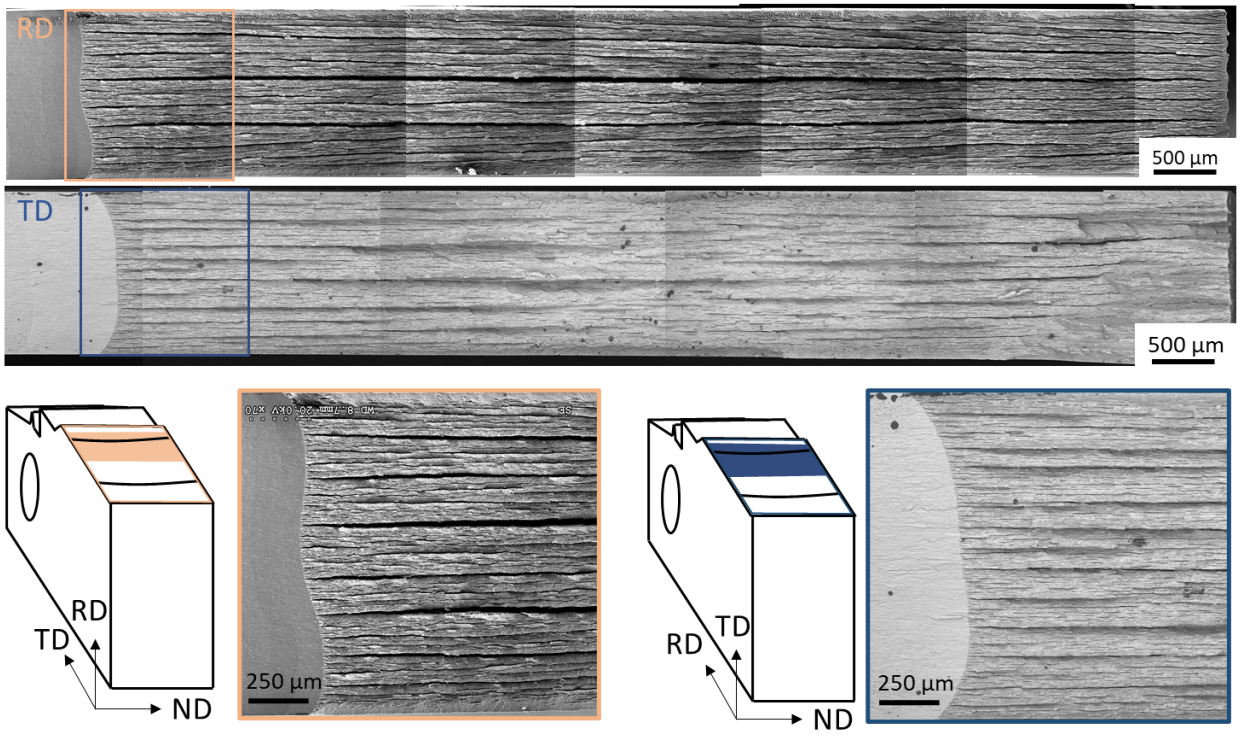

Figure 2.6: SEM images of the delamination seen on the fracture surfaces of D&P steel. They are the fracture surfaces of the C(T) specimens of both RD and TD.

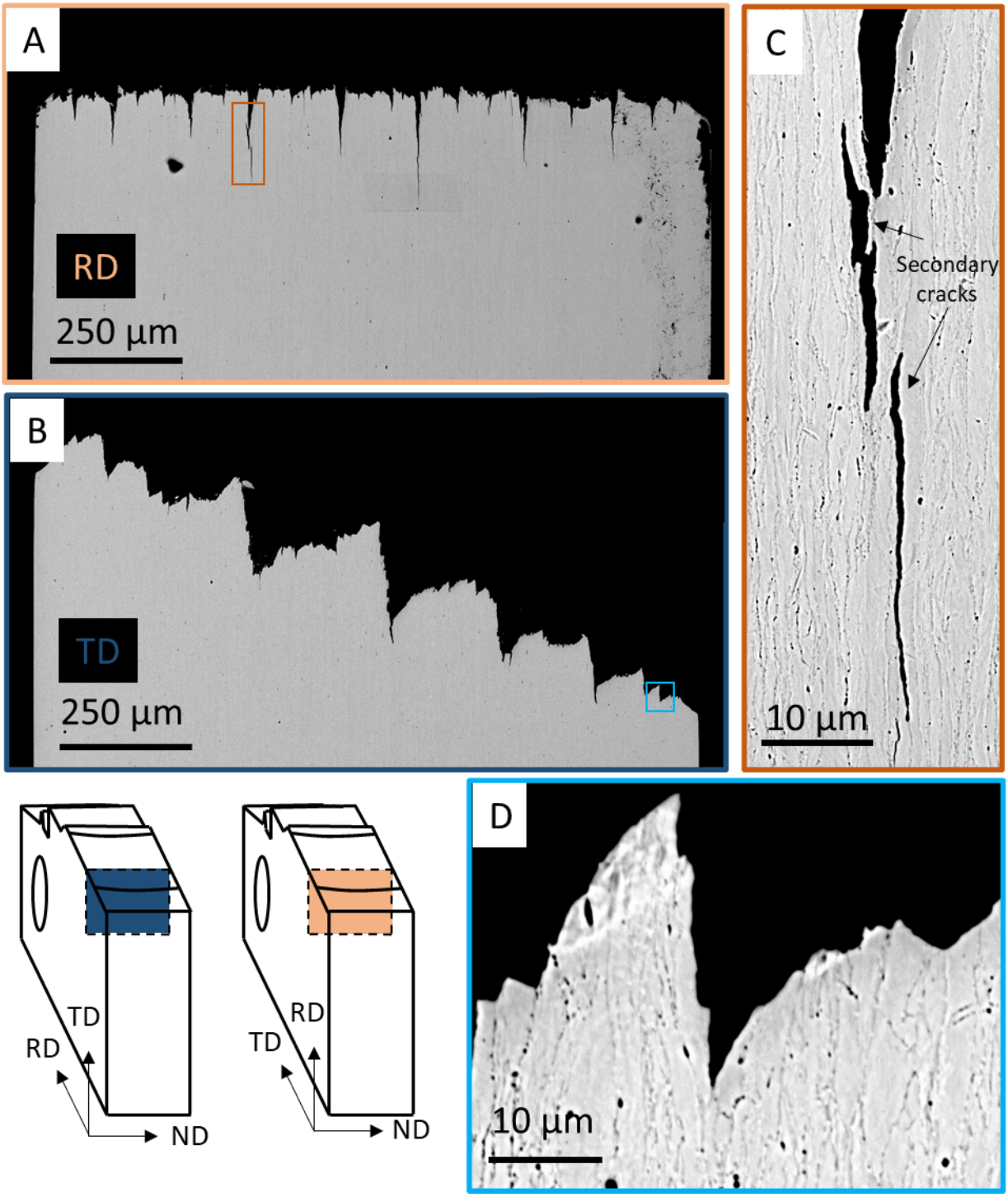

Figure 2.7: SEM images of the delaminations of the through thickness sections of both the RD and TD specimens in D&P steel.

2.4.1 Delamination Toughening

Delamination toughening can only be activated by relatively weak interfaces and mechanical stresses high enough to overcome the fracture stress of those relatively weak

interfaces. When the stress is high enough to overcome the fracture stress of the relatively weak interfaces then the delamination cracks can occur along these weak interfaces. From examining **Figure 2.7C & D** it is seen that the delaminations occur at the Mn-enriched PAGB's which are the relatively weak interfaces in D&P steel. These PAGB's act as the initiation and propagation sites of the delamination microcracks. In D&P steel, these PAGB's are not as strong as the grain interiors due to the Mn segregation, but still have a high cohesive strength [37], [38]. Because maraging steels have no interfaces or preferential sites with reduced cohesion for crack initiation and growth, even with its high yield strength, delaminations cannot form making delamination toughening not possible.

The mechanical driving force for delaminations is that for a sample in plane-strain conditions where there is a triaxial tensile stress state ahead of the crack tip. In front of the crack tip, the material is stressed in tension in the direction of the thickness (ND) of the sample shown in **Figure 2.8B**. If the tensile stresses in the ND are large enough to overcome the critical fracture stress of the Mn enriched weakened PAGB's then delamination occurs. For this to occur, the material needs to have high yield strength. A higher yield stress means an increased ND stress ahead of the crack tip. For many delamination toughening materials, the delamination toughening mechanisms do not activate until the material is at lower temperatures where the through-thickness stresses are larger and the interfaces may be more brittle. This low temperature activation mechanism means that several alloys including Al-Li alloys [26] and ultrafine-grained low alloy steels [39], [40] actually become tougher at cryogenic temperatures. D&P steel's high dislocation density and Mn-enriched PAGB's give the steel an ultrahigh yield strength and relatively weak interfaces respectively which provide the requirements for delaminations at room temperatures.

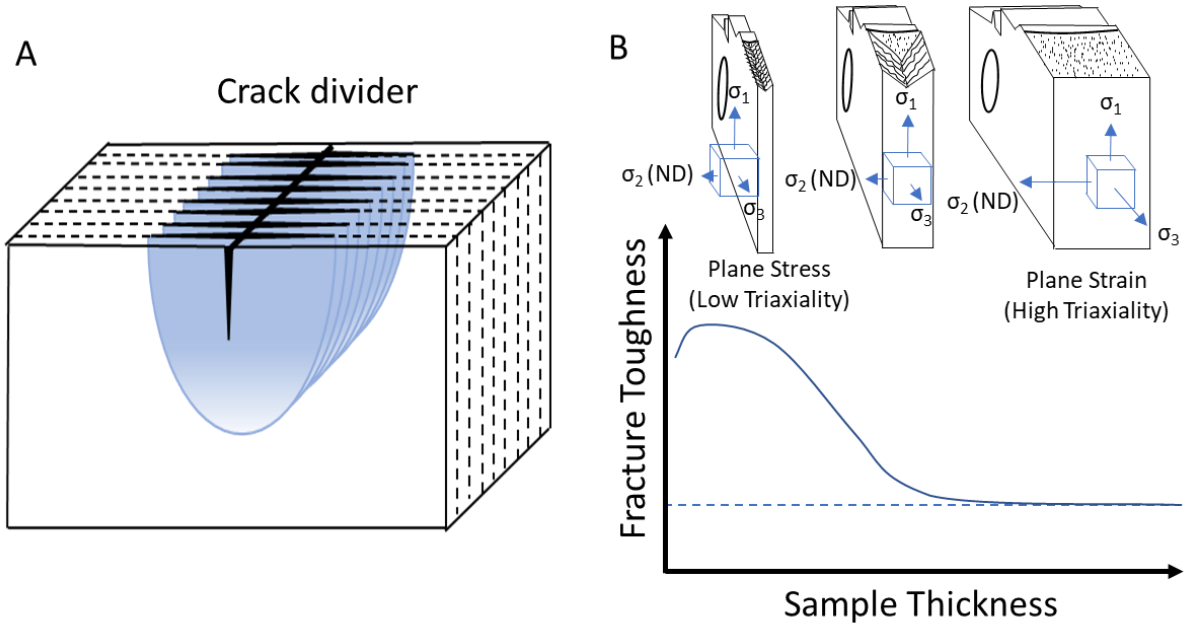

Figure 2.8: Schematic crack divider delamination toughening. B is schematic of how the thickness of the sample affects the fracture toughness.

Multiple delaminations ahead of the crack tip effectively transforms the expected plane strain condition into multiple parallel plane stress sections. These multiple plane stress ligaments have a much higher toughness than the same thickness sample in plane strain. In addition to this the generation of interfaces increases the energy consumption which increases fracture toughness. For D&P steel, the orientation of the sample and the orientation of the elongated grains affect the delamination toughening. The PAGB's are elongated and almost three times longer in the RD than the TD **Figure 2.2**. In the RD specimens, the main crack grows in the transverse direction while the delamination cracks propagate along the grains that are elongated in the RD **Figure 2.7**. This propagation allows for longer delamination cracks that more effectively divide the sample into many plane stress ligaments. In the TD specimens, the main cracks travel in the rolling direction when the delamination cracks propagate along the short side of the elongated grains. This reduced propagation reduces the delamination effect which effectively reduces the toughness in comparison to RD. In addition to this, as the TD specimen's crack grows, the crack tip encounters many PAGB's that are aligned perpendicular to the crack path. These grain boundaries effectively reduce delaminations, **Figure 2.7D**. The formation of these longer delamination cracks and shorter delamination cracks in RD and TD are directly related to the larger and smaller toughening effect that the samples experience.

2.4.2 Transformation-Induced Plasticity (TRIP) Toughening

D&P steel also exhibits TRIP toughening. TRIP toughening occurs when austenite is transformed into martensite in the vicinity of the crack tip as it grows. This leaves the crack path after propagation almost exclusively martensite. While not the primary TRIP toughening mechanism, martensite has a larger lattice parameter than austenite so as austenite is transformed to martensite at the crack tip a residual compressive stress is likely induced making the crack tips growth more difficult [41]. The main TRIP effect is that the transformation of austenite to martensite increases strain hardening. Strain hardening delays the onset of necking instability by enhancing uniform ductility which increases the intrinsic toughening by resisting crack propagation [31], [42].

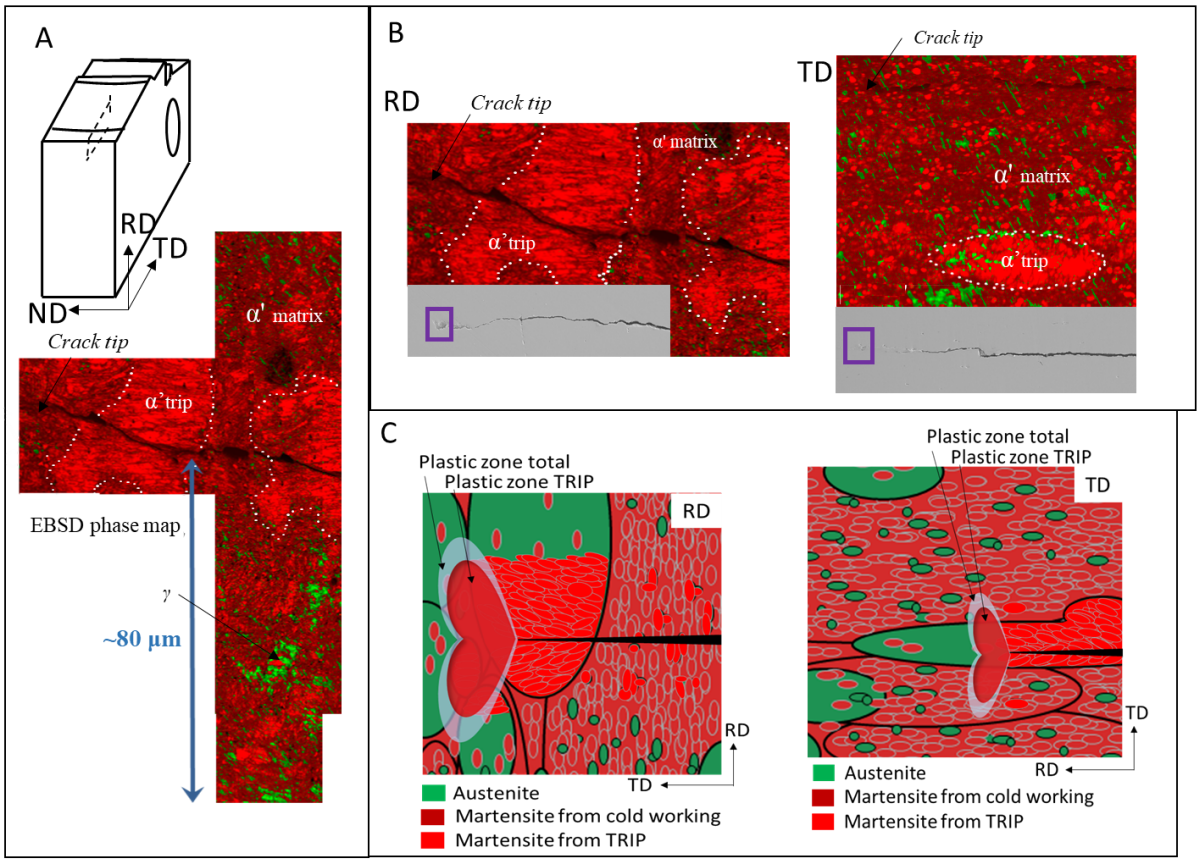

Figure 2.9: (**A**) Is an EBSD image of the mid plane of the crack tip of an RD C(T) specimen. It is an EBSD image quality map overlayed over the phase map of the crack and the area around it. Further away from the crack tip there is more untransformed austenite. (**B**) Shows a close up EBSD of the through thickness section of an RD and TD specimen. The lighter red section has a lower dislocation density and was transformed from austenite into martensite from the stress of the crack. The darker red areas were transformed when the material was cold worked during the materials processing. (**C**) Is a schematic that illustrates the structure of the material and the plastic zone ahead of the crack tip for RD and TD.

TRIP toughening is also affected by the orientation of the RD and TD. The RD specimen has a larger TRIP zone as the crack propagates perpendicular to the elongated austenite grains **Figure 2.9**. The TD specimen has a smaller TRIP zone because the crack grows in parallel to the elongated austenite grains [31]. **Figure 2.9B** shows the RD vs TD TRIP effect and zone sizes. The difference in higher and lower toughens between RD and TD are due to larger and smaller trip toughening zone size.

2.5 SUMMARY

D&P steel exhibits high damage tolerance and strength. **Figure 2.10** is an Ashby plot that shows how D&P steels fracture toughness and yield strength compare with the best structural materials available. D&P steel has a similar yield strength as maraging steels and still has almost double the initiation fracture toughness of maraging steel. D&P steel has a toughness similar to titanium alloys but is twice as strong. D&P steel's incredible strength and toughness show the benefits of high strength induced multi-delamination toughening mechanism. This mechanism

allowed for the maximization of strength and toughness while reducing the cost of the material. The main components of this delamination toughening is the high yield strength in combination with still strong, but relatively weak interfaces. This design principle of high strength and weakened interfaces can be exploited to improve the toughness of existing ultrahigh strength materials.

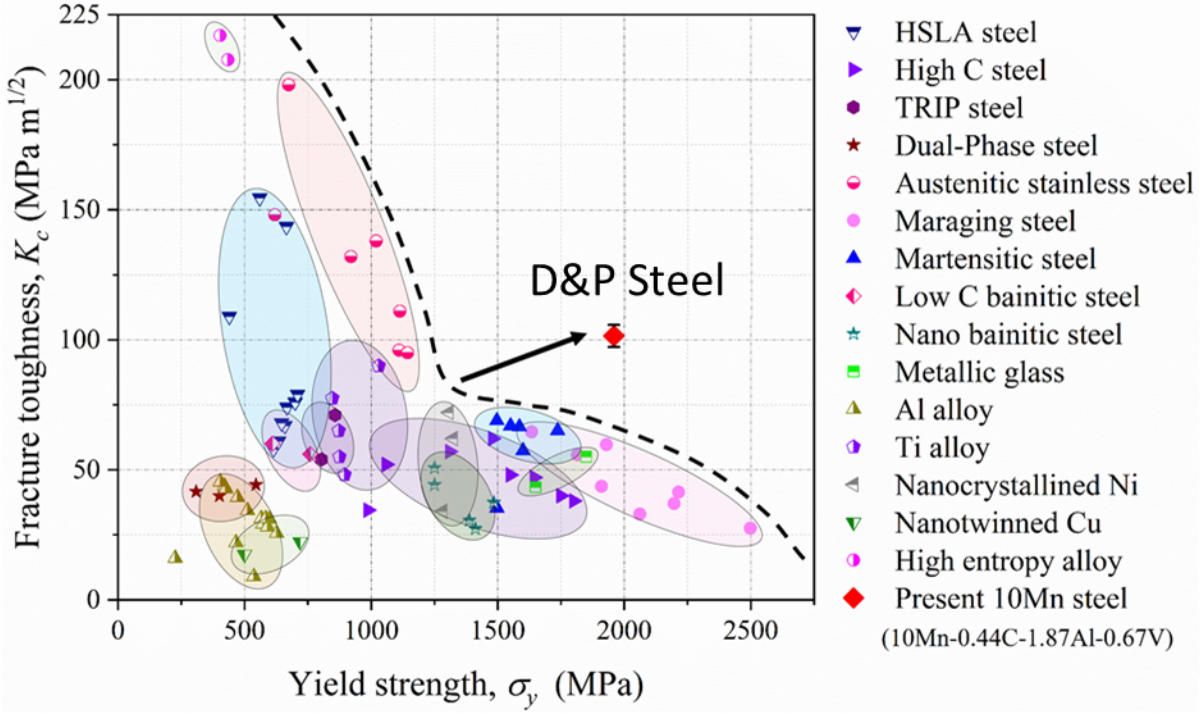

Figure 2.10. Is an Ashby plot of fracture toughness versus yield strength. D&P steel has a better strength toughness trade off than the best existing structural materials including: high strength low alloy (HSLA) steels [43], [44], high carbon (C) steels [45], TRIP steels [46], dual-phase steels [47], austenitic stainless steels [48], [49], maraging steels [33], [34], [50], martensitic steels [51], [52], low C bainitic steels [53], nano bainitic steels [54], metallic glass[55], Al alloys [56], Ti alloys [57], nanocrystalline Ni [58], nanotwinned Cu [59], and high-entropy alloys [15], [16].

Chapter 3
X-ray Tomography of Tristructural Isotropic Nuclear Fuel Particles

3.1 INTRODUCTION

Tristructural isotropic (TRISO) coated nuclear fuel particles were invented as part of the Dragon Reactor Project in the United Kingdom [60], [61], and have become widely used. These TRISO particles have been used in the Thorium High-Temperature Reactor [62], [63] (THTR-300, Germany), HTR-10 [64] (China), the High Temperature Test Reactor [65], [66] (HTTR, Japan), and Xe-100 (U.S.) [60]. These TRISO particles are being considered for use in the next generation high temperature gas cooled reactors [7] and very-high-temperature reactors [8]. These reactors include the pebble-bed reactor (PBR) and prismatic-core configurations (e.g., the Russian design of GT-MHR). They are also being considered for fluoride salt-cooled reactors (FHR) (e.g., by Kairos Power, U.S.) and in next generation light water reactors [67], [68]. Finally, TRISO particles are also involved with the light water reactor fully encapsulated fuel concept for accident tolerant conditions [69]–[71].

TRISO particles are most often composed of five layers [72]. The core is the fuel kernel which is generally an oxide and/or carbide of Uranium, Plutonium, or Thorium. Around the core there is usually a ~50% porosity low density layer of pyrolytic carbon. This layer accommodates for thermal expansion and acts as a reservoir for fission products. Surrounding the low density pyrolytic carbon, is a layer of dense pyrolytic carbon (IPyC). The next layer is silicon carbide, and the outer layer is pyrolytic carbon (OPyC). The silicon carbide layer contains the internal pressure during the fusion reaction and acts as a diffusion barrier for fission products. This SiC layer is loaded in compression as the dense pyrolytic carbon layers shrink during irradiation [73], [74].

This study utilized *in situ* X-ray computed tomography (XCT) [75], [76] to examine how the four unirradiated TRISO particles fail in compression at 1000 °C and room temperature (RT). The TRISO particles used in this study were supplied by the *pyrocarbon irradiation for creep and swelling/shrinkage of objects* neutron irradiation experiment [77]. XCT allows for observation of the initiation and propagation of cracks. Crushing tests were chosen over semi-sphere/shell pressurization/bending [78]–[81] because the particles have a simple geometry and crushing requires no sample preparation which makes it more viable for future tests involving irradiated samples [78]. However crushing tests have localized stress zones where the sample contacts the anvil, and the hardness of the anvil affects the maximum load to failure [82], [83]. While a soft anvil enables latitudinal tensile stress on the particle surface, a high hardness anvil will induce local bending stresses at the contact point which maximizes stress on the inner surface of the SiC.

The difference in layers that make up the TRISO particles have a marked effect on their failure modes but this has never been fully characterized [84]–[86]. Specifically, the failure mechanisms have also not been examined at elevated temperatures. Some annealed particles

have been examined [83], [84], [87], [88], but they require being cooled to room temperature before examination. This cooling could cause different residual stress states and changes in cracking patterns. This study seeks to understand these gaps in understanding: the crushing behavior of TRISO particles at high temperatures with simultaneous *in situ* 3D non-destructive imaging. I performed all of the sample loading, temperature calibration, sample alignment, and exposure time adjustment for the best possible images. I also performed the testing by loading, heating, and taking the scans. I was also involved with finding the center of rotation of the scans and some preliminary analysis.

3.2 MATERIALS AND EXPERIMENTAL PROCEDURES

3.2.1 Tristructural Isotropic Particles Structure and Processing

This work examines two types of simplified TRISO particles, which are known as PyC-1 (Kernel/Buffer/PyC) and PyC-2 (Kernel/Buffer/SiC/PyC); both of which are shown in **Figure 3.1**. PyC-1 does not contain SiC which creates conditions that allow for unrestrained dimensional changes, and allows for a better understanding of the SiC layer's effects on mechanical properties through comparison between both particles. These TRISO particles only have three and four layers, respectively, since they only contain one layer of dense pyrolytic carbon (PyC). The core kernel was made of alumina because its behavior in a reactor has been recorded in the literature [77] and it is readily available in high-purity which negates any impurity effects during irradiation.

The samples were prepared through the deposition of the buffer carbon on the alumina kernel at 1350 °C in an acetylene and argon environment. The SiC was deposited at 1560 °C in a methyltrichlorosilane and hydrogen environment. Finally the PyC was deposited at 1340 °C in an acetylene with propylene and argon environment [89].

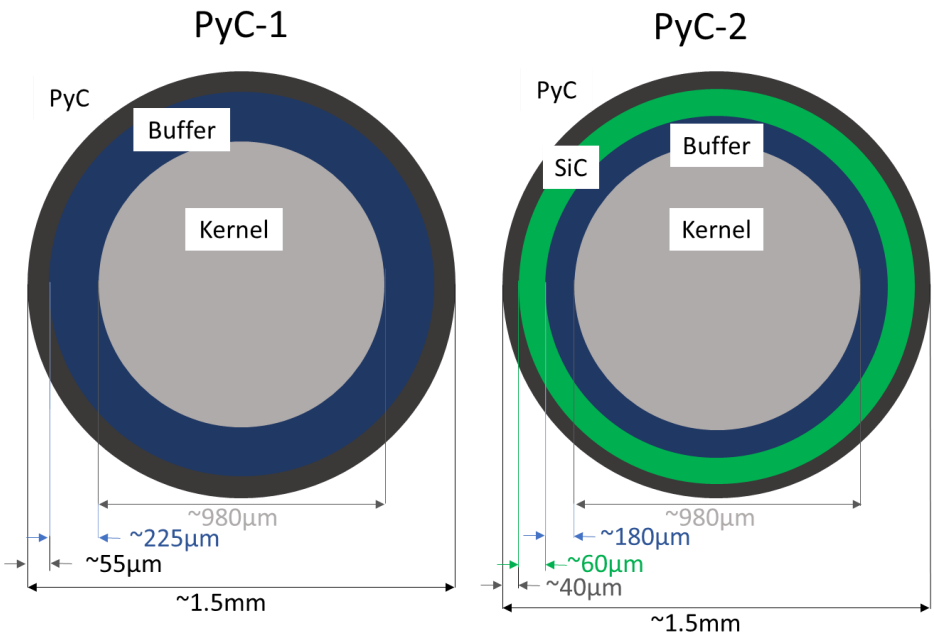

Figure 3.1: Diagrams of the internal structure of the PyC-1 (left) and PyC-2 (right) TRISO particles being tested.

3.2.2 Testing Procedure

The 8.3.2 tomography beamline at the Advanced Light Source (ALS) synchrotron at Lawrence Berkeley National Laboratory was used to perform *in situ* tomography experiments on the TRISO particles. The beamline consists of a tomography setup that can scan samples and create 3D images of the entire surface, as well as all interior features. This test is nondestructive and can be performed many times on the same sample. At the 8.3.2 beamline, the imaging technique is paired with a load frame with a built in furnace that can heat samples to 1200 ℃ [75], [76], as shown in **Figure 3.2**. Broadly this load frame/heating fixture consists of a screw-driven load frame with a ~150-mm diameter water-cooled chamber. The chamber holds six 150W light bulbs with elliptical, gold reflectors that focus the light on a ~5-mm diameter spherical region in the center of the chamber. This chamber is divided in half with a thin aluminum window at the equator of the sphere that allows for X-rays to pass through it to image the samples being tested inside. A detailed explanation of this device can be found in reference [76], [90]. The pairing of heating, mechanical deformation, and imaging allows for samples to be fully imaged then deformed under extreme temperatures if desired, and then imaged again to examine internal mechanisms in the material. Where this technique excels is in the testing of complex microstructures and macrostructures. The tomography procedure used a monochromatic beam of 25 keV measured by the detector (PCO Edge 5 × CCD camera (2560 × 2560)). The field of view was 3.3 × 3.5 mm giving a pixel size of 1.3 × 1.3 μm.

The anvil sample holders were made of alumina. The materials of the platens used to crush TRISO particles are usually alumina or SiC [84], but aluminum [83] and steel [85], [86] have also been utilized. Alumina rods were used as they needed to have high strength and hardness at high temperatures, and would only need to be used in compression. These are shown in **Figures 3.2C** and **3.3**. A loading displacement rate of 0.5 μm/s was used to ensure a quasi-static loading condition. A scan of the entire sample was taken before loading and then at several points during the loading process until fracture. These scans provide real time information of damage evolution by imaging the porosity, crack formation, and layer thickness changes *in situ*. The PyC-1 and PyC-2 each had two samples, of these; one was tested at room temperature and one was tested at 1000 °C. Before heating a thermocouple is attached to the sample to measure the sample's temperature as it is heated. The loading needed to be stopped for each scan to take place. A scan for this material took ~10 minutes and any movement of the sample during a scan would ruin it and make it blurry, due to a change in position of the sample part way through. This is why the samples were loaded then stopped so a scan could be taken, and then reloaded and repeated. During each scan, 1969 projections were collected while rotating 180°. Each projection took 300 ms and fifteen images were taken before and after each scan to subtract the background. The Gridrec algorithm and the TomoPy package were utilized to reconstruct the scans after the center of rotation was manually identified for each scan. For normalizing the projection images and reducing the detector's fixed pattern noise, a flat field correction method was utilized. Explore [5] for more information. This technique is limited as it cannot be used to image tiny features since these scans have a pixel size of 1.3 × 1.3 μm so micron sized flaws cannot be observed.

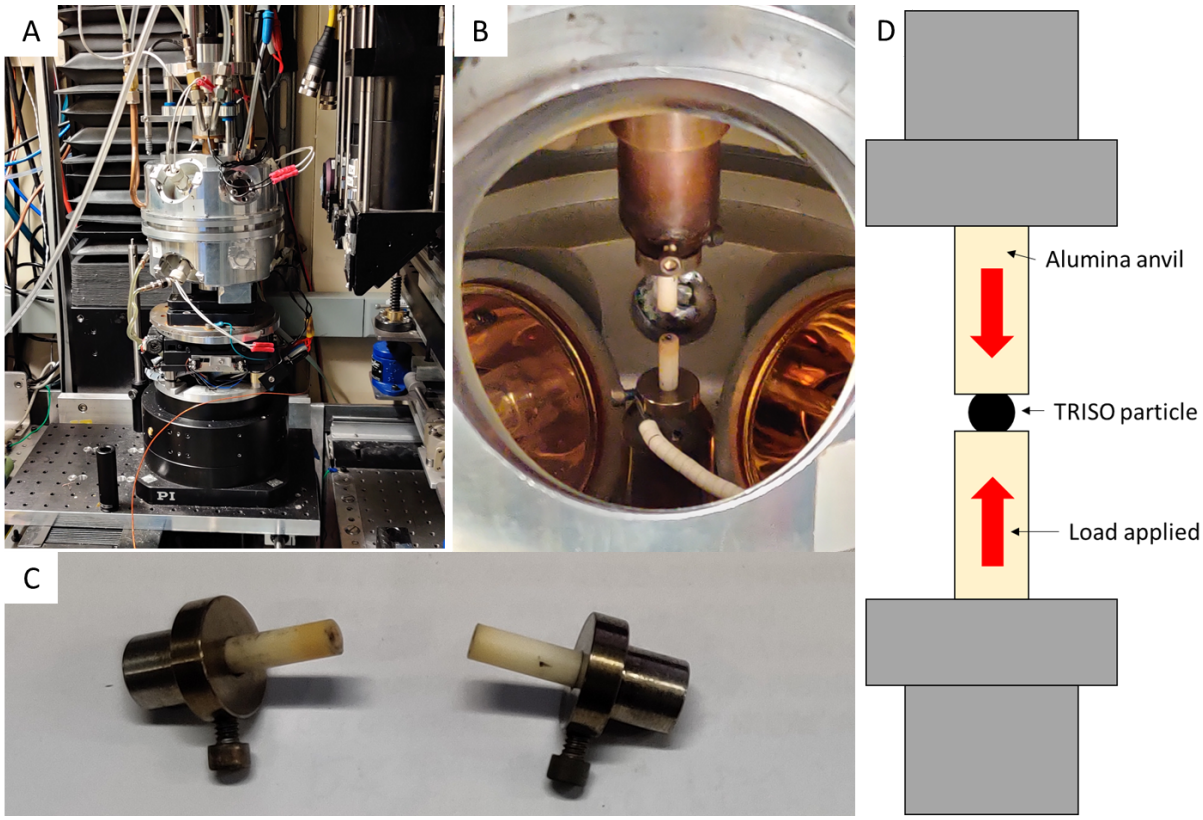

Figure 3.2: Image of the load frame hot cell at the 8.3.2 tomography beamline. Image (**A**) shows the outside of the load frame hot cell. (**B**) Inside of the load frame with mounted aluminum compression fixtures. (**C**) Alumina anvils used to compression test the TRISO particles. **(D)** A diagram of the alumina anvil compression fixtures used to test the TRISO particles at RT and 1000 ℃.

3.3 RESULTS

3.3.1 Temperature Effects on Particle Strength

Due to the limited number of TRISO particles, *in situ* imaging under load using XCT is extremely critical. This imaging can show any defects, or a lack thereof, that could cause a strength reduction, and provides exact measurement of the microstructure and dimensions of each of the layers in the TRISO particles. The scans before loading are performed to measure the thickness of each layer, as shown in **Table 3.1**. The sizes of TRISO particles are very consistent with a difference in dimensions of <5% between the two samples of each type, and no major defects were found. From this, it can be assumed that changes in loading curves and measured strength is due to the changes in temperature and not due to sample differences. Argon gas was used in every test for consistency even with no risk of oxidation at room temperature.

Table 3.1 Dimensions of the four particles tested using *in situ* XCT

Type	Test temperature (℃)	Kernel (μm)	Buffer (μm)	SiC (μm)	PyC (μm)	Whole sample (μm)
PyC-1	RT	988.8 ± 7.2	235.5 ± 8.9	N/A	56.6 ± 0.4	1579.4 ± 11.5
PyC-1	1000	982.9 ± 3.6	218.1 ± 11.6	N/A	54.1 ± 3.1	1540.6 ± 14.1
PyC-2	RT	980.1 ± 2.7	184.4 ± 6.7	60.1 ± 2.5	40.8 ± 2.2	1568.1 ± 14.5
PyC-2	1000	976.5 ± 3.2	174.4 ± 6.8	62.8 ± 2.2	39.1 ± 2.1	1543 ± 14.6

Figure 3.3A shows the load-displacement curves of the TRISO particles at RT and 1000 °C. It can be seen that the PyC-1 both fractured at similar loads at RT and 1000 ℃. The PyC-1 tested at 1000 ℃ is dimensionally slightly smaller with thinner layers than the sample tested at room temperature, which decreases its load at failure as compared to the larger RT PyC-1. Furthermore, there are several load drops in the load-displacement curve highlighted by the arrow on **Figure 3.3**. These load drops are due to the relaxation of the TRISO particle when the loading was stopped for about 10 minutes to take XCT scans. The load drops are slightly larger at ~9 N at 1000 °C and ~6 N are RT. The small pop-ins seen under 40 N are likely due to the formation of small cracks or the crushing phenomena and will be explored in section 3.3.2.

Linear fitting allowed for the slope of the load-displacement curve to be determined. Increases in the slope were seen at higher loads for both RT and 1000 °C. At RT between 30 and 40 N the slope was 0.583 ± 0.018 N/μm, and between 45 and 90 N the slope was 0.655 ± 0.006 N/μm. The representative modulus cannot be easily determined from these curves, but it can be seen that the particles fail abruptly and catastrophically without first showing signs of yielding or impending failure.

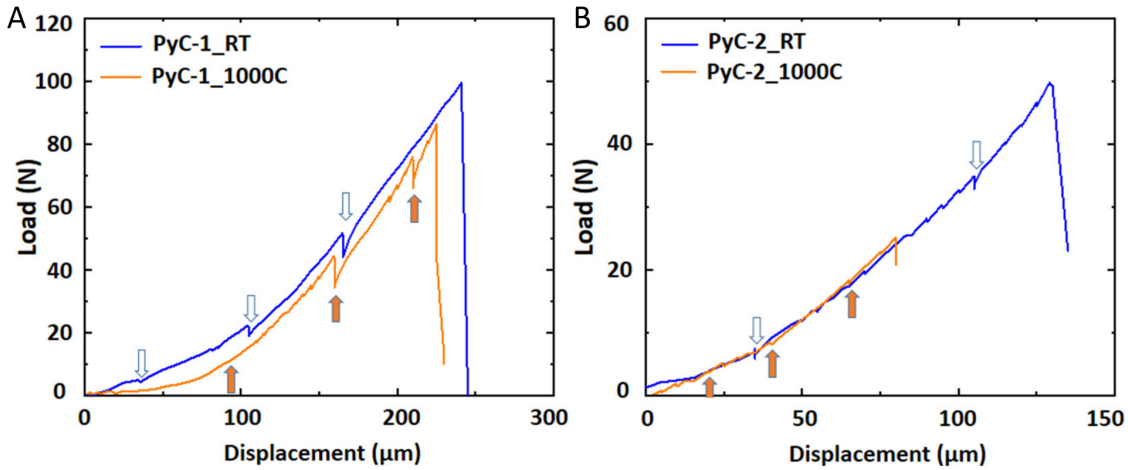

Figure 3.3: Load-displacement curves for (**A**) PyC-1 particles at RT and 1000 °C and (**B**) PyC-2 particles at RT and 1000 °C. The arrows indicate the load drops where the loading was stopped to take a tomography scan [5].

Figure 3.3B shows the load-displacement curves of PyC-2 particles at RT and 1000 °C. Unlike PyC-1, PyC-2 which contains the layer of SiC had a reduced failure strength of ~45% (compared to PyC-1) at 1000 °C even with similarly sized PyC-2 particles (**Table 3.1)**. From the XCT scans, it can be seen that this reduction of strength was not due to intrinsic defects such as voids and microcracks. Therefore, the SiC layer itself causes the reduction in failure strength at 1000 °C. The failure mechanisms will be discussed in section *3.4*. The arrows in **Figure 3.3B** shows where the loading was stopped to take a XCT scan. Unlike PyC-1, PyC-2 has very small load relaxation drops during the scans at both RT and 1000 °C. The slopes of the load-displacement curves were consistent. At RT with a load of 20 to 30 N the slope was 0.417 ± 0.013 N/μm, and at 35 to 45 N 0.588 ± 0.018 N/μm. At 1000 °C with a load of 10 to 20 N the slope was 0.395 ± 0.006 N/μm and at a load of 20 to 25 N 0.528 ± 0.024 N/μm. The PyC-2 particles failed brittlely at both RT and 1000 °C. Even with only one sample tested at each temperature, the lack of flaws seen in XCT scans, the consistency of the fracture behavior, and the load line displacement consistency, it can be concluded that it was the high temperature along with the SiC layer that caused the reduction in failure strength.

3.3.2 Temperature Effects on Fracture Mechanisms

Each sample was scanned by tomography before loading, multiple times during loading (arrows in **Figure 3.3**), and after final fracture. All scans show cracks and voids 2-3 times the pixel size of the tomography scan, but were likely not the cause of a reduced failure strength. The main aspects that were analyzed were the compressive deformation, the dilation at the equator, and crack formations prior to failure.

To measure the compressive deformation and equator enlargement, two orthogonal slices were manually selected with the largest diameter, the loading plane XZ and the equatorial plane XY shown in **Figure 3.4**. By identifying the edge of the grayscale profile, the diameter of the particles can be determined. To measure the average diameter, each slice diameter was measured 12 times with each having an offset of 30 degrees to cover the whole surface; these diameters were then averaged. This is partially shown in **Figure 3.4C**. These diameter measurements had an error of ± 10%.

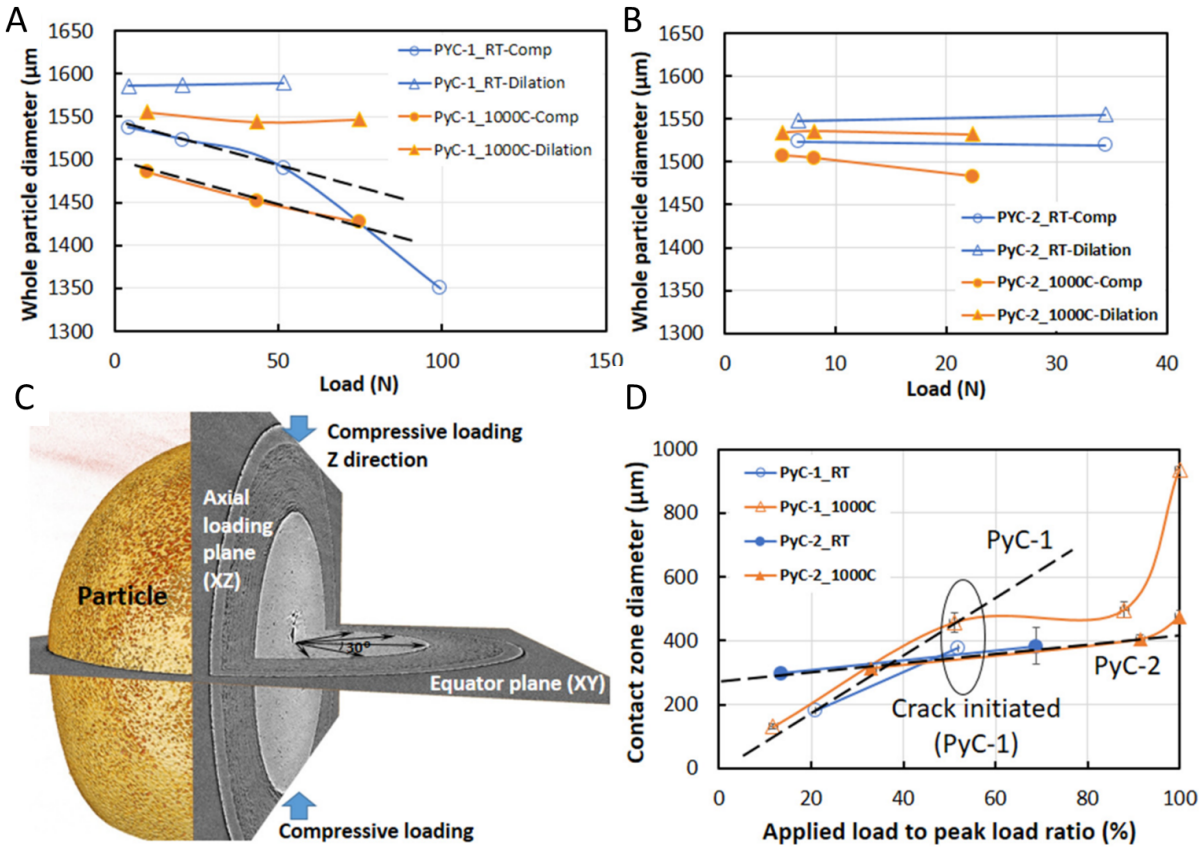

Figure 3.4 (**A**) The equator dilation and load line (z-axis) deformation seen in XCT scans of the PyC-1 particles tested at RT add 1000 °C. (**B**) The dilation and load line (z-axis) deformation seen in XCT scans of the PyC-2 particles tested at RT add 1000 °C. (**C**) A schematic of the axial loading (XZ) and equatorial (XY) planes and the bFlack arrows represent some of the diameters used to calculate the average particle diameter (**D**) the contact zone area diameter as a function of the applied load to peak load ratio [5].

For PyC-1, in the equatorial plane (XY), no measurable changes in equatorial dilation were observed at either RT and 1000 °C seen in Figure **3.4A** (triangles). This indicates that there is no major separation between layers until final failure. Significant changes were seen along the loading direction in the z-axis, as shown in **Figure 3.4A** (circles). Both RT and 1000 °C experienced significant reduction of the diameter in the z-axis as the load increased. Below 75% of the failure load, the gradients describing the change in the whole particle diameter with load were similar, which was expected as the load-displacement curves are very similar. This is shown by the two parallel dashed lines in **Figure 3.4A**.

PyC-2 samples also experienced no significant change in the equatorial diameter as shown in **Figure 3.4B** (triangles). Due to the SiC layer in PyC-2 it experienced much lower deformation along the load-line z axis (**Figure 3.4B** circles). The PyC-2 sample tested at 1000 °C had a much larger deformation along the load z axis than the RT sample shown in the circles of **Figure 3.4B**. The diameters in the load line direction were examined and it was found that the SiC layer did not change thickness but the PyC and the buffer layer were both compressed significantly more at 1000 °C. It was compressed ~37 µm at 91% failure load at 1000 °C and at a linear extrapolation equivalent of ~16 µm at 91% failure for RT. Unlike PyC-2, The PyC-1

samples with no SiC layer had a similar deformation at RT and 1000 °C of 45 μm at 51.9% of failure load and 36 μm at 51.1% of failure load, respectively. The SiC layer has a significant impact on the axial depression behavior at high temperatures.

Crushing the samples did not induce significant expansion in the equatorial plane which would be seen in a fully elastic material like a rubber ball. The deformation was instead concentrated at the points of contact where the sample met the alumina anvils. **Figure 3.4D** shows the mean contact diameters of the samples, and how they change with load. These loads are normalized against the maximum load at failure. At 1000 °C the PyC-1 sample had a 20% larger contact area than the RT sample. Below 60% of the failure load the contact sizes were similar between RT and 1000 °C. The contact area of the samples remained unchanged as the load increased until 90% of failure load, where there is an increase just before fracture. PyC-2 samples instead showed a linear increase in contact area for both RT and 1000 °C up to 90% of failure. The increase in the PyC-2 sample contact area was at a much lower rate than that of PyC-1, which is consistent with the inclusion of the SiC layer and the decreased load line displacement.

How the cracks were initiated and the samples overall failure was very different between PyC-1 and PyC-2. These differences are illustrated between **Figure 3.5** (PyC-1) and **3.6** (PyC-2). At RT the PyC-1 sample had two cracks form at ~50% failure load shown in **Figure 3.5A**. The cracks extended from the outer PyC layer (**Figure 3.5A**) down into the buffer layer (**Figure 3.5B)**. When the particle failed it fractured into many pieces shown in **Figure 3.5D** and **F**. The PyC-1 sample tested at 1000 °C started with a single crack in the PyC layer which started at a similar load as the RT sample (**Figure 3.5C**). At failure, this initial crack grew completely to split the particle from pole to pole seen in **Figure 3.5E** and **G**. The crushing of the outer PyC layer created small cracks and is the cause of the pop-ins seen while loading (**Figure 3.3**).

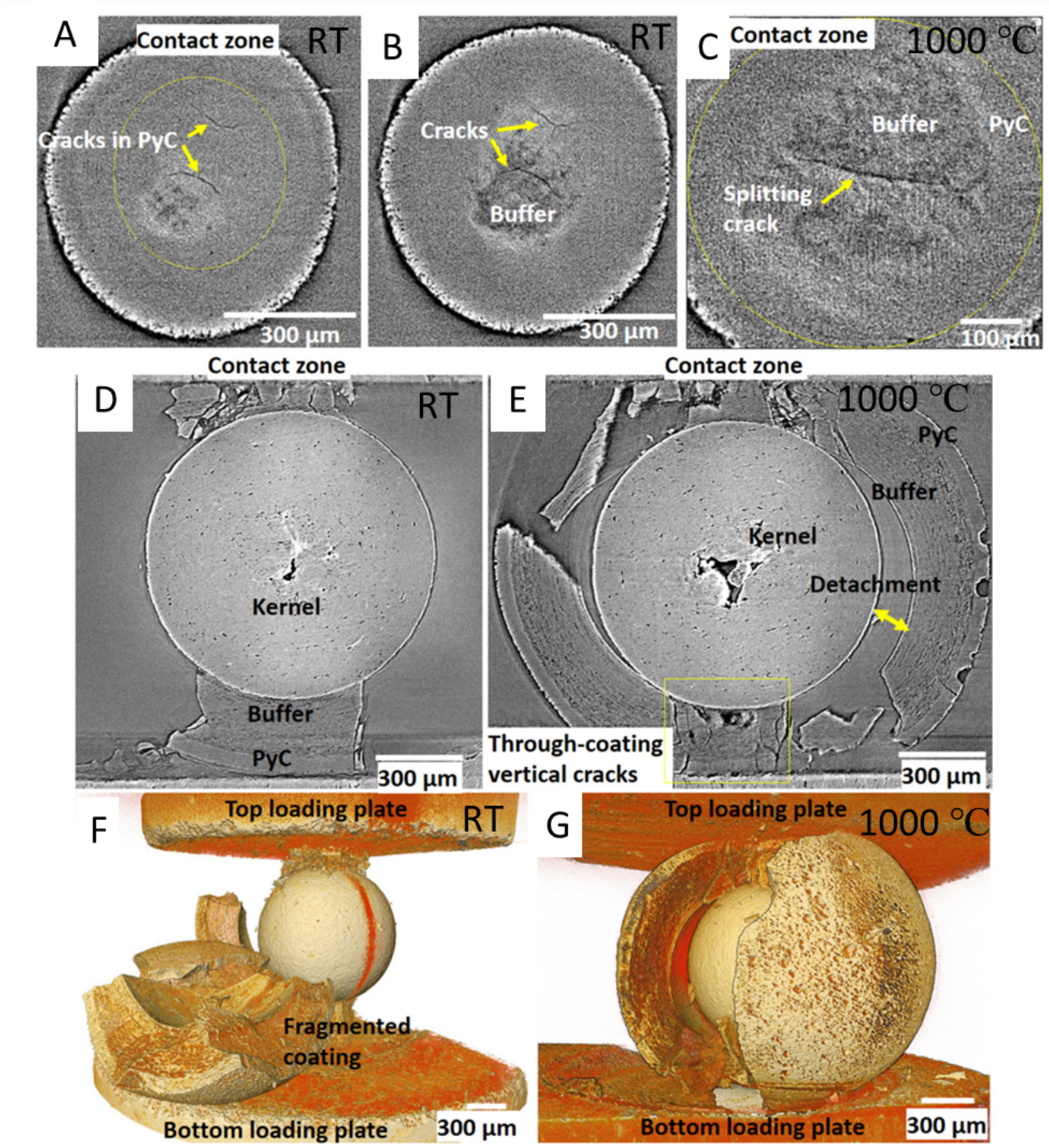

Figure 3.5: Is the tomography scans and reconstructions of PyC-1 TRISO particles tested at RT and 1000 °C. (**A**) Is the contact zone of the outer layer PyC and the alumina fixture at RT, (**B**) is the interface between the PyC layer and the buffer material below it at RT. (**C**) The buffer layer at 1000 °C. Image (**D**) and (**F**) are the 2D and 3D reconstruction respectively of these samples at RT. Image (**E**) and (**G**) are the 2D and 3D reconstruction respectively of these samples at 1000 °C [5].

The PyC-2 samples showed no cracks large enough to be observed by XCT before the catastrophic failure. The cracks at the contact area are somewhat circular seen in **Figure 3.6A** and **B**. Generally when a load is applied to two curved surfaces they are deformed slightly and the maximum tensile stress occurs on the surface a distance away from where the surface is contacted. This is a conventional Hertzian contact problem. Unlike standard Hertzian cracks these circular ring cracks formed inside the contact area due to the steep strain gradient formed on the surface of the flat anvil. While after failure both the RT and 1000 °C samples had many fragmented cracks at the contact zone the RT sample had significantly more cracks, seen in **Figure 3.6CA** and **B**. The cracks in the RT sample penetrated through the PyC and the SiC layers into the buffer material which caused failure, and delamination between the SiC and the buffer layer was observed. The PyC-2 sample tested at RT failed in more pieces than the 1000 °C, the same as what was seen in the PyC-1. The RT PyC-2 sample had many longitudinal cracks through the three outer layers breaking the sample into multiple pieces seen in **Figure 3.6E**. In the sample tested at 1000 °C, just a single crack penetrated the SiC and buffer layer which fractured the sample as shown in **Figure 3.6F**. The additional small cracks (**Figure 3.6B**) that were formed around the contact zone did not fully penetrate all the way through the PyC SiC and the buffer layer.

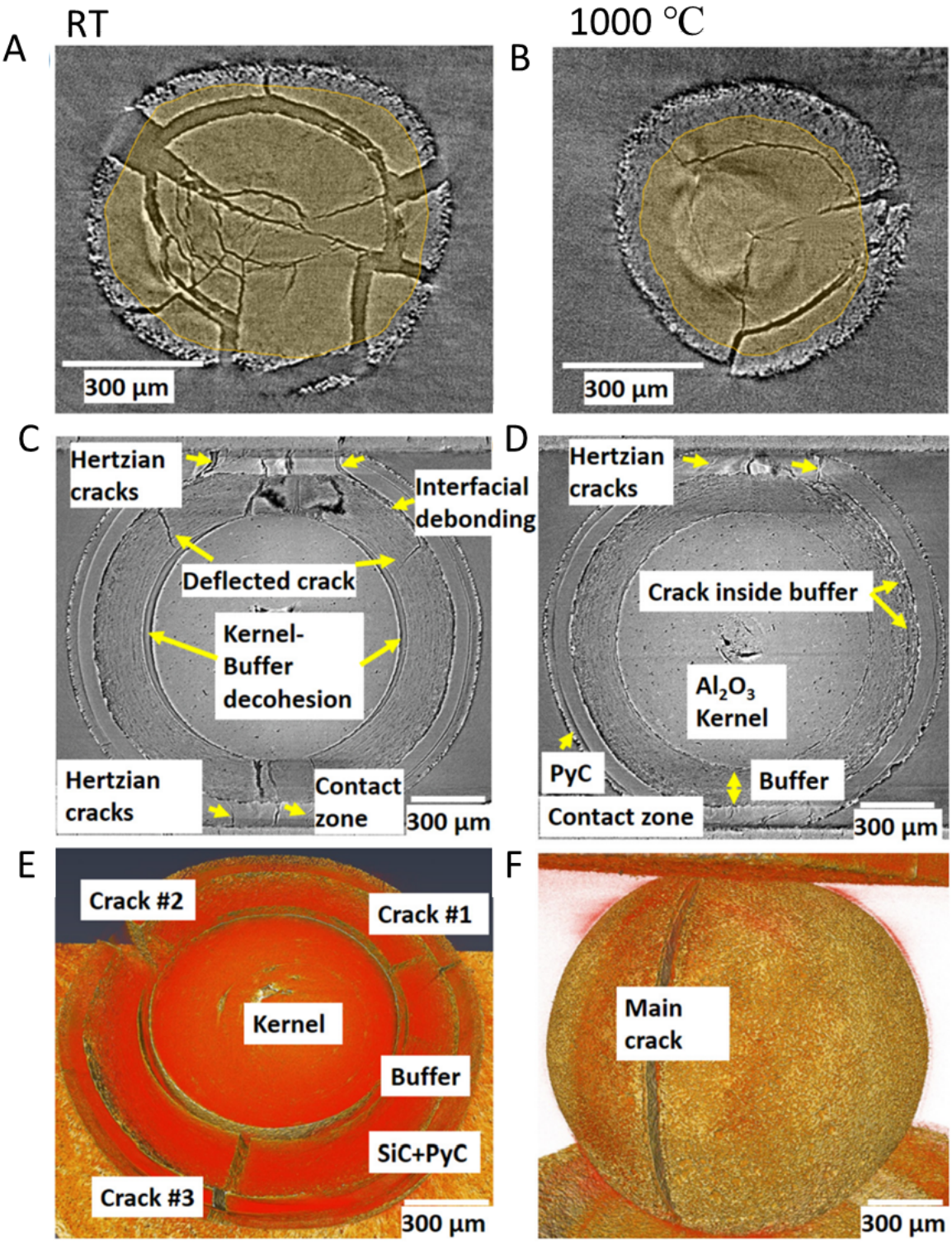

Figure 3.6: Is the tomography scans and reconstructions of PyC-2 TRISO particles tested at RT and 1000 °C. (**A**) Is the contact zone of the outer layer PyC and the alumina fixture at RT, (**B**) Is the contact zone of the outer layer PyC and the alumina fixture at 1000 °C. Image (**C**) and (**E**) are the 2D and 3D reconstruction respectively of these samples at RT. Image (**D**) and (**F**) are the 2D and 3D reconstruction respectively of these samples at 1000 °C [5].

At RT the cracks emanating from the PyC-2 contact zone after penetrating the PyC and SiC layers do not immediately penetrate into the buffer layer and instead travel along the SiC-buffer interface before entering the buffer (**Figure 3.6C)**. **Figure 3.6C** shows that some of the cracks went deep enough to cause core-buffer delamination. There was less crack deflection at the SiC-buffer interface in the 1000 °C, instead the cracks propagated into the buffer layer and then traveled through these layers to the contact zone on the other side of the particle seen in **Figure 3.6 D** and **F**.

Many samples are required to determine a material's properties with statistical significance. However the entire sample real time small resolution imaging of the XCT during loading allows for the understanding and characterization of the failure mechanisms with only small numbers of samples. It was observed that the temperature and SiC layer affected the strength, how cracks initiated, and the failure patterns.

3.4 DISCUSSION

*3.4.1 Hertzian Contac*t

In a conventional Hertzian contact problem, the elastic modulus and curvature of the two contact materials determines the degree of deformation and stress [91]. In this setup, the maximum stress created vertical cracks that occurred inside the contact zone. These are not the mechanisms that were suggested by Briggs et al. [84], which were that the outer coatings would separate at the end of the Hertzian contact.

Without the SiC layer the outer PyC layer must have experienced a splitting tensile stress in the center of the contact zone at RT and 1000 °C. With the SiC layer no observable cracks formed prior to fracture. The PyC-2 samples had complex final fracture patterns. It had circular cracks outside the contact zone that would usually form inside the contact zone, and had many angled cracks emanating from the point of contact.

Alumina was utilized as the anvil material over SiC because of its strength at high temperatures and its lower hardness and stiffness compared to SiC, which causes lower local stresses. Due to the material mismatch between the anvil and TRISO particle, the initial surface flaws can be affected because of a sticking condition that can occur from sample radial shearing due to a resistance to lateral displacement. Therefore, the observations of the cracks forming inside the contact zone is not unexpected. From the XCT imaging, it can be determined that there is not one failure mechanism that encompasses all of the different types of TRISO particles with different coatings. Thus, the strength of these particles is dependent on the material type, thickness, and number of layers.

3.4.2 Strength Reduction in PyC-2 at 1000 °C

PyC-1 retained its strength at 1000 °C while the PyC-2 sample had a significantly reduced crushing strength at 1000 °C. The crushing load for TRISO particles has been shown to be reduced by 30% after having experienced a heat treatment [78], [85], [86], [88], but this has

not been fully explained. The current theory is that there are residual stresses due to the differing thermal expansion coefficients [92].

Delle et al. [93] used the crushing particle strength to determine the roll of residual stresses. They related the strength of the coating material (σ_N) to the cruising load (F_N), the coating layer residual stresses (σ_r), and the force transmitted to the kernel (F_k) by:

$$\sigma_N = \frac{F_N - F_k}{\pi\left(R_O{}^2 - R_I{}^2\right)} + \sigma_r,$$

(3.1)

Where R_O is the inner radius and R_I is the outer radius of the coating layer. R_O and R_I remain unchanged as the outer layers of the PyC-2 samples experienced no measurable change in radius. From XCT measurements, it can be seen that the load transmitted to the kernel is higher at 1000 °C, therefore the F_k is likely larger (**Figure 3.4B)**. Thus, application to **Eq. 3.1** shows that a higher F_k could allow for the reduction in strength. Residual stresses (σ_r) could also be another factor affecting the failure load. At high temperature, the compressive stress is relaxed, which lowers the load required to crush the particle to the same amount. A reduction in strength of 45% was observed at the high temperature which is significantly larger than the prior reported 30% [84], [85], [88]. This is not unexpected as the measurements taken in literature were performed at RT after the sample had been cooled which undoubtedly relaxed any residual stresses.

Rohbeck et al. [89] used nano-indentation to measure the elastic modulus and nano-hardness of the TRISO particle's SiC layer at RT and 500 °C. Their results show a 40% reduction in hardness and ~11% reduction in elastic modulus. The reduction in nano-hardness at elevated temperatures was claimed to be indicative of a lower yield strength at 1000 °C, but the yield strength of SiC does not reduce significantly at 1000 °C [72]. Rohbeck et al. [83] also examined TRISO particles annealed between 1600 °C and 2000 °C in which the SiC layer had no change in nano-hardness or modulus. This means it is likely that there is no degradation of the SiC at high temperature and instead the PyC-2's observed reduced strength at 1000 °C is most likely due to the relaxation and redistribution of residual stresses. The PyC-1 samples' failure loads were similar between RT and 1000 °C which indicates that the residual stresses in the buffer and PyC layers were less significant. The buffer and PyC layers have very similar thermal expansion coefficients making residual stresses less likely due to fabrication processes. There was still a larger load line axial compression seen in the 1000 °C PyC-1 sample implying that it possessed a higher F_k, but this had no major effect on the final failure load.

The majority of studies done on TRISO particles have used large numbers of samples [83]–[86], [88], and employ a normal distribution or Weibull statistics to calculate the load of failure. This procedure uses post-mortem examination and in the case of low strength outliers it is generally assumed that a flaw accounted for its low performance. The XCT *in situ* scanning performed on the TRISO particles in this study at both RT and 1000 °C make it possible to reduce the number of samples needed to gain a higher-fidelity understanding of the damage evolution and structural integrity of these TRISO particles.

3.5 SUMMARY

Utilizing *in situ* XCT made it possible to examine the real time fracture mechanisms of TRISO nuclear fuel particles at temperature under load. The behavior of the TRISO particles under compression was measured with XCT imaging at RT and 1000 °C to allow for the observation and precise measurement of flaws, cracks, contact area, and dimensional changes.

Two PyC-1 samples were tested, one at RT and one at 1000 °C, and two PyC-2 samples were tested, one at RT and one at 1000 °C. These samples were crushed while being stopped periodically to take XCT scans to fully image the sample. The PyC-1 sample consisted of a kernel, buffer, and PyC. At RT and 1000 °C it fractured when microcracks formed at the loading contact point and extended out from there. The PyC-2 sample consisted of a kernel, buffer, SiC, and PyC, and fractured abruptly with no prior microcrack formation. For both PyC-2 samples tested at RT and 1000 °C, the cracks that formed either just before or after failure were located inside the loading contact point and extended out from there significantly different from the standard Hertzian contact model. The reduction of strength in the PyC-2 sample at high temperature is not due to the degradation of the SiC layer at 1000 °C, and is instead most likely due to the relaxation and redistribution of the residual stresses at elevated temperatures. This methodology used to make real time observations of failure mechanisms can be further utilized to test more complex layered TRISO particles and irradiated particles to gain further insight into the mechanical degradation under crushing loads.

Chapter 4
Refractory *BCC* High Entropy Superalloys

4.1 INTRODUCTION

High entropy alloys (HEAs) have been in the research spotlight ever since their proposed existence in 2004 by Yeh et al [10]. The field has opened up millions of new alloying combinations, created opportunities that have driven the materials engineering research field into overdrive, and led researchers to experimentally synthesize original elemental compositions or use computational methods and machine learning to discover new combinations. With these methods, several HEAs such as the CrCoNi and CrMnFeCoNi alloys have been developed, and have already proven to have excellent mechanical properties [15], [94], [95].

From the HEA field has emerged a push to find a material that can maintain strength and toughness at higher temperatures than Ni-based superalloys, the most widely used material for high temperature applications. Structural materials for high temperature applications have been extensively explored for applications such as gas turbine engines. Ni-based superalloys have many favorable properties at high operational temperatures: high tensile strength, reasonable ductility, good machinability, creep resistance, fatigue endurance, and sufficient oxidation resistance. However, the maximum operating temperature of Ni-based superalloys is limited by the melting temperature of its primary element of nickel, which has a melting temperature of 1455 °C [3], [96]. Body centered cubic (*bcc*) refractory HEAs (RHEAs) are composed of elements like W (3410 ℃), Ta (3020 ℃), Zr (1855 ℃), Nb (2477 ℃), and Mo (2623 ℃) [97] and have the potential to be useful in these high temperature applications because of their ability to retain high strength at high temperatures. Of all the possible *bcc* RHEAs, several studies have come out showing promising results for the compressive strength of NbMoTaW and VNbMoTaW RHSAs over 1000 ℃ which were synthesized, and tested by Senkov et al [95]. However, they are very brittle at room temperature [98], [99]. TaNbHfZrTi, was later tested and shown to have a good ductility at room temperature in compression and tension, but lost significant strength above 800 ℃ [99], [100]. This problem has been difficult to solve: if the alloy has good low temperature performance, it is weak at high temperatures. Conversely, if it shows strength at high temperatures, it is brittle at low temperatures. This creates an operational temperature range that is too small, rendering the alloy inadequate for most applications. Significant effort has been made to improve not only room temperature ductility, but also high temperature strength through new combinations of elements and by controlling microstructure through heat treatments. A possible solution to this problem is the use of refractory high entropy superalloys (RHSA's). These RHSA's have a complex precipitate dual phase microstructure similar to the dual phase Ni-superalloys microstructure.

The microstructure that gives Ni-based superalloys its peak performance is the presence of two phases: a ductile matrix phase and a harder coherent precipitate phase. This combination allows for its sound high temperature performance. $AlMo_{0.5}NbTa_{0.5}TiZr$ RHSA when slow-cooled from 1400 ℃, has a basket-weave microstructure that consists of disordered *bcc* nano-precipitates (A2) and an ordered *bcc* matrix (B2). This alloy exhibits superior mechanical properties with a compressive strength of 2197 MPa at RT and 725 MPa at 1000 ℃ [101].

However, this alloy shows very limited ductility because the B2 matrix phase is the hard brittle phase while the A2 nano precipitate is the ductile phase. This is the inversion from Ni superalloys, where the precipitates are hard and the matrix is ductile. Through heat treatments, Soni et al. was able to invert the matrix and precipitates of another RHSA, $Al_{0.5}NbTa_{0.8}Ti_{1.5}V_{0.2}Zr$, such that it imitated the microstructure of Ni superalloys; with soft matrix and hard precipitates [102]. This resulted in a decrease in compressive yield strength (1065 MPa), but significant increase in the ductility (elongation 38%) at RT while uninverted $Al_{0.5}NbTa_{0.8}Ti_{1.5}V_{0.2}Zr$ has a very high compressive yield strength of 2032 MPa, but little plasticity [102]. These tests were performed in compression, and it is important for materials with this potential for engineering applications to have their tensile and fracture toughness properties examined. In real-life engineering applications, load-bearing structural materials are often subject to tensile loading conditions, making the tensile properties far more critical for integrity of components and structures. Only limited tensile properties have been reported for RHEAs.

In high temperature materials with brittle characteristics, such as refractory metals, ceramics, and metal-ceramic composites, fracture toughness is one of the major properties to evaluate to determine a materials use as structural parts. For example, Nb-Hf-Ti-Si [103], [104], Mo-Si-B alloys [105]–[107], and ceramic-matrix composites [108], [109] all have higher strength at elevated temperatures than Ni-superalloys yet they have a low fracture toughness making them unsuitable for many safety-critical structural applications.

The RHSAs discussed here are *bcc* dual phase alloys that have nano precipitates very similar to the crystal structure of Ni superalloys. These have been chosen both for their microstructure, as well as their high melting temperature, which exceeds that of Ni by at least 1000°C. Here we examine the mechanical properties of two different microstructures of the $Ti_{20}Zr_{20}Nb_{25}Ta_{25}Al_{10}$ (atom percent) alloy. This alloy is similar to $Al_{0.5}NbTa_{0.8}Ti_{1.5}V_{0.2}Zr$ as it can also form two different microstructures that are synthesized by different heat treating conditions. The first microstructure of $Ti_{20}Zr_{20}Nb_{25}Ta_{25}Al_{10}$ is a brittle matrix and soft precipitates (600HT), and the second is the inverse phase material with a ductile matrix and hard brittle precipitates (the 800HT condition). They were tested in compression, tension, and for fracture toughness measurement at room temperature (RT), 800 ℃, 1000 ℃, and 1200 ℃. I performed all of the sample preparation for these materials including the surface polishing, notching, and micronotching. I made the inert gas tube fixturing required to keep the samples from oxidizing when testing up to 1200 °C, in a furnace that was not designed for inert gas. I performed all the tensile and fracture toughness tests at all temperatures. I examined the fracture surfaces of the tensile and fracture toughness specimens, and contributed to theorizing the failure mechanisms.

4.2 PROCESSING AND MICROSTRUCTURE

4.2.1 Processing

The $Ti_{20}Zr_{20}Nb_{25}Ta_{25}Al_{10}$ was manufactured at Seoul National University, Seoul, South Korea by vacuum arc melting the high purity elements: Ti, Zr, Nb, Ta, and Al. The ingots were vacuum arc melted five times to ensure a homogeneous composition. Then through the heat treatment process illustrated in **Figure 4.1** the ingots were hot isostatic pressed at 1500 °C for 2 hours and then cooled under vacuum. They were homogenized by holding them at 1300 °C for

12 hours with a constant flow of argon. The ingots were then electrical discharge machined (EDM) into 3mm plates that were heat treated at 800 ℃ for 12 hours and then EDMed into dog-bone tensile specimens, compression specimens, and C(T) fracture toughness specimens. These samples are labeled as the 800HT condition specimens. Half of these specimens were re-homogenized at 1300 °C for 12 hours and then heat aged at 600°C for 24 hours and air cooled to create the 600HT condition material with a brittle matrix and ductile precipitates.

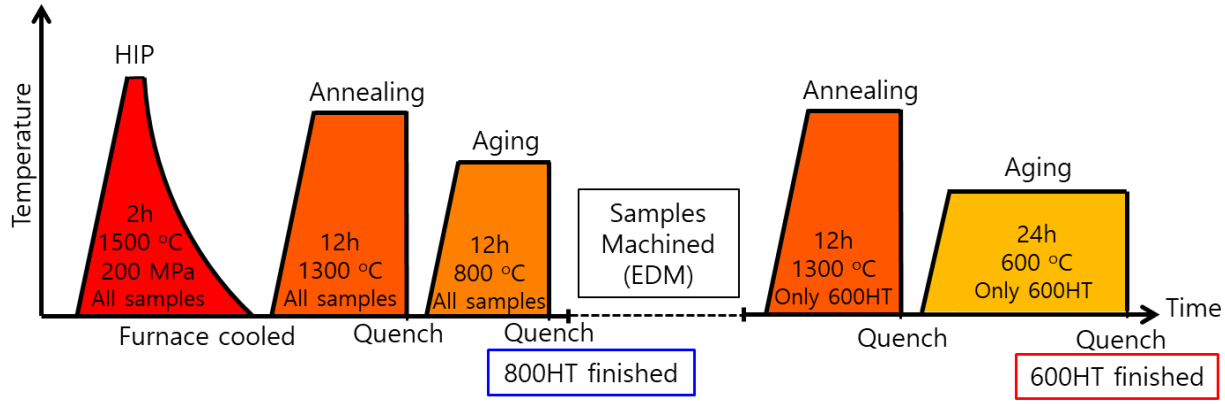

Figure 4.1: A schematic of the processing steps to form the 600HT condition and the 800HT condition.

4.2.2 Microstructure Characterization

Microstructural characterizations were performed on a scanning electron microscope (SEM; TESCAN MIRA 3). Electron backscatter diffraction (EBSD; e Flash FS, Bruker) was used to analyze the phase constitution, grain size, and orientation.

An FEI Tecnai G2 Spirit TWIN TEM instrument and a JEOL JEM-2010F HRTEM instrument were employed for micro and nanoscale fine structure characterizations. Thin-foil tunneling electron microscopy (TEM) specimens were prepared from RHSA pieces before and after deformation by dry mechanical grinding and then ion milling.

Post processing, images were taken of the two heat treatments microstructures shown in **Figure 4.2. Figure 4.2A** is a TEM image of the 600HT condition microstructure, where the light precipitates are distributed in the dark brittle matrix. **Figure 4.2B** is a SEM back-scattered electron (BSE) image of the 800HT condition microstructure; the dark precipitates are distributed in the continuous light phase. The Ta-rich A2 phase of RHSA is observed as a bright phase in BSE-SEM images due to the high atomic number of Ta in the Ti-Zr-Ta system [110]. Therefore, the bright matrix phase in **Figure 4.2B** is considered as A2 phase (ductile). Some abnormal growth of the dark precipitate can be observed in the 800HT condition microstructure. **Figure 4.2E** shows a dark field image of the alloy in [001] zone axis and it is seen that the ordered *bcc* phase constitutes the continuous channels of basket-weave structure of RHSA. There have been reports that the basket-weave structure of RHSA consists of continuous channels of an ordered *bcc* phase (B2 brittle) as matrix and disordered *bcc* (A2 ductile) phase as precipitates [101], [102], [111], which is consistent with the present study.

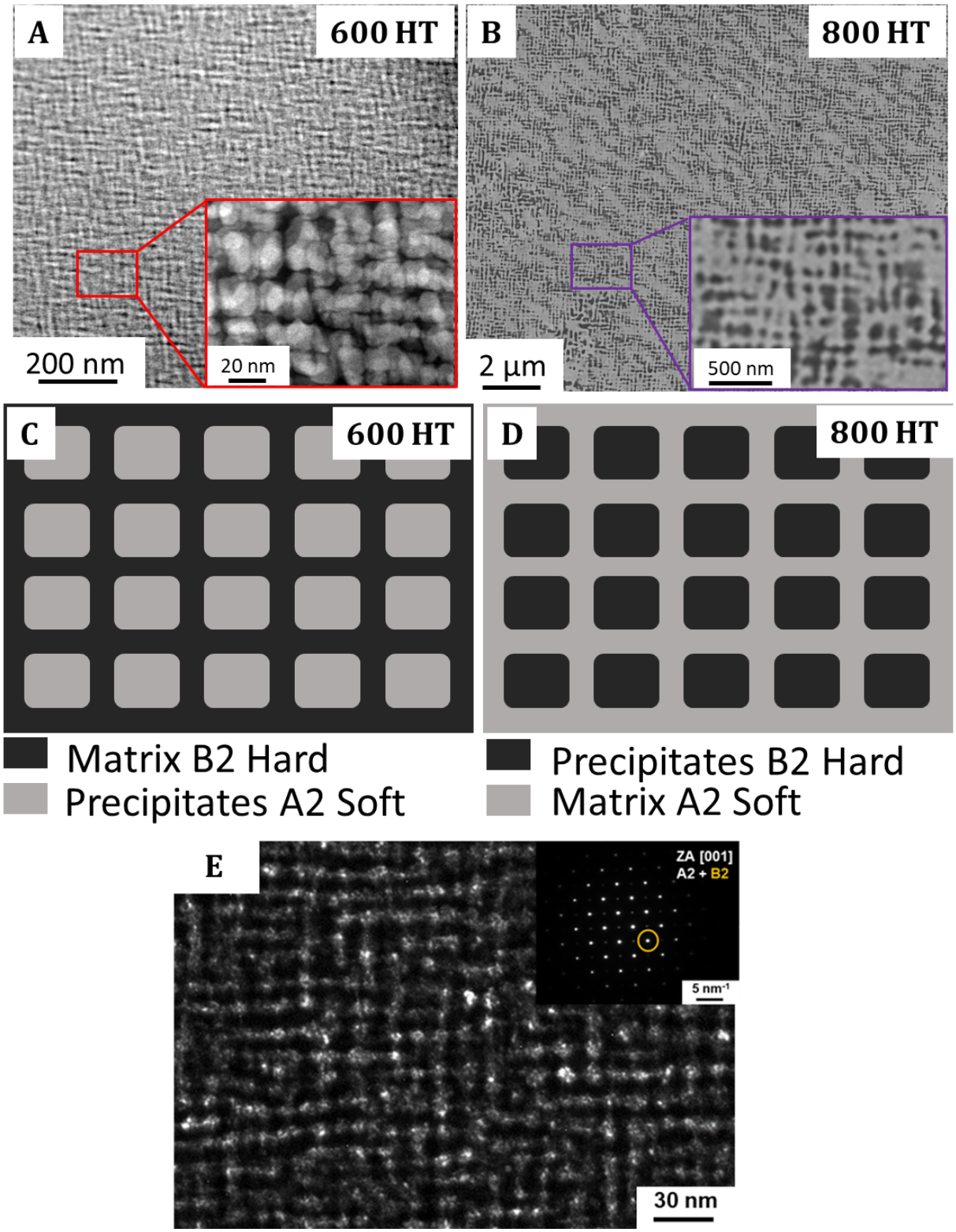

Figure 4.2: (**A**) TEM image of the microstructure of the 600HT condition. (**B**) SEM BSE images of the microstructure of the 800HT condition . (**C**) and **(D)** are illustrations of the microstructures of the two different heat treatments done at 600 ℃ and 800 ℃ respectively. (**E**) TEM dark field image of the alloy in [001] zone axis.

4.3 MECHANICAL TESTING

To gain a broad spectrum analysis of the mechanical properties and difference between the 600HT condition and the 800HT condition samples, they were tested for compression, tensile, and fracture toughness properties. **Figure 4.3** shows the sample geometries tested for compression tension and fracture toughness. The majority of the literature focuses on compression as it it's the easiest to perform at high temperature and is the material property that is most likely to yield inflated results. However, testing these materials' tensile and fracture toughness properties is critical for determining if these materials have any engineering applications.

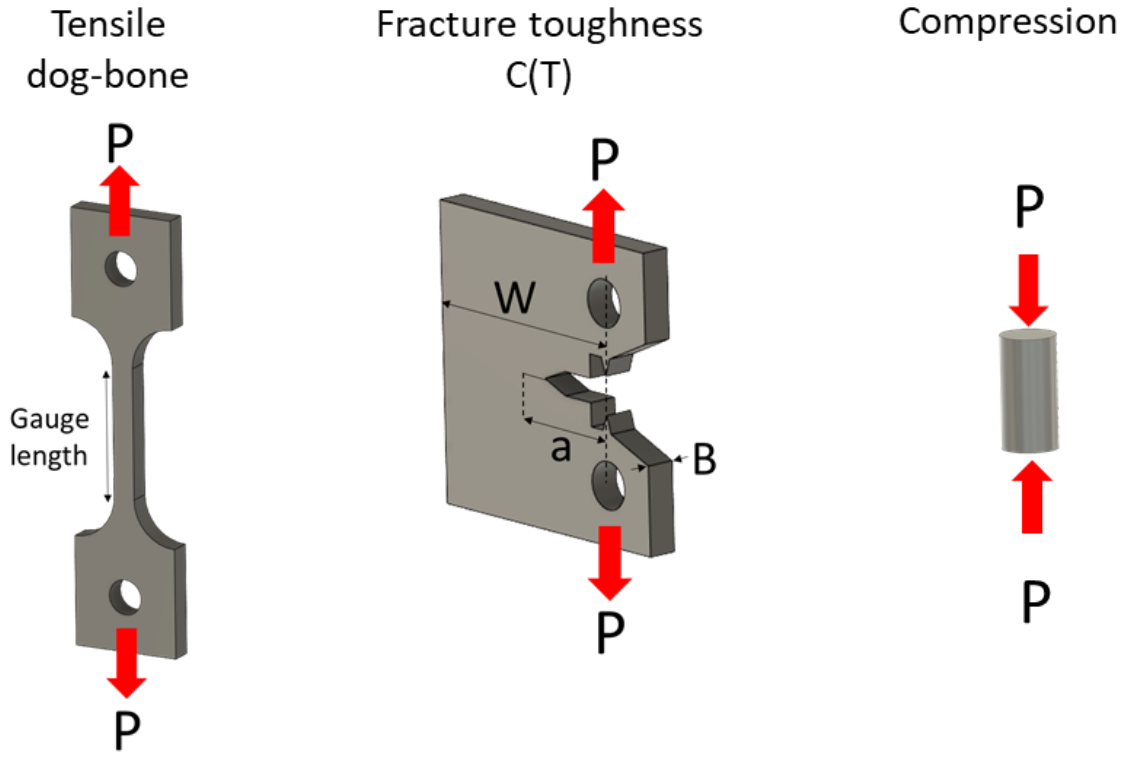

Figure 4.3: Computer aided design file images of the tensile (dog-bone), the fracture toughness (compact tension), and compression specimens that were used to test the materials mechanical properties.

All mechanical tests were performed on (MTS 810 servo-hydraulic load frame with an Instron 8800 controller) testing machine. These tests were performed at RT, 800 ℃, 1000 ℃, and 1200 ℃. Samples were loaded in position control at a very low rate of 0.1 mm/min to account for the brittle nature of the materials.

4.3.1 High Temperature Setup

The tension, compression, and fracture toughness samples tested at high temperatures utilized a MTS 657.01 high temperature resistance furnace. Due to the alloy's propensity to oxidize, a tube was inserted into the center of the furnace that was flooded with a constant flow of argon gas to reduce the oxidation of the sample during heating, testing, and cooling. **Figure**

4.4 illustrates the inert gas tube setup utilized in the testing of the tensile tests. A similar setup was used for fracture toughness and compression testing. Two K-type thermocouples were spot welded directly to the top and bottom of each tensile sample just outside the gauge length to accurately measure the temperature of the sample and make sure heating was uniform. Two thermocouples were attached to the top and bottom of the fracture toughness samples, and the compression sample only used one thermocouple due to its smaller size.

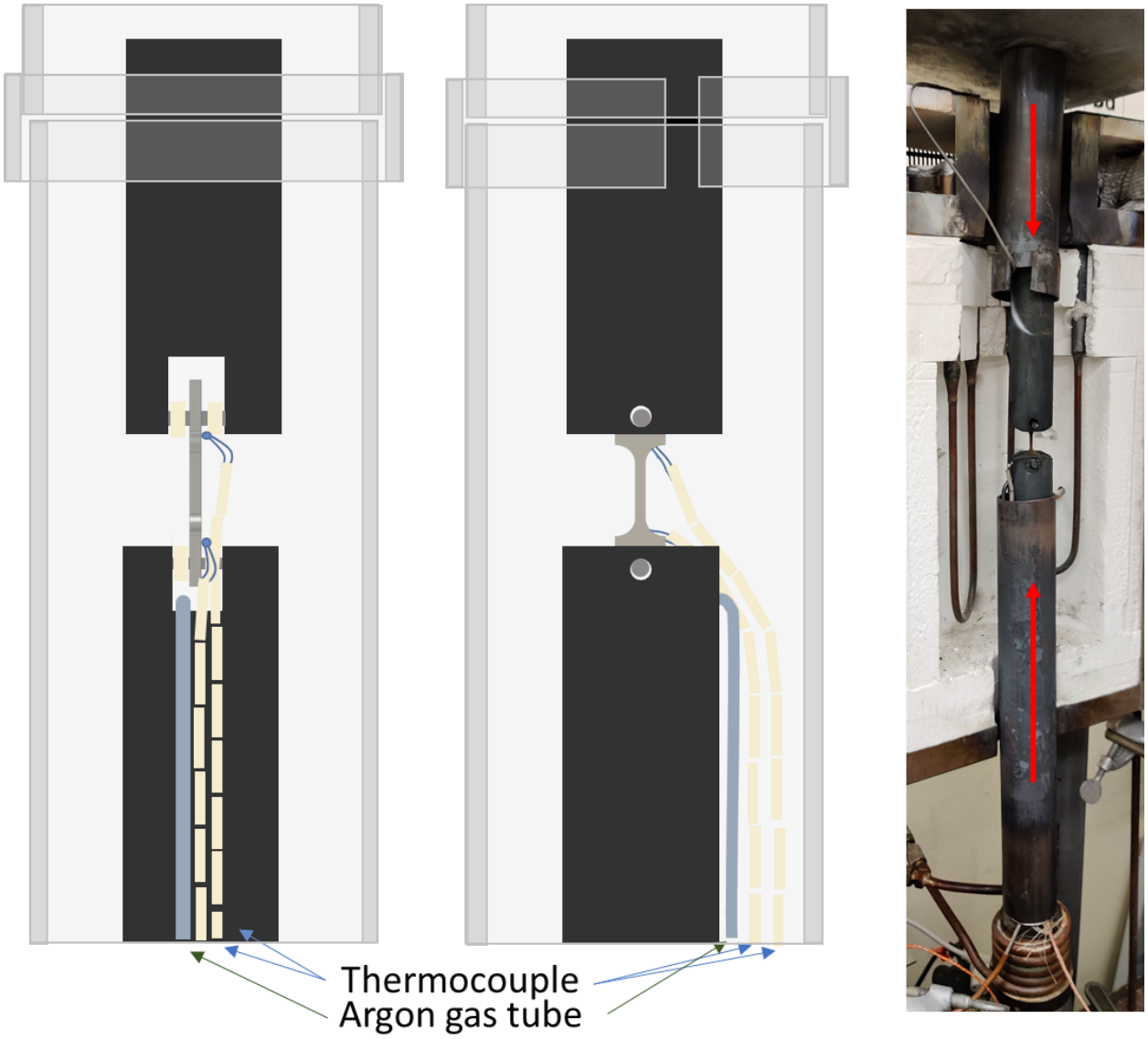

Figure 4.4: Image of the high temperature inert gas setup used. This allows for inert gas to constantly purge the chamber containing the specimen to eliminate or greatly reduce oxidation. The center image is a 90 degree counterclockwise (looking from the top) rotation of the left illustration. The right image is the tube opened up for sample loading and unloading.

4.3.2 Micro Notching

Due to the highly brittle nature of the materials the fracture toughness samples were not precracked and instead were micronotched to form a sharp crack tip. The samples were notched

using a low-speed diamond saw to increase the length of the a/W to nearly 0.5, and then sharpened using a micro-notching technique. Micronotching uses a thin razor blade to create a very sharp notch in a material. It achieves this by sliding the sample back and forth on a razor blade covered in 5µm diamond polishing paste, which polishes in a notch into the sample. **Figure 4.5** shows the micronotcher utilized. The final notch root radii of all fracture toughness samples tested was under 40 µm.

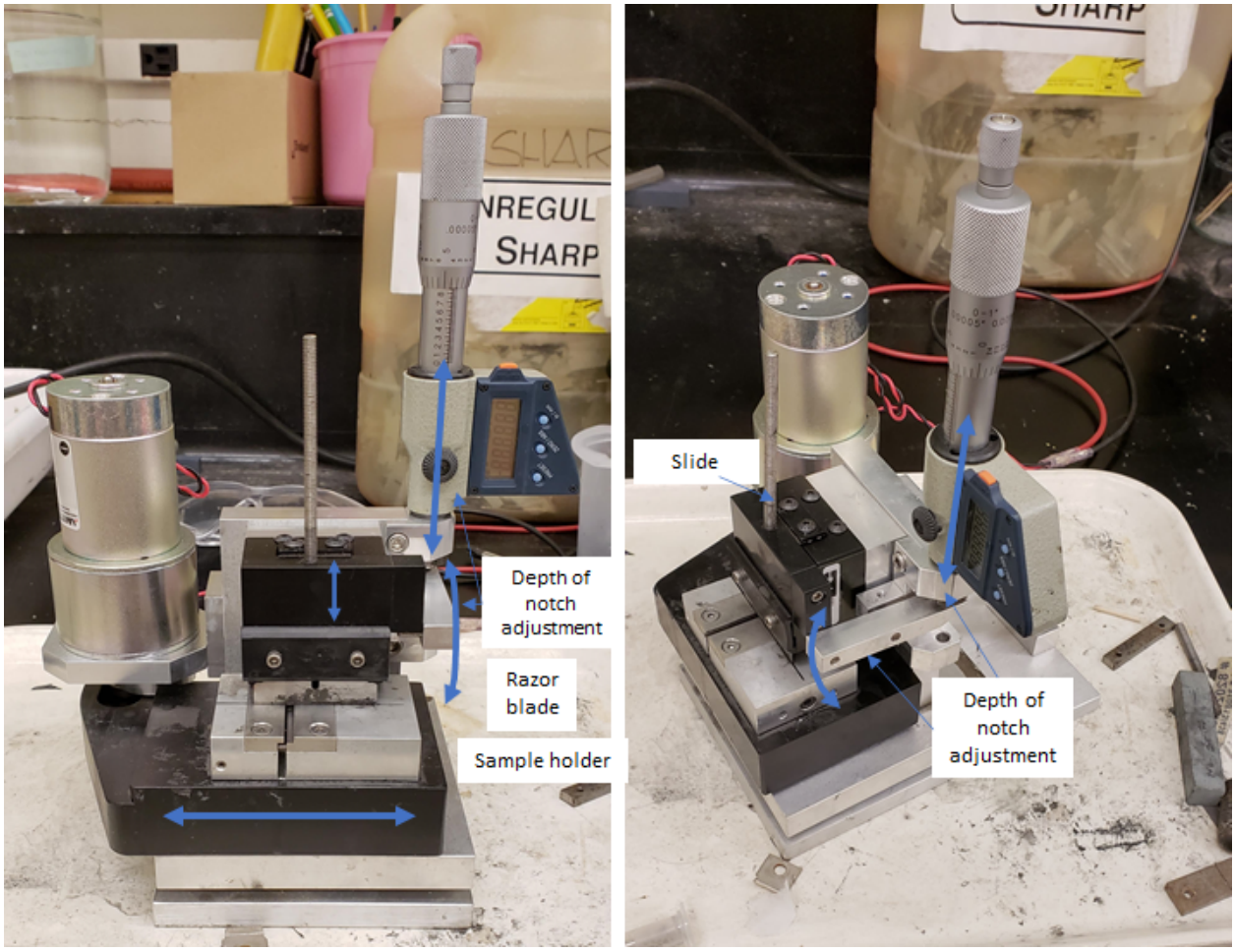

Figure 4.5: Image of the micronotcher. The sample is loaded into the sample holder in the center of the material, this slides back and forth moving the sample across the razor blade creating a sharp notch in the sample.

4.4 MECHANICAL PROPERTIES

4.4.1 Compression Tests

The RHSA compression samples were cylindrical and had a diameter of 4 mm and a length of 8 mm. They were deformed with SiC platens. The 600HT condition and the 800HT condition were tested at RT, 800 ℃, 1000 ℃, and 1200 ℃. The compression tests were carried out in position control with a rate of 0.1mm/min, which is a strain rate of 10^{-3} s^{-1}. If the samples did not fail during compression testing they were stopped at 40% reduction in length.

Figure 4.6A and **B** show the compression stress-strain curves of the 800HT condition and the 600HT condition samples. The 800HT condition shows ductility at all tested temperatures, and the 600HT condition shows significant ductility at all but room temperature. The 600HT condition sample has a high strength, but no notable plasticity at RT. The sample fractured at ~6% strain, but this number is inflated as the displacement was measured by load line. The 800HT condition sample had a slightly lower ultimate strength but experienced ductility with a strain of failure of ~18%. Both the 600HT condition and the the 800HT condition behaved similarly in terms of load and ductility at 800 ℃, 1000 ℃, and 1200 ℃. At 800 °C and 1000 °C, the stress-strain curves exhibited softening behavior where after the flow stress reaches a peak, it then decreases during the further strain. At 1200 °C, the slope of the steady-state flow stage after the yield point was observed until the test was stopped at 40 % strain.

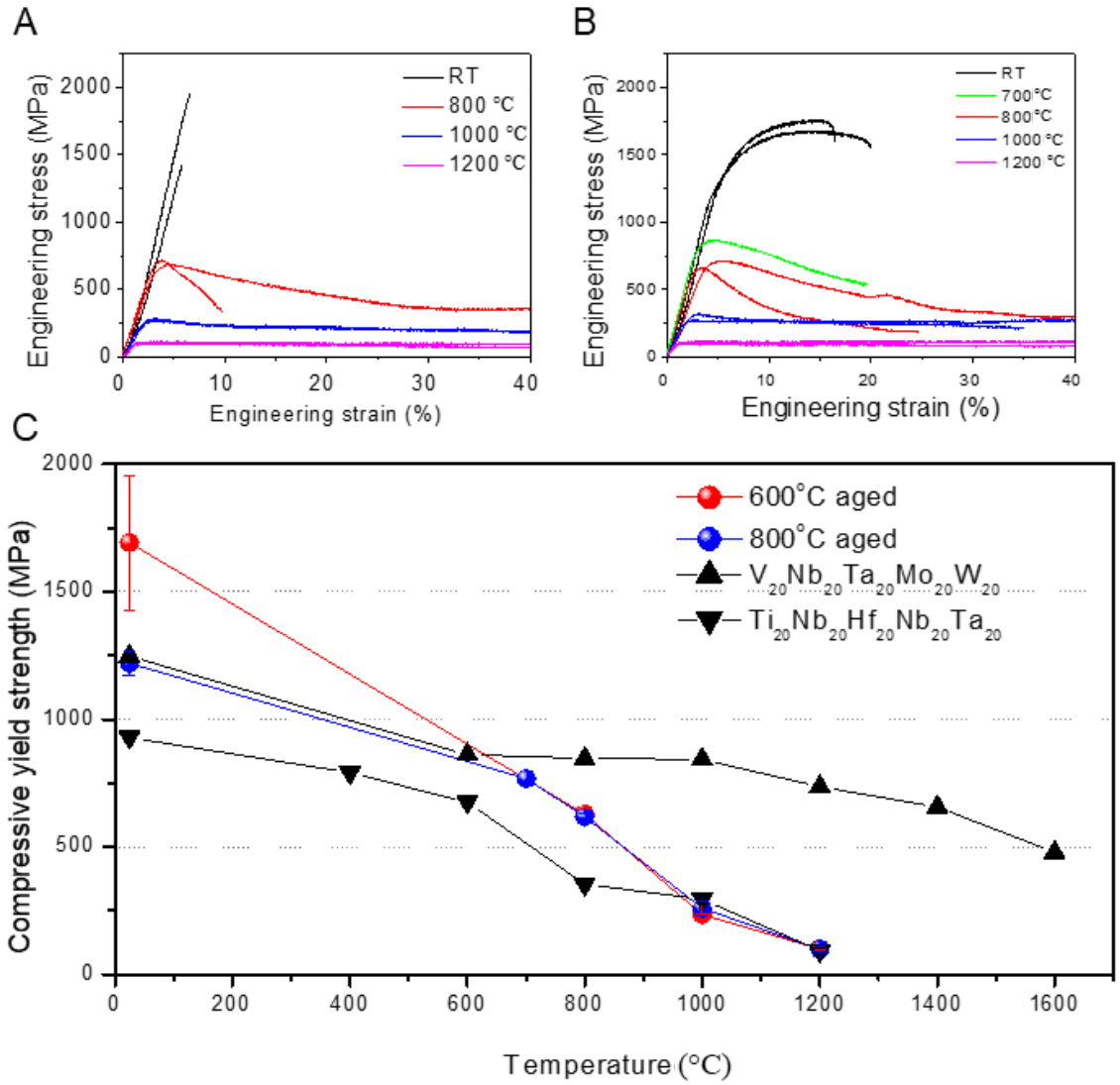

Figure 4.6: Compression stress-strain curve of the 600HT condition (**A**) and the 800HT condition (**B**) tested at RT, 800 ℃, 1000 ℃, and 1200 ℃. (**C**) is the tensile strength vs temperature of the 600HT condition and the 800HT condition.

This decrease in stress and steady flow state after yielding has been observed in materials that have two phases at low temperatures. For a near-α titanium alloy, the flow stress of the high temperature compression decreases after yielding at the α+β two phase temperature region, while steady-state stress flow after a yield point is observed at the single β phase temperature region [111], [112]. This same behavior of flow stress is also observed in the high temperature compression tests of the Ni-based superalloys which have γ + γ′ two phase region at low temperatures [113]. By annealing the $Ti_{20}Zr_{20}Nb_{25}Ta_{25}Al_{10}$ alloy at 1000 °C and 1200 °C and examining the microstructure (**Figure 4.7**) it was determined that the B2 phase dissolves into the alloy, creating a single phase A2 material between 1000 °C and 1200 °C, which explains the compression behavior.

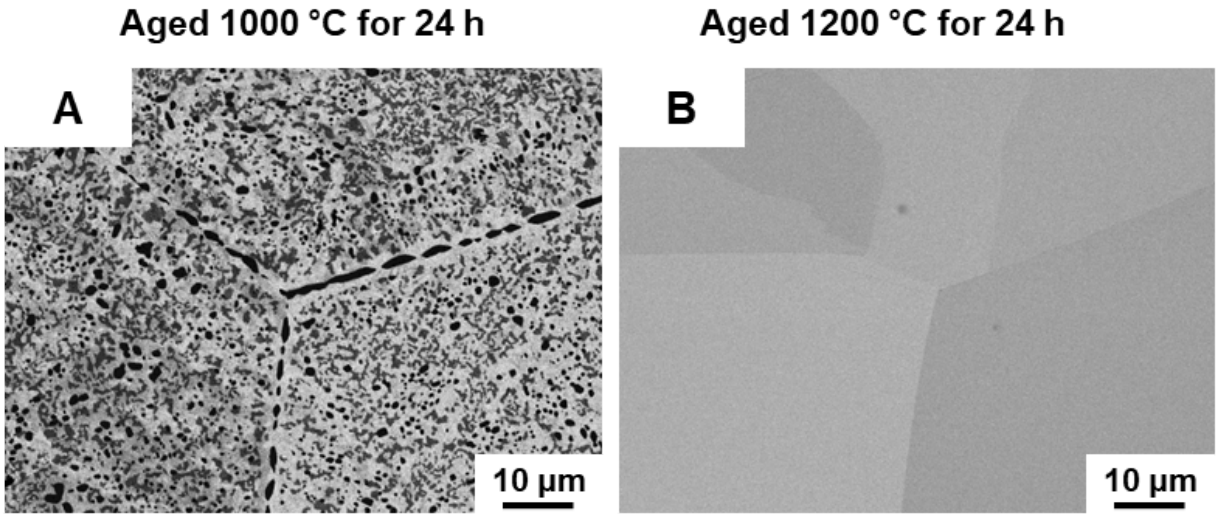

Figure 4.7: SEM back-scattered image of $Ti_{20}Zr_{20}Nb_{25}Ta_{25}Al_{10}$ RHSA (**A**) aged at 1000 °C for 24 h and (**B**) aged at 1200 °C for 24 h.

4.4.2 Tensile Tests

The 600HT condition and the 800HT condition dog-bone specimens had a thickness of 3 mm, a width of 2 mm, and a gauge length of 10 mm. Examining the tensile stress-strain properties shown in **Figure 4.8**, it is clear that both heat treatments of the RHSA exhibited no significant tensile ductility at any temperature. The samples broke (nominally) elastically in the range of 0.1%-0.2% strain and showed no yielding. Both of these alloys fractured low loads of ~180 MPa for the 800HT condition condition and ~110 for the 600HT condition at RT. This is unexpected as when tested in compression both heat treatments showed significant ductility at all temperatures, with the exception of the 600HT condition at RT. It can also be seen that there is a significant drop in strength as the temperature increases for both the 600HT condition and the 800HT condition, and both end up fracturing at about the same value of ~25 MPa at 1200 ℃. Given the compressive strength seen in **Figure 4.6**, the yield stress should be much higher than observed in **Figure 4.8**. The 800HT condition shows higher tensile strength than the 600HT condition at all tested temperatures. The 800HT condition has a higher load at fracture stress than the 600HT condition. Meaning the 800HT condition is likely slightly more ductile than the 600HT condition samples. Brittle materials become flaw-dependent, meaning the flaw size and

shape will affect at what load the sample will fracture. More ductile materials are less flaw dependent. Because the the 800HT condition and the 600HT condition were made from the same ingot their flaws should be similar in all samples.

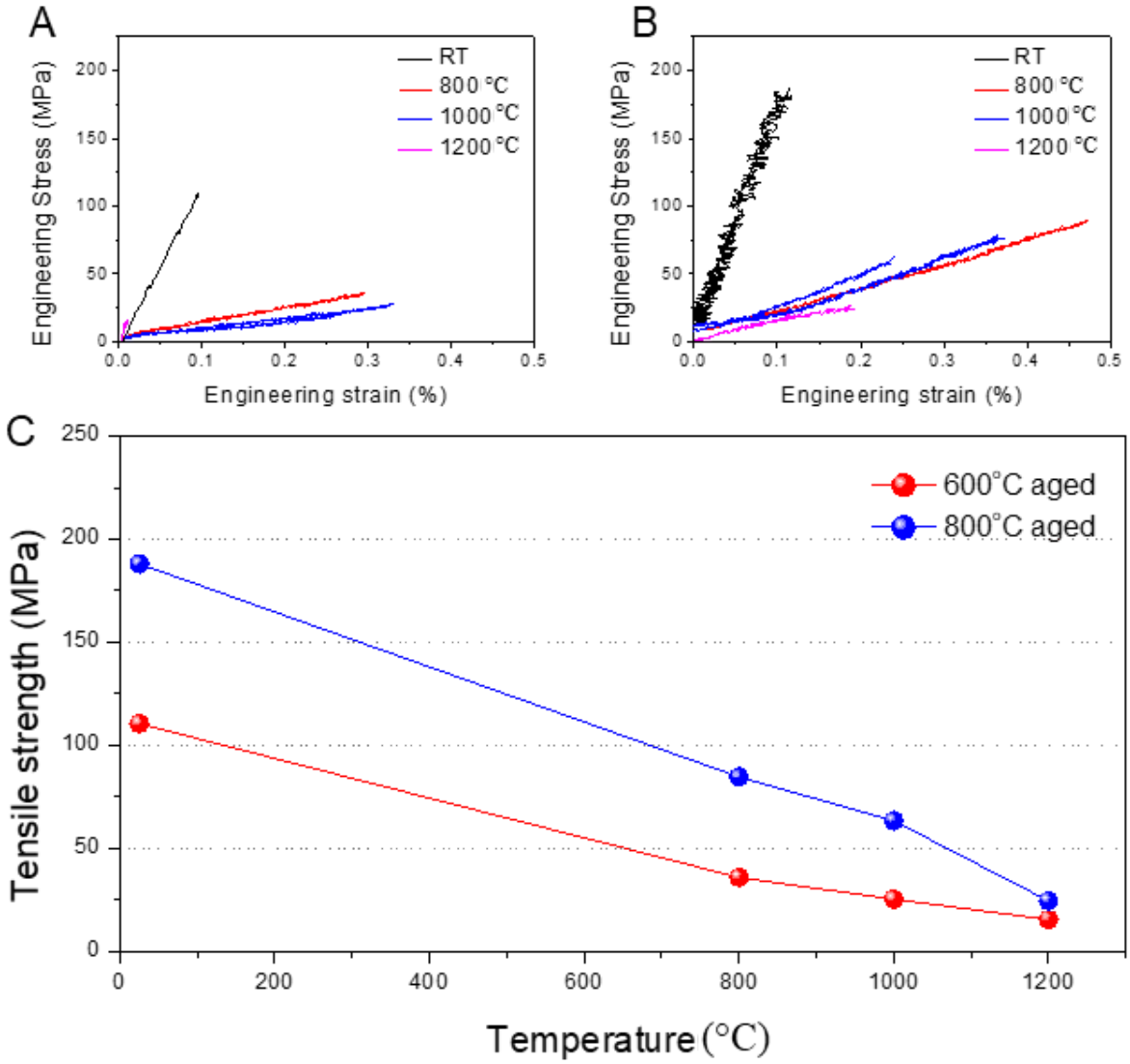

Figure 4.8: Tensile stress-strain curve of the 600HT condition (**A**) and the 800HT condition (**B**) tested at RT, 800 ℃, 1000 ℃, and 1200 ℃. (**C**) is the tensile strength vs temperature of the 600HT condition and the 800HT condition.

The RT samples did not require the use of an inert atmosphere so they were tested with an extensometer. This is where the large discrepancy in the slopes of the RT lines come from in **Figure 4.8A** and **4.8B**. The slopes of the high temperature test should be very close to that of the room temperature tests, similar to the slope difference seen in the compression tests. Testing without an extensometer is never ideal, but if the material shows no ductility, the extensometer is not as important because there is no plastic deformation to measure. However, the elastic modulus will not be accurate.

4.4.3 Fracture Toughness Testing

While neither RHSA heat treatment showed tensile ductility, it is still important to examine the fracture toughness properties of the materials. The C(T) specimens were electrical discharge machined (EDM) and heat treated along with the 600HT condition and the 800HT condition tensile specimens. They were tested at RT, 800 °C, 1000 °C, and 1200 °C. The fracture toughness testing was carried out in accordance with ASTM Standard E1820 [32]. **Figure 4.9A** and **B** show the load displacement curves. They show that the C(T) specimens exhibited no ductility during fracture tests. At crack initiation the crack extended across the sample breaking it completely and leaving it in two halves. The changes in fracture toughness due to temperature effects are seen in **Figure 4.9C**. At RT the 800HT condition showed a fracture toughness of 14.4 MPa√m and the 600HT condition showed a fracture toughness of 3.08 MPa√m. At elevated temperatures the fracture toughness of these materials significantly decreased and neither sample exceeded 5 MPa√m.

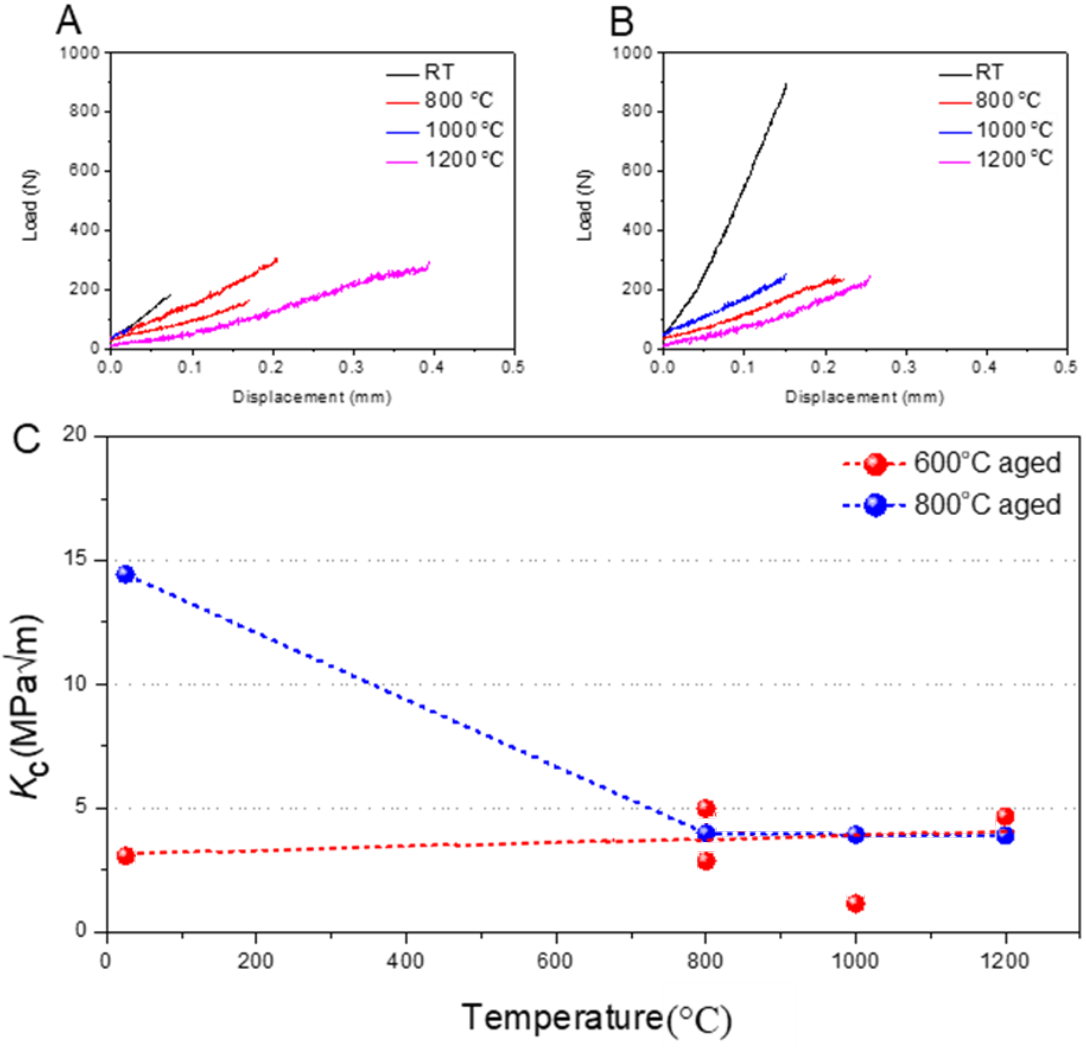

Figure 4.9: Load vs displacement curves of the 600HT condition (**A**) and the 800HT condition (**B**) tested at RT, 800 ℃, 1000 ℃, and 1200 ℃. (**C**) Fracture toughness vs temperature of the 600HT condition and the 800HT condition.

4.5 CHARACTERIZATION OF FAILURE

Based on the materials microstructures, the 600HT condition samples should be brittle and the 800HT condition ductile, but this was not what was observed. In tension both the 600HT condition and the the 800HT condition exhibited no ductility, and fractured at a low stress value at all temperatures tested. They also showed a low fracture toughness. However, in compression except for the 600HT condition at RT these materials exhibited significant ductility.

4.5.1 Compression

Electron backscatter diffraction (EBSD) was used to analyze further high temperature deformation behavior. **Figure 4.10** are EBSD inverse pole figure (IPF) maps and a Kernal average misorientation (KAM) map of the 600HT condition compressed at 1000 °C and 1200 °C in which the A2+B2 two phase regions and A2 single phase regions are present, respectively. **Figure 4.10A**, **B**, and **C** are IPF maps of the 600HT condition compressed at 1000 °C. The compressive deformation at 1000 °C is not locally concentrated around the grain boundary, but rather uniformly distributed in the entire grain. Also, dynamic recrystallization (DRX) was observed not only in grain boundaries (**Figure 4.10B**) but also grain interior (**Figure 4.10C**). **Figure 4.10D** is an IPF maps of the 600HT condition compressed at 1200 °C at low magnification, and **Figure 4.10E** is KAM map of the same position as **Figure 4.10D**. During the heating and compression, the B2+A2 two-phase microstructure was solutionized into the A2 single phase and deformed. The KAM value of grain boundary regions is much higher than that in the grain interior, which implies that the strain is concentrated in the grain boundaries and resembles a necklace. Recrystallized grains along grain boundaries are observed in **Figure 4.10D** and **F**. This is a typical necklace structure of discontinuous dynamic recrystallization (DDRX) where deformation strain and DRX are locally concentrated at the grain boundaries. The necklace structures were reported in other RHEAs with single *bcc* (A2) phases that underwent deformations at high temperatures, such as HfNbTaTiZr [114], MoNbHfZrTi [115].

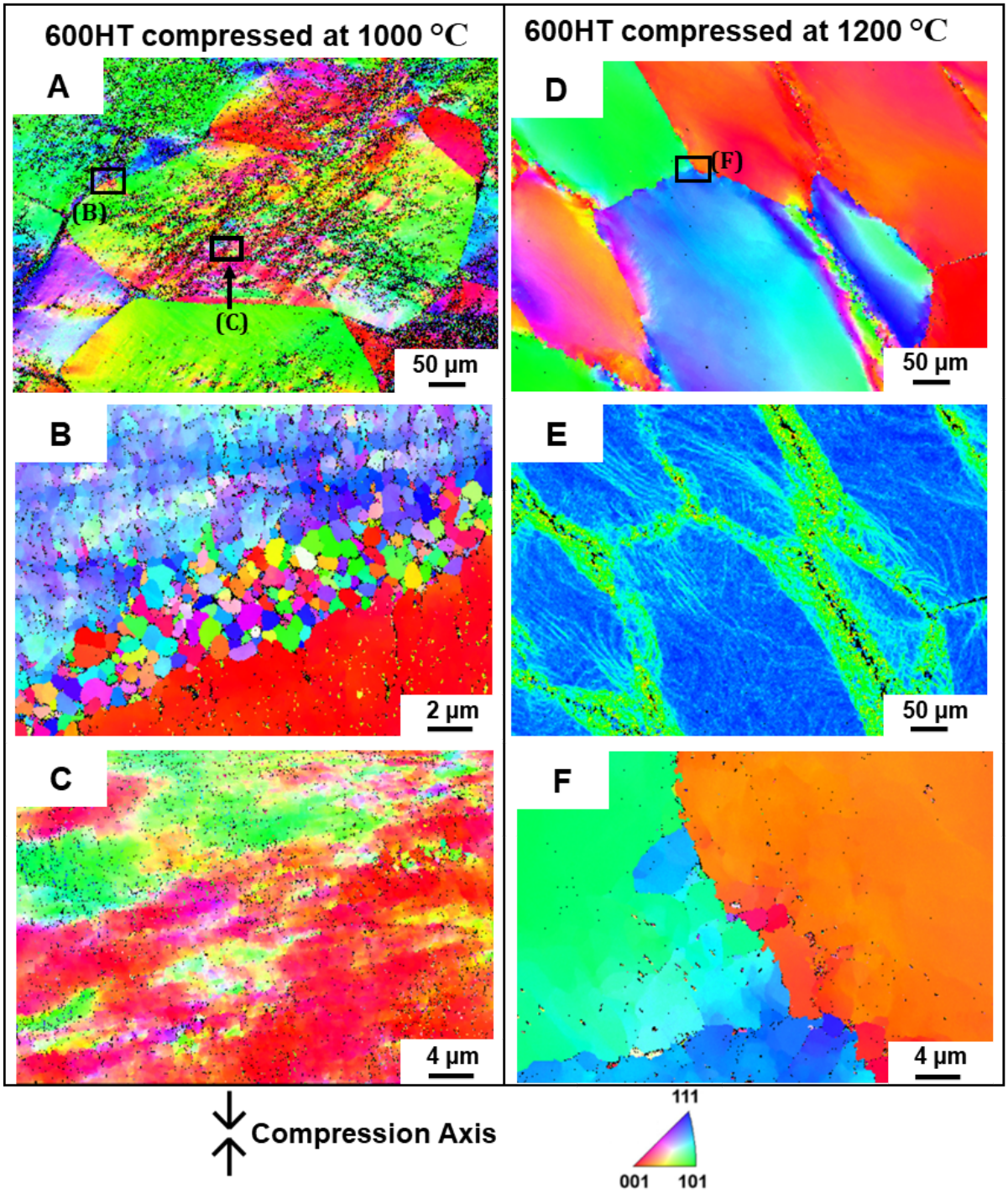

Figure 4.10: (**A**) EBSD inverse pole figure (IPF) map of the 600HT condition compressed at 1000 °C in a low magnification, (**B**) in a high magnification near grain boundary and (**C**) in a high magnification inside grain. (**D**) EBSD IPF maps RHSA aged at the 600HT condition compressed at 1200 °C in a low EBSD IPF map in a high magnification near grain boundary. (**E**) KAM map of the same position as **D**. (**F**) EBSD of recrystallized grains along grain boundaries are observed.

Figure 4.11 is BSE images of the 600HT condition after compressed at 800 °C, 1000 °C, and 1200 °C, respectively. Microstructure changes are observed in the samples tested at the 800

°C, and 1000 °C in which the A2 and B2 phase grew in a direction close to 45 ° to the compression direction and parallel to the shear direction. This is very similar with the rafting phenomena observed in Ni or Co superalloy systems [116]–[119]. For the samples tested at the 1200 °C, the microstructure of the alloy seems very similar to the original basket-weave structure (**Figure 4.1A**). However, it is likely that the basket-weave microstructure was reformed during the cooling of the furnace after testing at 1200 °C. At 1200 °C, the B2+A2 two-phase microstructure is solutionized into a single A2 phase. This single A2 phase was deformed during the test, then the basket-weave structure was reformed in the RHSA as the furnace and sample cooled. There are reports that RHSAs with basket-weave structures can be formed when slow cooling (10 - 20 K/m) after annealing [101], [120], [121].

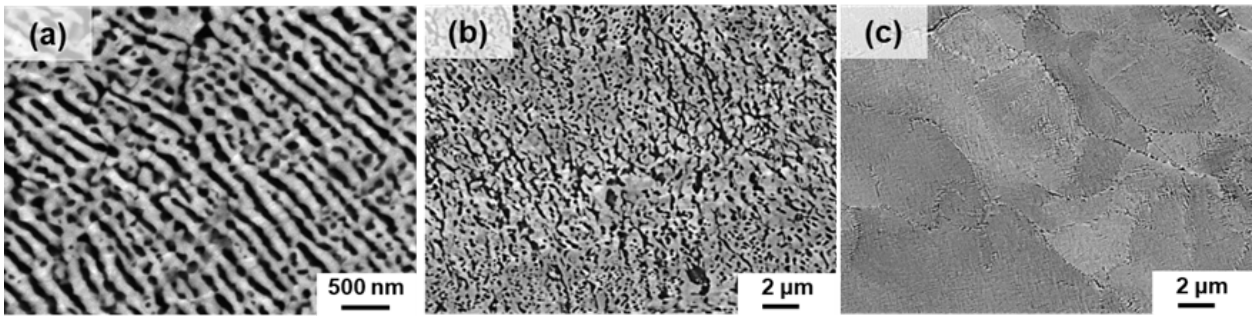

Figure 4.11: BSE images of the 600HT condition after compression at 800 °C (**A**), 1000 °C (**B**), and 1200 °C (**C**). Microstructure changes are observed in the samples tested at the 800 °C, and 1000 °C in which the A2 and B2 phase grew in a direction close to 45° to the compression direction and parallel to the shear direction. The 1200 °C microstructure of the alloy appears similar to the original basket-weave structure.

4.5.2 Tensile and Fracture Toughness

Given the high compressive strength, it was expected that the tensile yield strength would be much higher than what was seen. The two RHSA alloys both failed before yielding under the tensile loads. This could be because their ductile-brittle transition temperature is higher than the 1200 °C that they were tested at, but there was significant grain yielding seen in **Figure 4.10**. This could mean that instead of a high ductile to brittle transition, there was an interjection due to a low grain boundary cohesion strength, causing fracture before the material yielded.

Figure 4.12 shows SEM fractography taken from the fracture surface of the tensile specimens tested at all temperatures. All fractures that take place at all temperatures are inter-granular. **Figure 4.13** is EBSD scans of the crack path of the fracture toughness specimens tested at all temperatures. The notch tip of compact tension samples are indicated by red arrows. Same as the tensile samples all the fracture toughness samples failed intergranularly at all temperatures. Fractography of tensile and compact tension samples clearly show that these samples failed at the grain boundaries, which is consistent with the poor tensile strength and fracture toughness. The grain boundaries cannot take a high enough stress to allow for grain deformation in tensile loading.

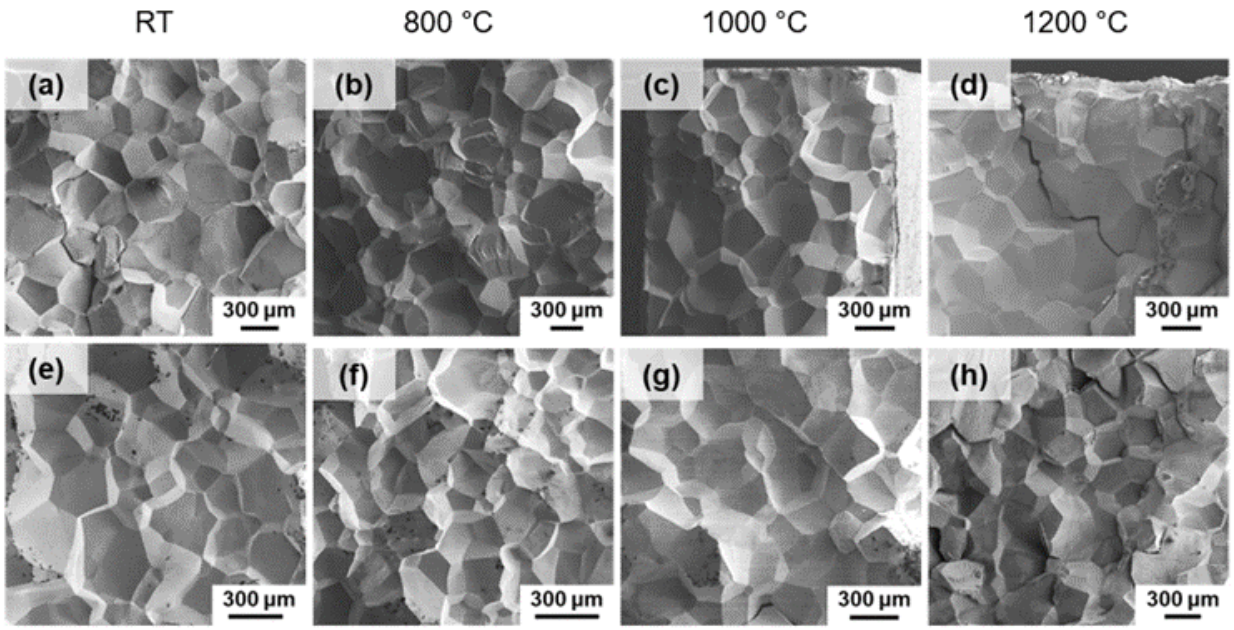

Figure 4.12: SEM images of the fracture surface of the material tested at RT, 800 ℃, 1000 ℃ and 1200 ℃. **A-D** is the 600HT condition and **E-H** is the 800HT condition**.**

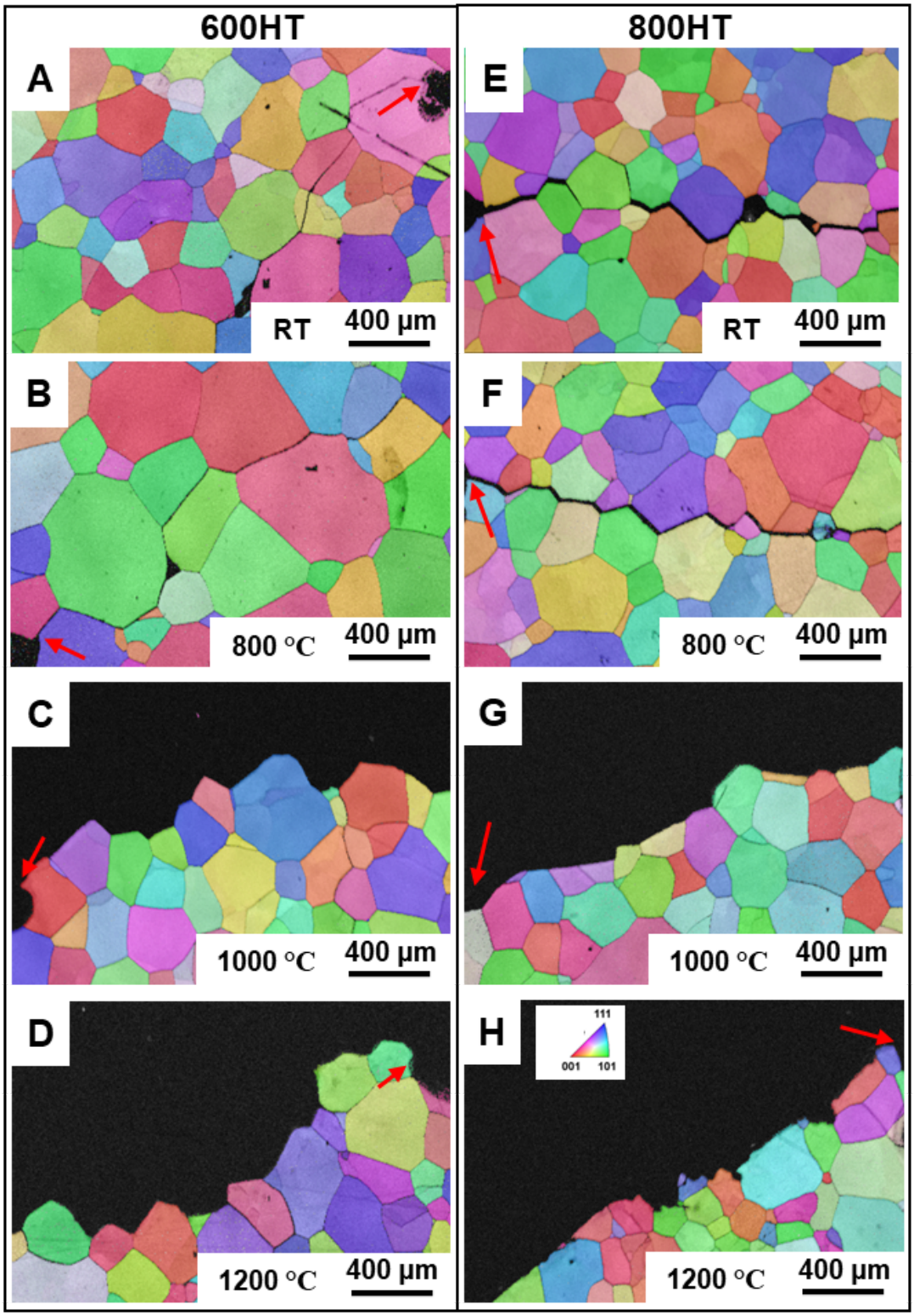

Figure 4.13: EBSD inverse pole figure (IPF) map of crack propagation of the 600HT condition tested at (**A**) room temperature, (**B**) 800 °C, (**C**) 1000 °C, (**D**) 1200 °C. EBSD inverse pole figure (IPF) map of crack propagation of the 800HT condition tested at (**E**) room temperature, (**F**) 800 °C, (**G**) 1000 °C, (**H**) 1200 °C.

4.5.3 Grain Boundary Characterization

Figure 4.14 displays the tensile specimen of the 600HT condition tested at 1000 °C. There is A2 phase (bright contrast) denuded zone at grain boundaries and intergranular cracks result from shearing and cracking in the A2 phase denuded zone. The grain boundary consists of a soft phase with a small amount of hard B2 phase, while the grain interiors have a large amount of B2 phase a few tens of nm in diameter homogeneously distributed throughout. Therefore, the grain boundaries have a lower strength than the interior of the grains, and the deformation is preferentially localized at the grain boundaries, which is the cause of intergranular fracture.

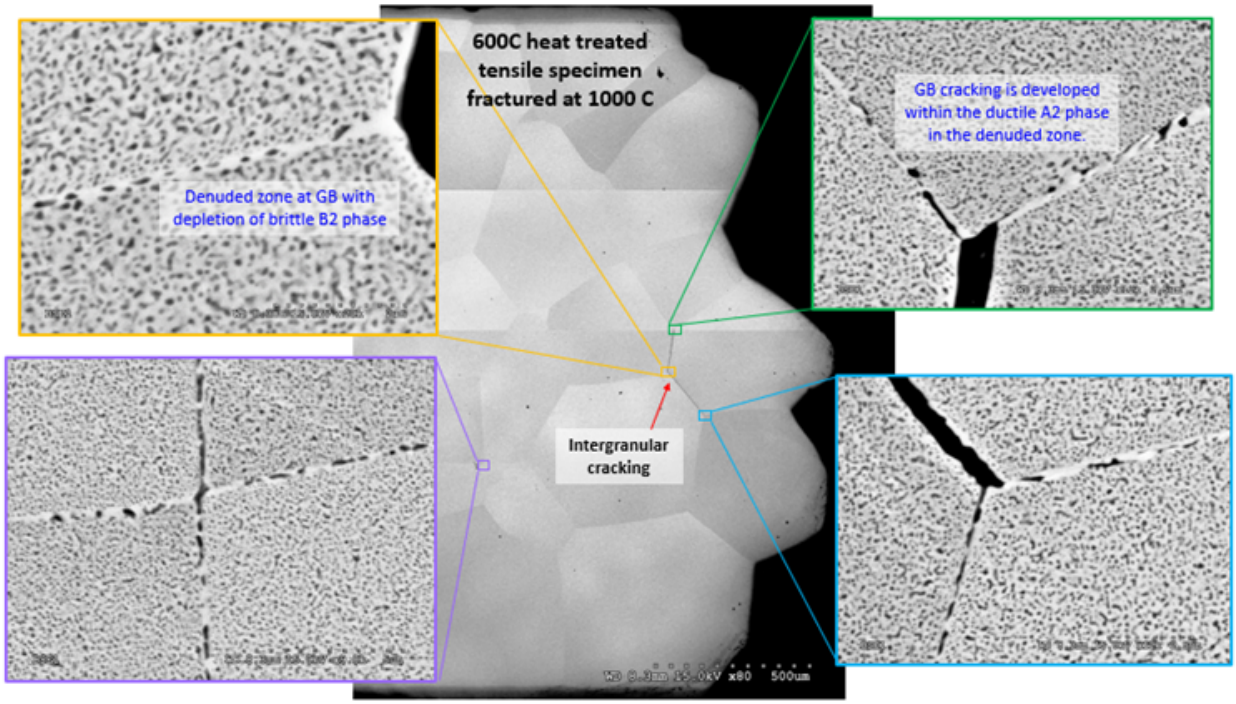

Figure 4.14: SEM BSE images of the fracture surface of the 600HT condition tensile specimen fractured at 1000 °C. At the grain boundaries, there is a brighter contrast area that represents a diluted zone.

The microstructure of grain interior in **Figure 4.14** is similar to the microstructure of the 800HT condition specimens. The basket-weave structure of the 600HT condition was transformed to microstructure with the B2 precipitates in A2 matrix during the high temperature tensile tests. This is not expected as it was shown that the temperature to transform into a single phase is above 1000 °C. The microstructural evolution was accelerated by the external tensile load as rafting occurred under the tensile load at high temperature. In order to check the effect of the external load, the compact tension samples were examined in a region that did not experience any tensile loading but experienced the same heating and cooling conditions as the tensile test, this microstructure is shown in **Figure 4.15**. The 600HT condition maintained the original basket-weave structure during a thermal cycle of high temperature tests, which means that external loads, whether in tension or compression, promote microstructural evolution at high temperature.

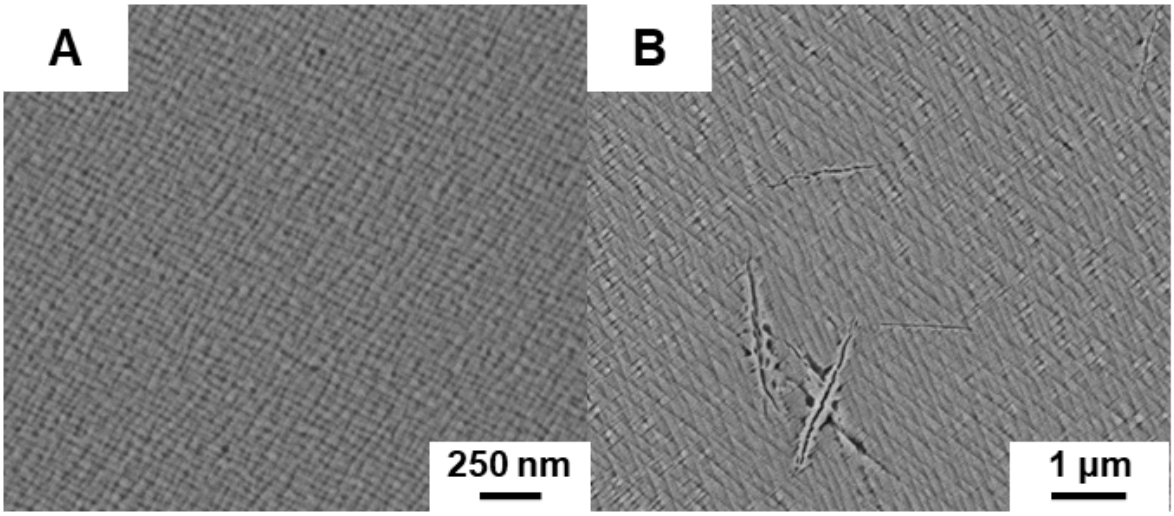

Figure 4.15: SEM back-scattered images of the undeformed region in the 600HT condition compact tension specimens tested at 800 °C (**A**) and 1000 °C (**B**).

Figure 4.16 displays the tensile specimen of the 800HT condition tested at 1000 °C. The 600HT condition and the 800HT condition were tested under the same conditions and both of them exhibited intergranular fracture, however, different phenomena were observed in **Figure 4.16**. In a grain at the fracture surface, cleavage-like intra-granular cracking was observed.` Voids were observed at some grain boundaries**,** which means inter-granular cracking is likely facilitated by cavitation nucleation at grain boundaries. This means that even though the 800HT condition showed an intergranular fracture mechanism the same as the 600HT condition, it fractured in a more ductile manner than the 600HT condition accounting for this slightly increased tensile strength and toughness seen in the the 800HT condition samples.

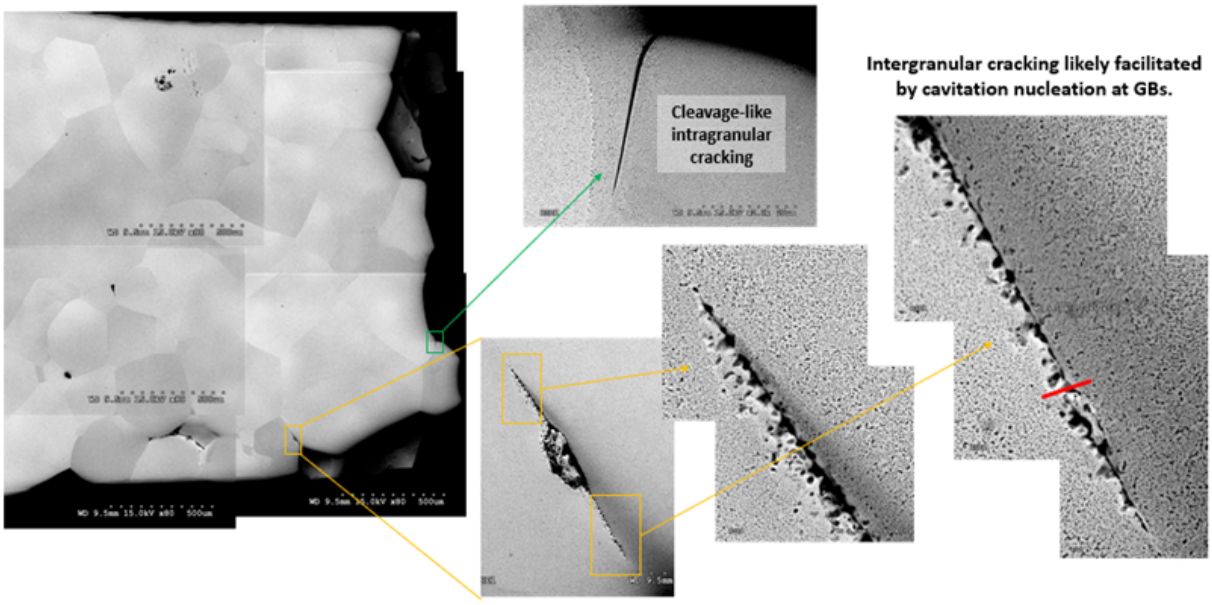

Figure 4.16: SEM BSE images of the fracture surface of the 800HT condition tensile specimen fractured at 1000 °C.

Since all tests under the tensile load exhibited brittle intergranular fracture, it is necessary to analyze the microstructure of the grain boundaries. **Figure 4.17** displays TEM images and EDS analysis of the two RHSAs before testing and after deformation at 1000 °C. In the TEM dark-field images, the zone axis were aligned so that only one grain was diffracted in order to determine the direction and location of the grain boundaries. Recent reports have shown that Ti, Zr, and Al segregate to the B2 phase, and Nb and Ta segregate to the A2 phase [99], [102], [111]. This is consistent with our EDS analysis results. It can be seen that Ti, Zr, and Al-rich B2 phase are segregated at grain boundaries in both of the RHSA aged conditions. This is because the alloy was homogenized as a single A2 phase and then annealed at 1400 °C which caused the B2 phase to precipitate from the A2 phase. This happened at the grain boundaries as well as the grain interiors. The difference between the two samples is that the Ti, Zr, and Al depleted zone by B2 precipitation in the grain boundary was clearly observed in the 600HT condition sample. This leaves the remaining A2 phase depleted of these elements, which weakens the grain boundaries. On the other hand, the 800HT condition sample also has segregated B2 in grain boundaries but does not have the Ti, Zr, and Al depleted zones. This allows the alloy to have a higher tensile strength than the 600HT condition at RT. At 1000 °C, the 600HT condition mostly shows B2 phase growth in the grain boundaries, while the 800HT condition contains both B2 and A2 phase in grain boundaries. For this reason, the the 800HT condition showed higher strength at all test temperatures than the 600HT condition.

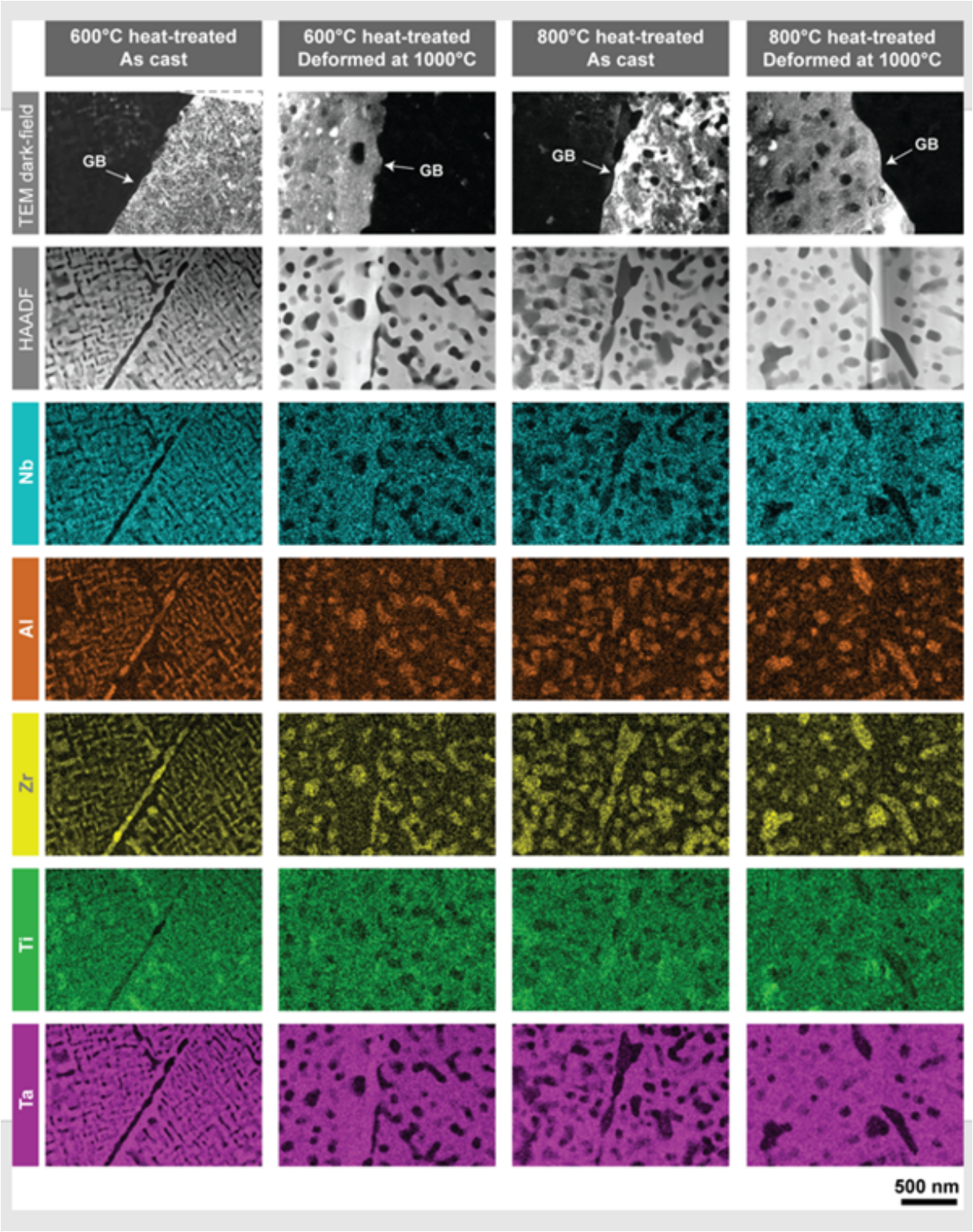

Figure 4.17: TEM images and EDS analysis of the two RHSAs before testing and after deformation at 1000 °C. In the TEM dark-field images, the zone axis were aligned so that only one grain was diffracted in order to determine the direction and location of the grain boundaries.

4.6 SUMMARY

In the present study, $Ti_{20}Zr_{20}Nb_{25}Ta_{25}Al_{10}$ RHSA with different microstructures was prepared and subjected to differing aging treatments. Aging at 600 ℃ for 24 h produced B2 matrix–A2 precipitates basket-weave microstructure and 800 ℃ for 12 h produced A2 matrix–B2 precipitates microstructure. The compression, tension, and fracture toughness properties were examined at RT, 800 ℃, 1000 ℃, and 1200 ℃. In compression, the 600HT condition showed strength as high as 1.7 GPa with low ductility, and the the 800HT condition showed a slightly lower strength of 1.2 GPa with higher fracture strain (~18 %) at RT. At elevated temperatures both RHSAs display considerable ductility exceeding 40%. During the high temperature compression test, both RHSA heat treatments showed a similar mechanical behavior. At 800 ℃ and 1000 ℃, where A2 + B2 phase is stable, grains were deformed relatively homogeneously, and the rafting phenomena was observed. Under tensile loading, the mechanical properties were poor, only deforming elastically, and with fracture toughness values not exceeding 5 MPa√m at all elevated temperatures. All tensile and fracture toughens specimens failed by brittle intergranular fracture. This intergranular fracture was likely due to the high amount of A2 phase at the grain boundaries and the diluted grain boundaries in the 600HT condition. The 800HT condition exhibited a higher tensile strength and fracture toughness because it did not experience the same grain boundary dilution that the 600HT condition did.

The vast majority of testing on RHEAs and RHSAs have been done in compression. These data are very misleading as one may misconstrue that if a material possesses compressive ductility that it should possess some tensile ductility, but it has been shown here that that is not the case, and should not be assumed. The 600HT condition and the 800HT condition showed over 40% ductility at high temperature in the compression, similarly to other RHEAs and RHSA's, but the $Ti_{20}Zr_{20}Nb_{25}Ta_{25}Al_{10}$ RHSA shows vanishingly small ductility in tension and a fracture toughness of ~5 MPa√m at high temperatures. Compression ductility cannot be used to make any inference on tensile properties of the material and tensile ductility is critical for real world applications. This material shows significant promise in compression, but its lack of tensile ductility and fracture toughness significantly limits its engineering application.

Chapter 5
Conclusions

Understanding a material's mechanical properties and failure mechanisms is incredibly important because it allows engineers to predict both how a material will behave under engineering applications and how it will fail under certain loading conditions. This is critical for the design of safe and reliable structural materials as well as the continued development of higher-performing materials. Here, I have described the mechanical properties and failure mechanisms of D&P steel, TRISO nuclear fuel particles, and RHSAs. D&P steel exhibits delamination and TRIP toughening that allows it to have an exceptionally high strength and toughness. Due to its highly tailored and layered microstructure, D&P steel bypasses the strength-toughness trade-off to achieve yield stresses close to 2 GPa, while maintaining a fracture toughness of 100 MPa√m and 75 MPa√m in the RD and TD, respectively. D&P steel's microstructure and mechanisms could be applied to other materials to increase their strength and toughness. In the future, other materials may have their microstructure tweaked to add in these toughening mechanisms to increase their mechanical properties. The next material type to be examined were TRISO nuclear particles using *in situ* tomography. Two types of TRISO particles, intended for use in nuclear reactors, were put into compression, and scanned during loading. The full 3D image at 1000 °C during loading showed that the SiC layer compromised the high temperature properties and illuminated the failure mechanisms with and without the SiC layer. The reduction of strength in the PyC-2 sample at high temperature is most likely due to the relaxation and redistribution of the residual stresses at elevated temperatures. Understanding this mechanism will lead to changes in these particles' design and processing that will allow them to be stronger at higher temperatures. With this knowledge it will be possible to improve the performance of these particles in the future. Finally, the high temperature compression, tensile strength, and fracture toughness of RHSAs was examined. The results show significant compressive ductility but lack tensile ductility, and exhibit brittle, intergranular fracture at all temperatures. This demonstrates that the compression data, commonly cited in literature, is misleading. To ensure that the mechanical properties of other HEAs and RHSAs are accurate, it is important that tensile data is recorded for these materials. Understanding the mechanisms of the poor tensile and fracture toughness properties can be used to improve the materials performance. The RHSA was brittle in tension due to low precipitation strengthening in the grain boundaries. Further development of this and similar alloys can focus on increasing grain boundary strength to increase tensile ductility and fracture toughness.

The forefront of research not only requires synthesizing materials that have complex microstructures that endow them with properties that allow them to endure extreme environments, but also requires a redesign of testing equipment in order to accurately reflect these extreme conditions that these materials are designed for. It is impossible to test a material that you want to operate at 1300℃ without a testing procedure and equipment that can achieve this environment. The final part of my work has been the design of a furnace that uses gold plated ellipsoidal halogen bulbs as a heating element. Inspired by a set-up used at the tomography beam line, where six 150 W bulbs can heat a sample over 1200 ℃, this new furnace design employs 16 of these bulbs. The simplicity of the design allows for reduced testing time and a simpler set-up procedure that is not limited to any particular load frame. Moreover, this

furnace can also be used in a vacuum or inert gas environment for oxidation prone materials. It will allow small scale samples to be heated to high temperatures in a way that makes testing much easier and significantly faster, thus creating the possibility to perform high throughput, high-temperature testing, a necessity for the HEA field that is confronted with the overwhelming amount of alloying combinations. With proper fixturing, small tensile samples can easily be tested to determine ductility more accurately than compression tests allow, and three-point and four-point bending specimens can be used to determine fracture toughness. Due to the high melting temperatures of many HEA constituents, large bulk samples are not possible to create, and therefore creating equipment to test small samples at high temperatures is a necessary adaptation for this field.

References

[1] R. Ritchie, “The Conflicts Between Strength and Toughness,” *Nat. Mater.*, vol. 10, pp. 817–22, Nov. 2011, doi: 10.1038/nmat3115.

[2] R. O. Ritchie, “Toughening materials: enhancing resistance to fracture,” *Philos. Trans. R. Soc. Math. Phys. Eng. Sci.*, vol. 379, no. 2203, p. 20200437, Aug. 2021, doi: 10.1098/rsta.2020.0437.

[3] J. H. Perepezko, “The Hotter the Engine, the Better,” *Science*, vol. 326, no. 5956, pp. 1068–1069, Nov. 2009, doi: 10.1126/science.1179327.

[4] L. Liu, Q. Yu, Z. Wang, J. Ell, M. X. Huang, and R. O. Ritchie, “Making ultrastrong steel tough by grain-boundary delamination.,” *Science*, vol. 368, no. 6497, pp. 1347–1352, Jun. 2020, doi: 10.1126/science.aba9413.

[5] D. Liu *et al.*, “X-ray tomography study on the crushing strength and irradiation behaviour of dedicated tristructural isotropic nuclear fuel particles at 1000 °C,” *Mater. Des.*, vol. 187, p. 108382, 2020, doi: https://doi.org/10.1016/j.matdes.2019.108382.

[6] B. B. He *et al.*, “High dislocation density–induced large ductility in deformed and partitioned steels,” *Science*, vol. 357, no. 6355, pp. 1029–1032, Sep. 2017, doi: 10.1126/science.aan0177.

[7] T. Taryo, I. Husnayani, R. M. Subekti, S. Sudadiyo, E. Saragi, and Rokhmadi, “The development of HTGR-TRISO coated fuels in the globe: challenging of Indonesia to be an HTGR fuel producer,” *J. Phys. Conf. Ser.*, vol. 1198, no. 2, p. 022062, Apr. 2019, doi: 10.1088/1742-6596/1198/2/022062.

[8] B. Liu, T. Liang, and C. Tang, “A review of TRISO-coated particle nuclear fuel performance models,” *Rare Met.*, vol. 25, no. 6, Supplement 1, pp. 337–342, Oct. 2006, doi: 10.1016/S1001-0521(07)60101-6.

[9] B. Cantor, I. T. H. Chang, P. Knight, and A. J. B. Vincent, “Microstructural development in equiatomic multicomponent alloys,” *Mater. Sci. Eng. A*, vol. 375–377, pp. 213–218, Jul. 2004, doi: 10.1016/j.msea.2003.10.257.

[10] J.-W. Yeh *et al.*, “Nanostructured High-Entropy Alloys with Multiple Principal Elements: Novel Alloy Design Concepts and Outcomes,” *Adv. Eng. Mater.*, vol. 6, no. 5, pp. 299–303, 2004, doi: 10.1002/adem.200300567.

[11] K. Lu, “The Future of Metals,” *Science*, vol. 328, no. 5976, pp. 319–320, Apr. 2010, doi: 10.1126/science.1185866.

[12] X. Li and K. Lu, “Playing with defects in metals,” *Nat. Mater.*, vol. 16, no. 7, Art. no. 7, Jul. 2017, doi: 10.1038/nmat4929.

[13] K. Lu, L. Lu, and S. Suresh, “Strengthening Materials by Engineering Coherent Internal Boundaries at the Nanoscale,” *Science*, vol. 324, no. 5925, pp. 349–352, Apr. 2009, doi: 10.1126/science.1159610.

[14] Jr. J.W. Morris, Z. Guo, C. R. Krenn, and Y.-H. Kim, “The Limits of Strength and Toughness in Steel,” *ISIJ Int.*, vol. 41, no. 6, pp. 599–611, 2001, doi: 10.2355/isijinternational.41.599.

[15] B. Gludovatz *et al.*, “Exceptional damage-tolerance of a medium-entropy alloy CrCoNi at cryogenic temperatures,” *Nat. Commun.*, vol. 7, no. 1, p. 10602, Feb. 2016, doi: 10.1038/ncomms10602.

[16] B. Gludovatz, A. Hohenwarter, D. Catoor, E. H. Chang, E. P. George, and R. O. Ritchie, “A

fracture-resistant high-entropy alloy for cryogenic applications," *Science*, vol. 345, no. 6201, pp. 1153–1158, Sep. 2014, doi: 10.1126/science.1254581.
[17] S. Floreen, "The physical metallurgy of maraging steels," *Metall. Rev.*, vol. 13, no. 1, pp. 115–128, Jan. 1968, doi: 10.1179/mtlr.1968.13.1.115.
[18] X. Li and K. Lu, "Improving sustainability with simpler alloys," *Science*, vol. 364, no. 6442, pp. 733–734, May 2019, doi: 10.1126/science.aaw9905.
[19] R. Cao *et al.*, "On the exceptional damage-tolerance of gradient metallic materials," *Mater. Today*, vol. 32, pp. 94–107, Jan. 2020, doi: 10.1016/j.mattod.2019.09.023.
[20] R. Cao, Q. Yu, Y. Li, and R. O. Ritchie, "Dual-gradient structure leads to optimized combination of high fracture resistance and strength-ductility synergy with minimized final catastrophic failure," *J. Mater. Res. Technol.*, vol. 15, pp. 901–910, Nov. 2021, doi: 10.1016/j.jmrt.2021.08.102.
[21] S. Zhao, R. Zhang, Q. Yu, J. Ell, R. O. Ritchie, and A. M. Minor, "Cryoforged nanotwinned titanium with ultrahigh strength and ductility," *Science*, vol. 373, no. 6561, pp. 1363–1368, 2021, doi: 10.1126/science.abe7252.
[22] Y. Lin, Q. Yu, J. Pan, F. Duan, R. O. Ritchie, and Y. Li, "On the impact toughness of gradient-structured metals," *Acta Mater.*, vol. 193, pp. 125–137, Jul. 2020, doi: 10.1016/j.actamat.2020.04.027.
[23] K. Lu, "Making strong nanomaterials ductile with gradients," *Science*, vol. 345, no. 6203, pp. 1455–1456, Sep. 2014, doi: 10.1126/science.1255940.
[24] Y. Wang, M. Chen, F. Zhou, and E. Ma, "High tensile ductility in a nanostructured metal," *Nature*, vol. 419, no. 6910, Art. no. 6910, Oct. 2002, doi: 10.1038/nature01133.
[25] C. C. Koch, D. G. Morris, K. Lu, and A. Inoue, "Ductility of Nanostructured Materials," *MRS Bull.*, vol. 24, no. 2, pp. 54–58, Feb. 1999, doi: 10.1557/S0883769400051551.
[26] K. T. Venkateswara Rao, W. Yu, and R. O. Ritchie, "Cryogenic toughness of commercial aluminum-lithium alloys: Role of delamination toughening," *Metall. Trans. A*, vol. 20, no. 3, pp. 485–497, Mar. 1989, doi: 10.1007/BF02653929.
[27] K. S. Chan, "Evidence of a thin sheet toughening mechanism in Al−Fe−X alloys," *Metall. Trans. A*, vol. 20, no. 1, pp. 155–164, Jan. 1989, doi: 10.1007/BF02647502.
[28] L. Liu, B. He, and M. X. Huang, "Processing-Microstructure Relation of Deformed and Partitioned (D&P) Steels," *Met. - Open Access Metall. J.*, vol. 9, Jun. 2019, doi: 10.3390/met9060695.
[29] J. Speer, D. K. Matlock, B. C. De Cooman, and J. G. Schroth, "Carbon partitioning into austenite after martensite transformation," *Acta Mater.*, vol. 51, no. 9, pp. 2611–2622, May 2003, doi: 10.1016/S1359-6454(03)00059-4.
[30] S. Chatterjee, H.-S. Wang, J. R. Yang, and H. K. D. H. Bhadeshia, "Mechanical stabilisation of austenite," *Mater. Sci. Technol.*, vol. 22, no. 6, pp. 641–644, Jun. 2006, doi: 10.1179/174328406X86128.
[31] M. Wang, C. Tasan, D. Ponge, A.-C. Dippel, and D. Raabe, "Nanolaminate transformation-induced plasticity - twinning-induced plasticity steel with dynamic strain partitioning and enhanced damage resistance," *Acta Mater.*, vol. 85, pp. 216–228, Feb. 2015, doi: 10.1016/j.actamat.2014.11.010.
[32] "Standard Test Method for Measurement of Fracture Toughness." https://www.astm.org/e1820-17.html (accessed Nov. 30, 2021).
[33] C. S. Carter, "Stress corrosion crack branching in high-strength steels," *Eng. Fract. Mech.*, vol. 3, no. 1, pp. 1–13, Jul. 1971, doi: 10.1016/0013-7944(71)90047-6.

[34] Y. He, K. Yang, W. Qu, F. Kong, and G. Su, “Strengthening and toughening of a 2800-MPa grade maraging steel,” *Mater. Lett.*, vol. 56, no. 5, pp. 763–769, Nov. 2002, doi: 10.1016/S0167-577X(02)00610-9.
[35] R. O. Ritchie, “Influence of microstructure on near-threshold fatigue-crack propagation in ultra-high strength steel,” *Met. Sci.*, vol. 11, no. 8–9, pp. 368–381, Aug. 1977, doi: 10.1179/msc.1977.11.8-9.368.
[36] R. O. Ritchie, B. Francis, and W. L. Server, “Evaluation of toughness in AISI 4340 alloy steel austenitized at low and high temperatures,” *Metall. Trans. A*, vol. 7, no. 6, pp. 831–838, Jun. 1976, doi: 10.1007/BF02644080.
[37] N. H. Heo, J. W. Nam, Y.-U. Heo, and S.-J. Kim, “Grain boundary embrittlement by Mn and eutectoid reaction in binary Fe–12Mn steel,” *Acta Mater.*, vol. 61, no. 11, pp. 4022–4034, Jun. 2013, doi: 10.1016/j.actamat.2013.03.016.
[38] M. Kuzmina, D. Ponge, and D. Raabe, “Grain boundary segregation engineering and austenite reversion turn embrittlement into toughness: Example of a 9wt.% medium Mn steel,” *Acta Mater.*, vol. 86, pp. 182–192, Mar. 2015, doi: 10.1016/j.actamat.2014.12.021.
[39] Y. Kimura, T. Inoue, F. Yin, and K. Tsuzaki, “Inverse Temperature Dependence of Toughness in an Ultrafine Grain-Structure Steel,” *Science*, vol. 320, no. 5879, pp. 1057–1060, May 2008, doi: 10.1126/science.1156084.
[40] J. W. Morris, “Stronger, Tougher Steels,” *Science*, vol. 320, no. 5879, pp. 1022–1023, May 2008, doi: 10.1126/science.1158994.
[41] W. Bleck, X. Guo, and Y. Ma, “The TRIP Effect and Its Application in Cold Formable Sheet Steels,” *Steel Res. Int.*, vol. 88, no. 10, p. 1700218, 2017, doi: 10.1002/srin.201700218.
[42] R. H. Leal, “Transformation toughening of metastable austenitic steels,” Thesis, Massachusetts Institute of Technology, 1984. Accessed: Feb. 21, 2022. [Online]. Available: https://dspace.mit.edu/handle/1721.1/15349
[43] M. A. Linaza, J. L. Romero, J. M. Rodríguez-Ibabe, and J. J. Urcola, “Improvement of fracture toughness of forging steels microalloyed with titanium by accelerated cooling after hot working,” *Scr. Metall. Mater.*, vol. 29, no. 9, pp. 1217–1222, Nov. 1993, doi: 10.1016/0956-716X(93)90112-6.
[44] M. E. Haque and K. V. Sudhakar, “ANN back-propagation prediction model for fracture toughness in microalloy steel,” *Int. J. Fatigue*, vol. 24, no. 9, pp. 1003–1010, Sep. 2002, doi: 10.1016/S0142-1123(01)00207-9.
[45] S. K. Putatunda, “Fracture toughness of a high carbon and high silicon steel,” *Mater. Sci. Eng. A*, vol. 297, no. 1, pp. 31–43, Jan. 2001, doi: 10.1016/S0921-5093(00)01272-7.
[46] “Fracture Toughness of an Advanced Ultrahigh-strength TRIP-aided Steel.” https://www.jstage.jst.go.jp/article/isijinternational/54/4/54_955/_article (accessed Feb. 21, 2022).
[47] A. Bayram, A. Uğuz, and M. Ula, “Effects of Microstructure and Notches on the Mechanical Properties of Dual-Phase Steels,” *Mater. Charact.*, vol. 43, no. 4, pp. 259–269, Oct. 1999, doi: 10.1016/S1044-5803(99)00044-3.
[48] L. Xiong, Z. S. You, S. D. Qu, and L. Lu, “Fracture behavior of heterogeneous nanostructured 316L austenitic stainless steel with nanotwin bundles,” *Acta Mater.*, vol. 150, pp. 130–138, May 2018, doi: 10.1016/j.actamat.2018.02.065.
[49] J. E. Pawel *et al.*, “Fracture toughness of candidate materials for ITER first wall, blanket, and shield structures,” *J. Nucl. Mater.*, vol. 212–215, pp. 442–447, Sep. 1994, doi:

10.1016/0022-3115(94)90101-5.
[50] L. F. Van Swam, R. M. Pelloux, and N. J. Grant, “Properties of Maraging Steel 300 Produced by Powder Metallurgy,” *Powder Metall.*, vol. 17, no. 33, pp. 33–45, Mar. 1974, doi: 10.1179/pom.1974.17.33.004.
[51] R. O. Ritchie, “Near-Threshold Fatigue Crack Propagation in Ultra-High Strength Steel: Influence of Load Ratio and Cyclic Strength,” *J. Eng. Mater. Technol.*, vol. 99, no. 3, pp. 195–204, Jul. 1977, doi: 10.1115/1.3443519.
[52] G. Y. Lai, W. E. Wood, R. A. Clark, V. F. Zackay, and E. R. Parker, “The effect of austenitizing temperature on the microstructure and mechanical properties of as-quenched 4340 steel,” *Metall. Mater. Trans. B*, vol. 5, no. 7, pp. 1663–1670, Jul. 1974, doi: 10.1007/BF02646340.
[53] H. A. Aglan, Z. Y. Liu, M. F. Hassan, and M. Fateh, “Mechanical and fracture behavior of bainitic rail steel,” *J. Mater. Process. Technol.*, vol. 151, no. 1, pp. 268–274, Sep. 2004, doi: 10.1016/j.jmatprotec.2004.04.073.
[54] C. Garcia-Mateo and F. G. Caballero, “Ultra-high-strength Bainitic Steels,” *ISIJ Int.*, vol. 45, no. 11, pp. 1736–1740, 2005, doi: 10.2355/isijinternational.45.1736.
[55] M. D. Demetriou *et al.*, “A damage-tolerant glass,” *Nat. Mater.*, vol. 10, no. 2, Art. no. 2, Feb. 2011, doi: 10.1038/nmat2930.
[56] N. Kamp, I. Sinclair, and M. J. Starink, “Toughness-strength relations in the overaged 7449 al-based alloy,” *Metall. Mater. Trans. A*, vol. 33, no. 4, pp. 1125–1136, Apr. 2002, doi: 10.1007/s11661-002-0214-2.
[57] M. Niinomi, “Mechanical properties of biomedical titanium alloys,” *Mater. Sci. Eng. A*, vol. 243, no. 1, pp. 231–236, Mar. 1998, doi: 10.1016/S0921-5093(97)00806-X.
[58] R. A. Mirshams, C. H. Xiao, S. H. Whang, and W. M. Yin, “R-Curve characterization of the fracture toughness of nanocrystalline nickel thin sheets,” *Mater. Sci. Eng. A*, vol. 315, no. 1, pp. 21–27, Sep. 2001, doi: 10.1016/S0921-5093(01)01213-8.
[59] A. Singh, L. Tang, M. Dao, L. Lu, and S. Suresh, “Fracture toughness and fatigue crack growth characteristics of nanotwinned copper,” *Acta Mater.*, vol. 59, no. 6, pp. 2437–2446, Apr. 2011, doi: 10.1016/j.actamat.2010.12.043.
[60] Y. Brits, F. Botha, H. van Antwerpen, and H.-W. Chi, “A control approach investigation of the Xe-100 plant to perform load following within the operational range of 100 – 25 – 100%,” *Nucl. Eng. Des.*, vol. 329, pp. 12–19, Apr. 2018, doi: 10.1016/j.nucengdes.2017.11.041.
[61] J. M. Beck and L. F. Pincock, “High Temperature Gas-Cooled Reactors Lessons Learned Applicable to the Next Generation Nuclear Plant,” Idaho National Lab. (INL), Idaho Falls, ID (United States), INL/EXT-10-19329, Apr. 2011. doi: 10.2172/1023461.
[62] H. Nickel, H. Nabielek, G. Pott, and A. W. Mehner, “Long time experience with the development of HTR fuel elements in Germany,” *Nucl. Eng. Des.*, vol. 217, no. 1, pp. 141–151, Aug. 2002, doi: 10.1016/S0029-5493(02)00128-0.
[63] K. Roellig and W. Theymann, “Operational requirements of spherical HTR fuel elements and their performance,” International Atomic Energy Agency (IAEA), 1985.
[64] M. Lang, H. Xie, and Y. Dong, “Three Design Basis Accidents’ Analysis on the HTR-10GT,” *Sci. Technol. Nucl. Install.*, vol. 2017, p. e1686291, Jun. 2017, doi: 10.1155/2017/1686291.
[65] K. FUKUDA *et al.*, “Research and Development of HTTR Coated Particle Fuel,” *J. Nucl. Sci. Technol.*, vol. 28, no. 6, pp. 570–581, Jun. 1991, doi: 10.1080/18811248.1991.9731396.

[66] S. Saito, T. Tanaka, and Y. Sudo, “Design of high temperature Engineering Test Reactor (HTTR),” Japan, 1994.
[67] K. A. Terrani, L. L. Snead, and J. C. Gehin, “Microencapsulated fuel technology for commercial light water and advanced reactor application,” *J. Nucl. Mater.*, vol. 427, no. 1, pp. 209–224, Aug. 2012, doi: 10.1016/j.jnucmat.2012.05.021.
[68] J. Porta *et al.*, “Coated particle fuel to improve safety, design, economics in water-cooled and gas-cooled reactors,” *Prog. Nucl. Energy*, vol. 38, no. 3, pp. 407–410, Jan. 2001, doi: 10.1016/S0149-1970(00)00146-3.
[69] K. A. Terrani *et al.*, “Fabrication and characterization of fully ceramic microencapsulated fuels,” *J. Nucl. Mater.*, vol. 426, no. 1, pp. 268–276, Jul. 2012, doi: 10.1016/j.jnucmat.2012.03.049.
[70] K. A. Terrani, L. L. Snead, and J. C. Gehin, “FCM Fuel Development for SMR Applications,” Feb. 2012, pp. 207–209. doi: 10.1115/SMR2011-6608.
[71] J. J. Powers *et al.*, “Fully Ceramic Microencapsulated (FCM) Replacement Fuel for LWRs,” Oak Ridge National Lab. (ORNL), Oak Ridge, TN (United States), ORNL/TM-2013/173, Jul. 2013. doi: 10.2172/1087039.
[72] L. L. Snead, T. Nozawa, Y. Katoh, T.-S. Byun, S. Kondo, and D. A. Petti, “Handbook of SiC properties for fuel performance modeling,” *J. Nucl. Mater.*, vol. 371, no. 1, pp. 329–377, Sep. 2007, doi: 10.1016/j.jnucmat.2007.05.016.
[73] J. D. Hunn *et al.*, “Detection and analysis of particles with failed SiC in AGR-1 fuel compacts,” *Nucl. Eng. Des.*, vol. 306, pp. 36–46, Sep. 2016, doi: 10.1016/j.nucengdes.2015.12.011.
[74] D. A. Petti, J. Buongiorno, J. T. Maki, R. R. Hobbins, and G. K. Miller, “Key differences in the fabrication, irradiation and high temperature accident testing of US and German TRISO-coated particle fuel, and their implications on fuel performance,” *Nucl. Eng. Des.*, vol. 222, no. 2, pp. 281–297, Jun. 2003, doi: 10.1016/S0029-5493(03)00033-5.
[75] D. Liu, B. Gludovatz, H. S. Barnard, M. Kuball, and R. O. Ritchie, “Damage tolerance of nuclear graphite at elevated temperatures,” *Nat. Commun.*, vol. 8, no. 1, Art. no. 1, Jun. 2017, doi: 10.1038/ncomms15942.
[76] H. A. Bale *et al.*, “Real-time quantitative imaging of failure events in materials under load at temperatures above 1,600 °C,” *Nat. Mater.*, vol. 12, no. 1, pp. 40–46, Jan. 2013, doi: 10.1038/nmat3497.
[77] S. Knol, S. de Groot, P. R. Hania, and M. H. C. Hannink, “PYCASSO: Irradiation of HTR coated particles at high temperatures,” *Nucl. Eng. Des.*, vol. 251, pp. 150–156, Oct. 2012, doi: 10.1016/j.nucengdes.2011.10.050.
[78] S.-G. Hong, T.-S. Byun, R. A. Lowden, L. L. Snead, and Y. Katoh, “Evaluation of the Fracture Strength for Silicon Carbide Layers in the Tri-Isotropic-Coated Fuel Particle,” *J. Am. Ceram. Soc.*, vol. 90, no. 1, pp. 184–191, 2007, doi: 10.1111/j.1551-2916.2005.01367.x.
[79] N. Rohbeck and P. Xiao, “Evaluation of the mechanical performance of silicon carbide in TRISO fuel at high temperatures,” *Nucl. Eng. Des.*, vol. 306, pp. 52–58, Sep. 2016, doi: 10.1016/j.nucengdes.2016.05.040.
[80] P. Hosemann *et al.*, “Mechanical characteristics of SiC coating layer in TRISO fuel particles,” *J. Nucl. Mater.*, vol. 442, no. 1, pp. 133–142, Nov. 2013, doi: 10.1016/j.jnucmat.2013.08.041.
[81] “Evaluation of Fracture Stress for the SiC Layer of TRISO‐Coated Fuel Particles Using a

Modified Crush Test Method - Byun - 2010 - International Journal of Applied Ceramic Technology - Wiley Online Library." https://ceramics.onlinelibrary.wiley.com/doi/10.1111/j.1744-7402.2009.02462.x (accessed Nov. 30, 2021).

[82] G. T. van Rooyen, R. du Preez, J. de Villiers, and R. Cromarty, "The fracture strength of TRISO-coated particles determined by compression testing between soft aluminium anvils," *J. Nucl. Mater.*, vol. 403, no. 1, pp. 126–134, Aug. 2010, doi: 10.1016/j.jnucmat.2010.06.011.

[83] R. D. Cromarty, G. T. van Rooyen, and J. P. R. de Villiers, "Crush strength of silicon carbide coated TRISO particles: Influence of test method and process variables," *J. Nucl. Mater.*, vol. 445, no. 1, pp. 30–36, Feb. 2014, doi: 10.1016/j.jnucmat.2013.10.041.

[84] A. Briggs, R. W. Davidge, C. Padgett, and S. Quickenden, "Crushing behaviour of high temperature reactor coated fuel particles," *J. Nucl. Mater.*, vol. 61, no. 3, pp. 233–242, Sep. 1976, doi: 10.1016/0022-3115(76)90262-2.

[85] T. Ogawa and K. Ikawa, "Crushing strengths of SiC-Triso and ZrC-Triso coated fuel particles," *J. Nucl. Mater.*, vol. 98, no. 1, pp. 18–26, May 1981, doi: 10.1016/0022-3115(81)90383-4.

[86] K. Minato, K. Fukuda, K. Ikawa, H. Matsushima, and S. Kurobane, "Crushing strength of irradiated Triso coated fuel particles," *J. Nucl. Mater.*, vol. 119, no. 2, pp. 326–332, Dec. 1983, doi: 10.1016/0022-3115(83)90211-8.

[87] I. J. Van Rooyen, J. H. Neethling, and P. M. Van Rooyen, "The influence of annealing temperature on the strength of TRISO coated particles," *J. Nucl. Mater.*, vol. 402, no. 2–3, pp. 136–146, 2010, doi: 10.1016/j.jnucmat.2010.05.009.

[88] W. J. Lackey, D. P. Stinton, L. E. Davis, and R. L. Beatty, "Crushing strength of high temperature gas cooled reactor fuel particles," *Nucl. Technol.*, vol. 31, no. 2, pp. 191–201, 1976, doi: 10.13182/NT76-A31682.

[89] N. Rohbeck *et al.*, "In-situ nanoindentation of irradiated silicon carbide in TRISO particle fuel up to 500 °C," *J. Nucl. Mater.*, vol. 465, pp. 692–694, Oct. 2015, doi: 10.1016/j.jnucmat.2015.06.035.

[90] A. Haboub *et al.*, "Tensile testing of materials at high temperatures above 1700 °C with in situ synchrotron X-ray micro-tomography," *Rev. Sci. Instrum.*, vol. 85, no. 8, p. 083702, Aug. 2014, doi: 10.1063/1.4892437.

[91] "Hertz: On the Contact of Rigid Elastic Solids and Hardness - Google Scholar." https://scholar.google.com/scholar_lookup?title=On%20the%20Contact%20of%20Rigid%20Elastic%20Solids%20and%20Hardness&author=H.%20Hertz&publication_year=1882 (accessed Mar. 15, 2022).

[92] K. E. Gilchrist and J. E. Brocklehurst, "A technique for measuring the strength of high temperature reactor fuel particle coatings," *J. Nucl. Mater.*, vol. 43, no. 3, pp. 347–350, Jun. 1972, doi: 10.1016/0022-3115(72)90069-4.

[93] W. Delle, K. Drittler, G. Haag, and H. Schiffeis, *JUL-569-RW*, vol. ORNL-tr-2128, 1969.

[94] K. V. S. Thurston, B. Gludovatz, A. Hohenwarter, G. Laplanche, E. P. George, and R. O. Ritchie, "Effect of temperature on the fatigue-crack growth behavior of the high-entropy alloy CrMnFeCoNi," *Intermetallics*, vol. 88, pp. 65–72, Sep. 2017, doi: 10.1016/j.intermet.2017.05.009.

[95] D. B. Miracle and O. N. Senkov, "A critical review of high entropy alloys and related concepts," *Acta Mater.*, vol. 122, pp. 448–511, Jan. 2017, doi:

10.1016/j.actamat.2016.08.081.
[96] O. N. Senkov, D. B. Miracle, K. J. Chaput, and J.-P. Couzinie, “Development and exploration of refractory high entropy alloys—A review,” *J. Mater. Res.*, vol. 33, no. 19, pp. 3092–3128, Oct. 2018, doi: 10.1557/jmr.2018.153.
[97] W. Knabl, G. Leichtfried, and R. Stickler, “Refractory Metals and Refractory Metal Alloys,” in *Springer Handbook of Materials Data*, H. Warlimont and W. Martienssen, Eds. Cham: Springer International Publishing, 2018, pp. 307–337. doi: 10.1007/978-3-319-69743-7_13.
[98] O. N. Senkov, G. B. Wilks, J. M. Scott, and D. B. Miracle, “Mechanical properties of Nb25Mo25Ta25W25 and V20Nb20Mo20Ta20W20 refractory high entropy alloys,” *Intermetallics*, vol. 19, no. 5, pp. 698–706, May 2011, doi: 10.1016/j.intermet.2011.01.004.
[99] O. N. Senkov, J. M. Scott, S. V. Senkova, D. B. Miracle, and C. F. Woodward, “Microstructure and room temperature properties of a high-entropy TaNbHfZrTi alloy,” *J. Alloys Compd.*, vol. 509, no. 20, pp. 6043–6048, May 2011, doi: 10.1016/j.jallcom.2011.02.171.
[100] O. N. Senkov, J. M. Scott, S. V. Senkova, F. Meisenkothen, D. B. Miracle, and C. F. Woodward, “Microstructure and elevated temperature properties of a refractory TaNbHfZrTi alloy,” *J. Mater. Sci.*, vol. 47, no. 9, pp. 4062–4074, May 2012, doi: 10.1007/s10853-012-6260-2.
[101] O. N. Senkov, D. Isheim, D. N. Seidman, and A. L. Pilchak, “Development of a Refractory High Entropy Superalloy,” *Entropy*, vol. 18, no. 3, Art. no. 3, Mar. 2016, doi: 10.3390/e18030102.
[102] V. Soni, O. N. Senkov, B. Gwalani, D. B. Miracle, and R. Banerjee, “Microstructural Design for Improving Ductility of An Initially Brittle Refractory High Entropy Alloy,” *Sci. Rep.*, vol. 8, no. 1, p. 8816, Jun. 2018, doi: 10.1038/s41598-018-27144-3.
[103] B. P. Bewlay, M. R. Jackson, J. C. Zhao, P. R. Subramanian, M. G. Mendiratta, and J. J. Lewandowski, “Ultrahigh-Temperature Nb-Silicide-Based Composites,” *MRS Bull.*, vol. 28, no. 9, pp. 646–653, Sep. 2003, doi: 10.1557/mrs2003.192.
[104] B. P. Bewlay, M. R. Jackson, and H. A. Lipsitt, “The balance of mechanical and environmental properties of a multielement niobium-niobium silicide-basedIn Situ composite,” *Metall. Mater. Trans. A*, vol. 27, no. 12, pp. 3801–3808, Dec. 1996, doi: 10.1007/BF02595629.
[105] J. A. Lemberg and R. O. Ritchie, “Mo-Si-B Alloys for Ultrahigh-Temperature Structural Applications,” *Adv. Mater.*, vol. 24, no. 26, pp. 3445–3480, 2012, doi: 10.1002/adma.201200764.
[106] J. H. Schneibel, P. F. Tortorelli, R. O. Ritchie, and J. J. Kruzic, “Optimization of Mo-Si-B intermetallic alloys,” *Metall. Mater. Trans. A*, vol. 36, no. 3, pp. 525–531, Mar. 2005, doi: 10.1007/s11661-005-0166-4.
[107] K. Ito, M. Kumagai, T. Hayashi, and M. Yamaguchi, “Room temperature fracture toughness and high temperature strength of T2/Moss and (Mo,Nb)ss/T1/T2 eutectic alloys in the Mo–Si–B system,” *Scr. Mater.*, vol. 49, no. 4, pp. 285–290, Aug. 2003, doi: 10.1016/S1359-6462(03)00289-6.
[108] J. J. Brennan and K. M. Prewo, “Silicon carbide fibre reinforced glass-ceramic matrix composites exhibiting high strength and toughness,” *J. Mater. Sci.*, vol. 17, no. 8, pp. 2371–2383, Aug. 1982, doi: 10.1007/BF00543747.
[109] H. Porwal, S. Grasso, and M. J. Reece, “Review of graphene–ceramic matrix

composites," *Adv. Appl. Ceram.*, vol. 112, no. 8, pp. 443–454, Nov. 2013, doi: 10.1179/174367613X13764308970581.
[110] T. E. Whitfield, E. J. Pickering, K. A. Christofidou, C. N. Jones, H. J. Stone, and N. G. Jones, "Elucidating the microstructural development of refractory metal high entropy superalloys via the Ti–Ta–Zr constituent system," *J. Alloys Compd.*, vol. 818, p. 152935, Mar. 2020, doi: 10.1016/j.jallcom.2019.152935.
[111] P. Wanjara, M. Jahazi, H. Monajati, S. Yue, and J.-P. Immarigeon, "Hot working behavior of near-α alloy IMI834," *Mater. Sci. Eng. A*, vol. 1–2, no. 396, pp. 50–60, 2005, doi: 10.1016/j.msea.2004.12.005.
[112] X. Wu, "Review of alloy and process development of TiAl alloys," *Intermetallics*, vol. 14, no. 10, pp. 1114–1122, Oct. 2006, doi: 10.1016/j.intermet.2005.10.019.
[113] F. Liu, J. Chen, J. Dong, M. Zhang, and Z. Yao, "The hot deformation behaviors of coarse, fine and mixed grain for Udimet 720Li superalloy," *Mater. Sci. Eng. A*, vol. 651, pp. 102–115, Jan. 2016, doi: 10.1016/j.msea.2015.10.099.
[114] R. R. Eleti, T. Bhattacharjee, A. Shibata, and N. Tsuji, "Unique deformation behavior and microstructure evolution in high temperature processing of HfNbTaTiZr refractory high entropy alloy," *Acta Mater.*, vol. 171, pp. 132–145, Jun. 2019, doi: 10.1016/j.actamat.2019.04.018.
[115] N. N. Guo *et al.*, "Hot deformation characteristics and dynamic recrystallization of the MoNbHfZrTi refractory high-entropy alloy," *Mater. Sci. Eng. A*, vol. 651, pp. 698–707, Jan. 2016, doi: 10.1016/j.msea.2015.10.113.
[116] M. Kamaraj, "Rafting in single crystal nickel-base superalloys — An overview," *Sadhana*, vol. 28, no. 1, pp. 115–128, Feb. 2003, doi: 10.1007/BF02717129.
[117] H. Long *et al.*, "A comparative study of rafting mechanisms of Ni-based single crystal superalloys," *Mater. Des.*, vol. 196, p. 109097, Nov. 2020, doi: 10.1016/j.matdes.2020.109097.
[118] J. Coakley *et al.*, "Rafting and elastoplastic deformation of superalloys studied by neutron diffraction," *Scr. Mater.*, vol. 134, pp. 110–114, Jun. 2017, doi: 10.1016/j.scriptamat.2017.03.007.
[119] Y. Li *et al.*, "Rafting of γ′ precipitates in a Co-9Al-9W superalloy during compressive creep," *Mater. Sci. Eng. A*, vol. 719, Feb. 2018, doi: 10.1016/j.msea.2018.02.017.
[120] O. N. Senkov, S. V. Senkova, and C. Woodward, "Effect of aluminum on the microstructure and properties of two refractory high-entropy alloys," *Acta Mater.*, vol. 68, pp. 214–228, Apr. 2014, doi: 10.1016/j.actamat.2014.01.029.
[121] O. N. Senkov, J. K. Jensen, A. L. Pilchak, D. B. Miracle, and H. L. Fraser, "Compositional variation effects on the microstructure and properties of a refractory high-entropy superalloy AlMo0.5NbTa0.5TiZr," *Mater. Des.*, vol. 139, pp. 498–511, Feb. 2018, doi: 10.1016/j.matdes.2017.11.033.